

WIND TURBINE BLADE BEARING FAULT DETECTION AND DIAGNOSIS USING VIBRATION AND ACOUSTIC EMISSION SIGNAL ANALYSIS

A THESIS SUBMITTED TO THE UNIVERSITY OF MANCHESTER
FOR THE DEGREE OF DOCTOR OF PHILOSOPHY
IN THE FACULTY OF SCIENCE AND ENGINEERING

2021

Zepeng Liu

School of Engineering

Department of Electrical and Electronic Engineering

Contents

List of Figures	9
Symbols	14
Abbreviations	14
Abstract	15
Declaration	17
Copyright Statement	18
Publications	19
Acknowledgements	20
1 Introduction to Blade Bearing Fault Detections	21
1.1 Introduction	21
1.2 Challenges and Objectives	23
1.3 Contributions of the thesis	24

1.4	Thesis Organization	25
2	Review of Failure Modes for Large-scale Wind Turbine Bearings	27
2.1	Introduction	27
2.2	Types of large-scale wind turbine bearings	29
2.3	Failure modes of large-scale wind turbine bearings	31
2.3.1	Plastic deformation	31
2.3.2	Lubricant	32
2.3.3	Electrical arc erosion	34
2.3.4	Cracks and fractures	35
2.3.5	Wear	36
2.3.6	Mounting failure/improper mounting	37
2.3.7	Failure mode classification	40
2.4	The failure mode of blade bearings	41
2.5	Conclusion	44
3	Review of Condition Monitoring and Fault Diagnosis for Large-scale Wind Turbine Bearings	45
3.1	Introduction	45
3.2	Data acquisition techniques	45
3.2.1	Vibration	46
3.2.2	Acoustic emission	46
3.2.3	Lubricant/debris	47

3.2.4	Power quality	47
3.2.5	Borescope inspection	47
3.2.6	Temperature Monitoring	48
3.2.7	Other techniques	48
3.3	CMFD for main bearings	48
3.3.1	Vibration signal Analysis	48
3.3.2	Stator current analysis	50
3.3.3	Summary of the review for main bearings CMFD	51
3.4	CMFD for gearbox bearings	51
3.4.1	Vibration signal analysis	51
3.4.2	Electrical signal analysis	54
3.4.3	Microscope analysis	55
3.4.4	Lubricant/debris analysis	56
3.4.5	Summary of the review for gearbox bearings CMFD	56
3.5	CMFD for generator bearings	57
3.5.1	Vibration signal analysis	57
3.5.2	Electrical signal analysis	61
3.5.3	Supervisory control and data acquisition (SCADA) analysis	62
3.5.4	Summary of the review for generator bearings CMFD	62
3.6	CMFD for blade bearings and yaw bearings	63
3.7	Potential CMFD methods for large-scale wind turbine bearings	63

3.7.1	Slow-speed sensing	64
3.7.2	Non-stationary methods	65
3.8	Summary	68
4	Detection Principle and Test-rig Facility	69
4.1	Introduction	69
4.2	Bearing defect frequencies	69
4.3	Test-rig Construction and Components	70
4.4	Conclusion	73
5	Vibration Fault Diagnosis Using Wavelet Filtering	75
5.1	Introduction	75
5.2	Theoretical background	77
5.2.1	Empirical wavelet thresholding	77
5.2.2	Envelope analysis for fault diagnosis	80
5.3	Case 1: manual rotation and spectrum segmentation	81
5.3.1	Raw vibration data at different manual rotation speed conditions	82
5.3.2	Spectrum segmentation	84
5.3.3	Empirical wavelet thresholding	88
5.4	Case 2: vibration signals collected by motor driving	89
5.5	Conclusion	93

6	Vibration Fault Diagnosis Using Iterative Nonlinear Filter and Morphological Analysis	98
6.1	introduction	98
6.2	Background theory	100
6.2.1	Iterative Nonlinear Filter (INF)	100
6.2.2	Morphological analysis	105
6.2.3	Summary of the algorithm and parameter tuning	107
6.2.4	Validation on a small-scale bearing	108
6.3	Experiment and results	109
6.4	Conclusion	113
7	Vibration Fault Diagnosis Using Bayesian Augmented Lagrangian Analysis	115
7.1	Introduction	115
7.2	Theoretical background	118
7.2.1	Sparse Bayesian Learning	118
7.2.2	Bayesian Augmented Lagrangian algorithm for signal denoising	120
7.2.3	Angular resampling	123
7.2.4	Order domain fault diagnosis	124
7.2.5	Summary of the algorithm	125
7.3	Validation experiment	126
7.3.1	Validation on a seeded defect bearing	126

7.3.2	Validation on a simulation experiment	128
7.3.3	Discussion of the BAL denoising	129
7.4	Wind turbine blade bearing fault diagnosis	131
7.5	Conclusions	136
8	Acoustic Emission Fault Diagnosis Using Cepstrum Editing Liftering	137
8.1	Introduction	137
8.2	Theoretical Background	140
8.2.1	Discrete/Random Separation based cepstrum editing liftering (DRS-CEL)	140
8.2.2	Morphological closing envelope	144
8.2.3	Summary of the diagnostic framework and parameter tuning . .	145
8.3	AE signal denoising	146
8.4	Fault diagnosis	150
8.5	Conclusion	151
9	Conclusions and Future Works	153
9.1	Introduction	153
9.2	Conclusions and Comparisons	153
9.3	Future Works and Interesting topics	155
	Bibliography	158

List of Tables

3.1	Summary of the review for main bearings CMFD.	51
3.2	Summary of the survey for gearbox bearings CMFD.	56
3.3	Summary of the review for generator bearings CMFD.	62
5.1	Defect frequencies of the test blade bearing.	84
5.2	Diagnosis accuracy at 3.19 r/min and 3.12 r/min.	93
6.1	Bearing defect frequencies.	109
6.2	DFME of Test 1 and Test 2.	113
6.3	DFME of extensive experiments.	114
7.1	Diagnostic accuracy of Test 1 and Test 2.	136
8.1	AE HIT PARAMETERS OF TEST 1	149
8.2	AE HIT PARAMETERS OF TEST 2	150
8.3	DEFECT FREQUENCIES MATCHING ERROR	151
9.1	Comparisons of different proposed methods.	156

List of Figures

1.2	An example of vibration signals with a 90° rotation angle at (a) 1.34 r/min and (b) 7.39 r/min.	24
4.2	The schematic of wind turbine blade bearings field operations.	71
4.3	Blade bearing test rig (a) front view (b) back view.	72
4.4	Blade bearing test rig with the blade load.	73
4.5	General detection procedure.	73
5.1	Hard-thresholding rule.	80
5.2	Flowchart of the empirical wavelet thresholding and fault diagnosis method.	81
5.3	Wind turbine blade bearing test rig.	82
5.4	The schematic of manual rotation operation.	83
5.5	(a) The raw vibration data plots, (b) the frequency spectrum plots. . .	85
5.6	(a) 0-100 Hz frequency spectrum plots and (b) 0-10 Hz frequency spectrum plots.	86
5.7	Segmentations of frequency spectrums at (a1) 1.2 r/min (a2) 2.1 r/min (a3) 4.1 r/min and (b) empirical wavelet filter bank in the normalized Fourier axis.	87

5.8	(a) raw vibration signal at 4.1 r/min and (b) empirical wavelet thresholding signal and (c) modes extracted by the empirical wavelet transform.	90
5.9	The schematic of motor driving.	91
5.10	raw and recombined vibration data at 3.19 r/min.	91
5.11	The recombined vibration data plots at (a1) 3.19 r/min (a2) 3.12 r/min and the frequency spectrum plots at (b1) 3.19 r/min (b2) 3.12 r/min.	92
5.12	(a) raw vibration signal at 3.19 r/min and (b) empirical wavelet thresholding signal and (c) modes extracted by the empirical wavelet transform.	94
5.13	(a) raw vibration signal at 3.12 r/min and (b) empirical wavelet thresholding signal.	95
5.14	Defect frequencies at (a) 3.19 r/min, (b) 3.12 r/min.	96
6.1	(a) Enlarged raw vibration signal within 0.1s (b) Nonlinear diffusion filtered signal after the first iteration.	103
6.2	(a) Raw vibration signal, and INF denoised signals after the (b) first INF iteration and (c) ninth INF iteration.	105
6.3	(a) INF denoised signal, and different kinds of morphological envelopes: (b) dilation and (c) closing.	105
6.4	The flowchart of the proposed method.	107
6.5	Kurtosis versus iteration k .	108
6.6	High-speed bearing (a1) raw vibration signal (a2) INF denoised signal and (b) frequency spectrum processed by morphological envelope method.	109
6.7	Test 1, (a) raw vibration signal collected under the reciprocating operation condition, (b) recombined signal at 2.13 r/min, (c) nonlinear diffusion denoised signal, (d) DRS denoised signal and (e) INF denoised signal.	110

6.8	Test 2, (a) raw vibration signal collected under the reciprocating operation condition, (b) recombined signal at 1.27 r/min, (c) nonlinear diffusion denoised signal, (d) DRS denoised signal and (e) INF denoised signal.	111
6.9	Test 1 at 2.13 r/min, frequency spectrums processed by (a) INF/morphological closing envelope method, (b) INF/Hilbert envelope method and (c) fast kurtogram/Hilbert envelope method.	112
6.10	Test 2 at 1.27 r/min, frequency spectrums processed by (a) INF/morphological closing envelope method, (b) INF/Hilbert envelope method and (c) fast kurtogram/Hilbert envelope method.	113
7.1	Flowchart of the proposed method for blade bearing fault detection under variable speed conditions.	125
7.2	(a) Raw vibration signal and denoised signals obtained by the (b) DRS method, (c) Fast Kurtogram method and (d) BAL method.	127
7.3	DRS method, Kurtosis VS Filter length and Time delay.	127
7.4	BAL method, Kurtosis VS N and M (a) $\Upsilon = 1$, (b) $\Upsilon = 2$ and (c) $\Upsilon = 3$	128
7.5	The results of sparse coefficients.	128
7.6	Order spectrum obtained by the (a) DRS method, (b) Fast Kurtogram method and (c) BAL method.	129
7.7	Simulation example (a) generated fault signals, (b) noise signal, (c) noise masked fault signals, (d) filtered signal based on linear autoregressive model ($\Upsilon = 1$) and (d) filtered signal based on nonlinear autoregressive model ($\Upsilon = 3$).	130
7.8	Test 1: (a) Gearbox shaft speed (b) blade bearing raw vibration signal, (c) band-pass filtered signal and (d) BAL denoised signal.	132

7.9	3D plan for Υ , N and M . The highest kurtosis is 35078.07 under the conditions of $\Upsilon = 2$, $N = 2743$ and $M = 24$	133
7.10	Test 1 with 0.15 seconds: (a) Raw vibration signal, (b) BAL denoised signal and (c) OMP denoised signal.	134
7.11	Test 1: (a) frequency spectrum (b) order spectrum based on the gearbox shaft speed.	134
7.12	Test 2: (a) Gearbox shaft speed (b) blade bearing raw vibration signal and (c) BAL denoised signal.	135
7.13	Test 2: (a) frequency spectrum (b) order spectrum based on the gearbox shaft speed.	135
8.1	(a) DRS-CEL denoised signal, and its different kinds of envelopes: (b) Hilbert envelope and (c) morphological closing envelope.	145
8.2	The flowchart of the diagnostic framework.	146
8.3	3D plot for kurtosis VS time delay Δ and lifter length M	146
8.4	Test 1, the comparisons of raw AE signal, low-pass edited signal and DRS-CEL denoised signal: (a1) raw AE signal at 1.11 r/min (a2) enlarged raw AE signal (a3) real cepstrum of the raw AE signal (b1) low-pass edited signal (b2) enlarged low-pass edited signal (c3) real cepstrum of the low-pass edited signal (c1) DRS-CEL denoised signal (c2) enlarged DRS-CEL denoised signal and (c3) real cepstrum of the DRS-CEL denoised signal	147
8.5	Different denoised signals by using the (a) DRS method and (b) SK analysis.	148
8.6	Test 2: (a) raw AE signal at 2.69 r/min, (b) DRS denoised signal, (c) band-pass filtered signal by using the SK and (d) DRS-CEL denoised signal.	149

8.7	Test 1 at 1.11 r/min, frequency spectrum process by (a) DRC-CEL/morphological closing envelope, (b) DRC-CEL/Hilbert envelope analysis (c) fast kurtogram analysis and (d) raw signal envelope spectrum.	151
8.8	Test 2 at 2.69 r/min, frequency spectrum process by (a) DRC-CEL/morphological closing envelope, (b) DRC-CEL/Hilbert envelope analysis and (c) fast kurtogram analysis and (d) raw AE signal envelope spectrum.	152

The University of Manchester

Zepeng Liu

Doctor of Philosophy

Wind Turbine Blade Bearing Fault Detection and Diagnosis Using Vibration and Acoustic Emission Signal Analysis

March 12, 2021

Abstract

Over the last few decades, wind energy, as one of the renewable sources, has attracted extensive attention all over the world; and wind turbines are critical devices to convert the kinetic wind energy into electrical energy. Blade bearings, as joint components of wind turbines, play an important role in pitching blades at the desired angles for optimized electric energy output. Blade bearing failure can cause the turbine to lose control or even breakdown which cause curtailment in energy productivity. The assemble and repair costs of blade bearings are high. As a result, condition monitoring and fault diagnosis (CMFD) of wind turbine blade bearings are vitally important to increase the wind turbine production and reduce operation and maintenance (O&M) costs. However, CMFD of wind turbine blade bearings is still at an initial stage due to the following challenges: (1) The rotation speeds of blade bearings are very slow (less than 5 r/min), so the collected fault signals are weak and masked by heavy noise disturbances. (2) Different from constantly rotating bearings, such as main bearings, generator bearings and gearbox bearings, the blade bearing rotation angle is very limited (within 100°) resulting a limited number of fault signals. (3) The disturbances from the blade flapping and dynamic wind loads can cause fluctuating rotation speeds which affect the diagnostic accuracy.

To overcome the aforementioned challenges, we firstly developed an industrial-scale and slow-speed wind turbine blade bearing test-rig, and utilized vibration and acoustic emission (AE) analysis for the fault detection. The test blade bearing is a naturally damaged wind turbine blade bearing which was in operation on a wind farm for over 15 years; therefore, its vibration and AE signals are more in line with field situations.

Then, some novel methods including time-domain analysis, frequency domain analysis and AI methods, are developed to gradually and systematically solve the aforementioned challenges. The proposed diagnostic methods in this thesis are validated by different experiments and case studies. The comparisons with respect to some popular diagnostic methods are explained in detail, which highlights the superiority of our developed methods.

Declaration

No portion of the work referred to in this thesis has been submitted in support of an application for another degree or qualification of this or any other university or other institute of learning.

Copyright Statement

- i. The author of this thesis (including any appendices and/or schedules to this thesis) owns certain copyright or related rights in it (the “Copyright”) and s/he has given The University of Manchester certain rights to use such Copyright, including for administrative purposes.
- ii. Copies of this thesis, either in full or in extracts and whether in hard or electronic copy, may be made **only** in accordance with the Copyright, Designs and Patents Act 1988 (as amended) and regulations issued under it or, where appropriate, in accordance with licensing agreements which the University has from time to time. This page must form part of any such copies made.
- iii. The ownership of certain Copyright, patents, designs, trade marks and other intellectual property (the “Intellectual Property”) and any reproductions of copyright works in the thesis, for example graphs and tables (“Reproductions”), which may be described in this thesis, may not be owned by the author and may be owned by third parties. Such Intellectual Property and Reproductions cannot and must not be made available for use without the prior written permission of the owner(s) of the relevant Intellectual Property and/or Reproductions.
- iv. Further information on the conditions under which disclosure, publication and commercialisation of this thesis, the Copyright and any Intellectual Property and/or Reproductions described in it may take place is available in the University IP Policy (see <http://documents.manchester.ac.uk/DocuInfo.aspx?DocID=487>), in any relevant Thesis restriction declarations deposited in the University Library, The University Library’s regulations (see <http://www.manchester.ac.uk/library/aboutus/regulations>) and in The University’s Policy on Presentation of Theses.

Publications

- 1). **Z. Liu**, B. Yang, X. Wang and L. Zhang, “Acoustic Emission Analysis for Wind Turbine Blade Bearing Fault Detection Under Time-Varying Low-Speed and Heavy Blade Load Conditions,” *IEEE Transactions on Industrial Applications*, pp.1-1, 2021.
- 2). **Z. Liu**, X. Tang, X. Wang, J. Mugica and L. Zhang, “Wind Turbine Blade Bearing Fault Diagnosis Under Fluctuating Speed Operations via Bayesian Augmented Lagrangian Analysis,” *IEEE Transactions on Industrial Informatics*, pp.1-1, 2020.
- 3). **Z. Liu**, X. Wang, and L. Zhang, “Fault diagnosis of industrial wind turbine blade bearing using acoustic emission analysis,” *IEEE Transactions on Instrumentation and Measurement*, vol. 69, no. 9, pp. 6630-6639, Sept. 2020.
- 4). **Z. Liu** and L. Zhang, “Naturally damaged wind turbine blade bearing fault detection using novel iterative nonlinear filter and morphological analysis,” *IEEE Transactions on Industrial Electronics*, vol. 67, no. 10, pp. 8713-8722, Oct. 2020.
- 5). **Z. Liu** and L. Zhang, “Acoustic emission analysis for wind turbine blade bearing fault detection using sparse augmented lagrangian algorithm,” in *2020 IEEE Applied Power Electronics Conference and Exposition (APEC)*, 2020, pp. 145–151.
- 6). **Z. Liu**, L. Zhang, and J. Carrasco, “Vibration analysis for large-scale wind turbine blade bearing fault detection with an empirical wavelet thresholding method,” *Renewable Energy*, vol. 146, pp. 99 – 110, 2020.
- 7). **Z. Liu** and L. Zhang, “A review of failure modes, condition monitoring and fault diagnosis methods for large-scale wind turbine bearings,” *Measurement*, vol. 149, p. 107002, 2020.

Acknowledgements

First and foremost, I would like to thank Dr Long Zhang for his supervision in four years. He led me through the door of wind turbine fault diagnosis and pointed out the new research field to form my PhD project.

I would also like to say thank you to Xuefei Wang, Boyuan Yang, Enze Lu, Kaiji He and Yue liu who helped me to solve the difficulties and do experiments.

My thanks also go to all control systems centre colleagues who accompany me through my PhD study.

Last but not least, thanks must go to my relatives and girlfriend. I probably would have not completed this project without their encouragement and financial support.

Chapter 1

Introduction to Blade Bearing Fault Detections

1.1 Introduction

Wind power, as a reliable and emission-free energy source available in nature, has become the world's fastest-growing renewable energy source leading a way towards a clean energy future [1]. Based on the global wind statistics, the global cumulative installed wind capacity was only 23.9 GW in 2001, but had increased to 651 GW by the end of 2019 and it is estimated to be over 1000 GW by 2024 [2].

At present, there are over a quarter of a million wind turbines in operation and this number will continue to increase in the future [1]. In order to improve the wind energy usage rate and optimize energy yield, modern wind turbine blades can be controlled at desired angles while keeping the main shaft speeds within operating limits via the pitch systems. The blade bearing, also termed pitch bearing, is one of the critical components in the wind turbine pitch system, and it is a typical slewing bearing [3]. The blade bearing inner ring is connected to the blade while the outer ring is mounted on the hub, so the bearing inner rings can be driven by electric motors (electrical pitch systems) or hydraulic equipment (hydraulic pitch systems) to change the blade pitch angle [4]. For the electric pitch system (Fig. 1.1(a)), blades are adjusted by

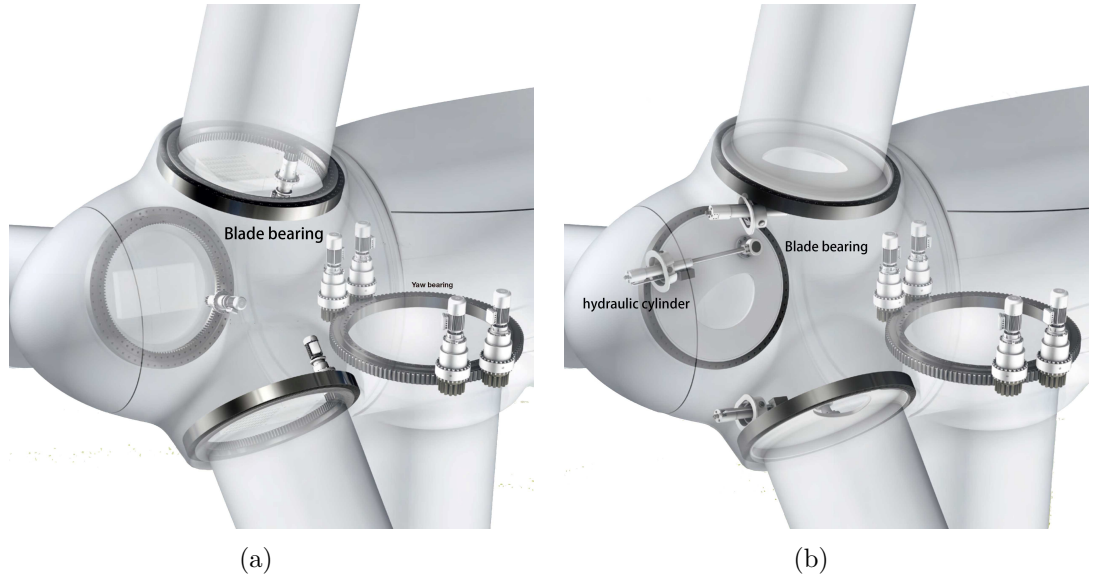


Fig. 1.1. (a) Blade bearing electrical pitch systems and (b) blade bearing hydraulic pitch systems [5].

electric motors driving geared blade bearings. This type of pitch system is particularly advantageous in saving space. The other hydraulic pitch system is that blade positions are pitched by hydraulic cylinders (Fig. 1.1(b)). For this type of pitch system, large bearings without gear teeth are used.

However, blade bearings are usually operated in the extreme and harsh environment, such as moisture, sand, wind gusts and lightning strikes, which can increase their failure rates [6]. The failure of blade bearings can result in lost control of blades and damage of the whole turbine systems. As the repair and replacement costs of failed blade bearings are high, the condition monitoring and fault diagnosis (CMFD) of blade bearings is of critical importance to decrease the operation and maintenance (O&M) cost and improve the system reliability [7]. To achieve this goal, some researchers [8,9] utilized fatigue life analysis as a kind of CMFD tool. Although fatigue life analysis can identify changes of blade bearings' health condition, it requires long-time measurement covering both healthy and deteriorated conditions. Moreover, fatigue life analysis is only suitable in an idealized lab environment. In real-world operations, the working conditions of good blade bearings are usually not recorded for spare use in a long-term. Therefore, the methods used in fatigue life analysis cannot be applied to real wind turbine blade bearing fault detection.

1.2 Challenges and Objectives

Wind turbine blade bearings work at slow rotation speeds with limited angles, so this special working mechanism gives rise to three main challenges which are summarized as follows:

- The fault signals are weak under slow rotation speed conditions (less than 5 r/min) which is due to the fact that low rotation can result in low kinetic energy according to Newton's Law. For example, Fig.1.2(a) and Fig.1.2(b) display raw vibration signals collected from the Blade Bearing Laboratory with 90° rotation angles at 1.34 r/min and 7.39 r/min, respectively. The weak fault signals are masked by the noise generated from bearing rotation motion, gearbox and motor driving. Comparing Fig.1.2(a) and Fig.1.2(b), the fault signals in Fig.1.2(a) at a lower rotation speed are much weaker than those in Fig.1.2(b) at a higher speed.
- The bearing rotation angle is very limited because blade bearings can only swing in small angles (less than 100°), which is different from continuously rotating main bearings, generator bearings or gearbox bearings.
- The blade bearing is controlled by the pitch system to run at constant speed except for its start and end. However, the disturbances from the blade flapping and dynamic wind loads can cause fluctuating rotation speeds. Fault detection methods for constant speeds may tolerate some speed fluctuations but their performances could be deteriorated when the speed variations are beyond their tolerant range. Therefore, non-stationary fault diagnosis methods have to be deployed.

In order to fill the gap of blade bearing CMFD, my PhD study for the first time and at the international forefront, to develop intelligent blade bearing CMFD methods and vibration and acoustic emission (AE) measurements. In particular, my study focuses on addressing the fundamentally challenges related to weak, noisy and non-stationary signal analysis for industry-scale and slow-speed blade bearings. This will be achieved by obtaining the following objectives:

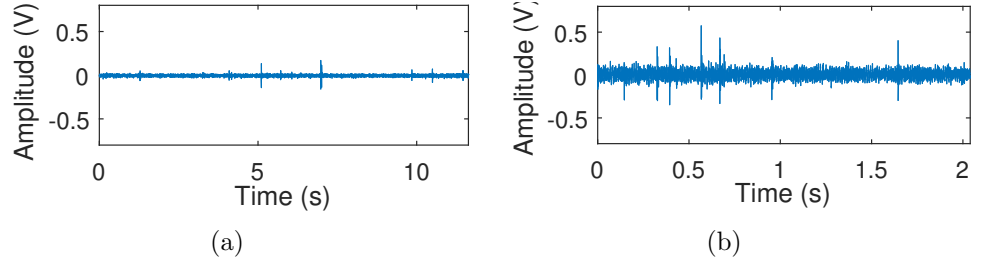


Fig. 1.2. An example of vibration signals with a 90° rotation angle at (a) 1.34 r/min and (b) 7.39 r/min.

- To systematically and comprehensively review current large-scale wind turbine bearing failure modes and condition monitoring and fault diagnosis (CMFD) achievements, which provides a comprehensive references for researchers to better understand the fundamental tribological issues and further enable them to propose or utilize more reliable and cost-effective fault diagnosis methods.
- To develop an industrial-scale blade bearing test-rig and in-situ tools using vibration and acoustic emission measurements. The developed platform can create a solid foundation for blade bearing fault detection and diagnosis.
- To develop new denoising methods (e.g. wavelet based methods and nonlinear filtering methods) and AI methods (e.g. sparse representation methods) for extracting weak fault vibration signals under the conditions of time-varying slow rotation speeds and limited rotation angles. This objective tackles the challenges in blade bearing fault diagnosis by addressing the problems related to weak, noisy, and non-stationary data analysis.
- To develop new cepstrum editing methods for AE signal denoising under constant speeds conditions. The developed method can effectively address the problems related to weak and noisy AE signal analysis.

1.3 Contributions of the thesis

To achieve the objectives of the thesis, the main contributions of the thesis are as follows:

- Systematically reviewed the large-scale wind turbine bearing failure modes and CMFD achievements.
- Development of an industrial-scale blade bearing test-rig and in-situ tools using vibration and acoustic emission measurements.
- Development of new filtering methods and AI methods, empirical wavelet thresholding, iterative nonlinear filter (INF) and Bayesian augmented Lagrangian (BAL) analysis, for extracting weak fault vibration signals under the conditions of time-varying low speeds, limited rotation angles and heavy blade load conditions.
- Development of a novel AE signal denoising method, discrete/random separation based cepstrum editing liftering (DRS-CEL), for blade bearing fault diagnosis under constant speed conditions, which can effectively filter the raw AE signals.

1.4 Thesis Organization

The rest of the thesis is organized as follows. In Chapter 2, the representative failure modes of large-scale wind turbine bearings including main bearings, gearbox bearings, generator bearings, blade bearing and yaw bearings, were systematically and comprehensively reviewed. In Chapter 3, CMFD methods of large-scale wind turbine bearings were presented; within which failure modes, experimental scale and signal processing approaches are summarized. Furthermore, a number of popular condition monitoring and fault diagnosis approaches that can be potentially used for wind turbine bearings are reviewed, followed by a brief summary of future research directions for wind turbine bearing fault diagnosis. Chapter 4 introduced the theoretical background of bearing fault diagnosis and test-rig constructions. Chapter 5 introduced a method called the empirical wavelet thresholding, which can remove heavy noise and extract weak fault signals. In Chapter 6, a novel iterative nonlinear filter (INF) is proposed to remove heavy noise and extract weak fault vibration features. Then, the morphological transform-based envelope method is applied to diagnose the bearing fault in the frequency domain. The diagnostic results were validated under slow-speed and limited rotation angle conditions. In Chapter 7, a novel AI method, Bayesian Augmented

Lagrangian (BAL) Algorithm, is used to build a sparse model for noise reduction. The proposed method was validated by different experiments under slow-speed and heavy blade load conditions. Chapter 8 introduced a novel cepstrum editing method, discrete/random separation-based cepstrum editing liftering (DRS-CEL), to extract weak fault features from raw AE signals. Finally, conclusions and future works were included in Chapter 9.

Chapter 2

Review of Failure Modes for Large-scale Wind Turbine Bearings

2.1 Introduction

Wind turbines, as shown in Fig. 2.1, are made up of mechanical and electrical components to extract kinetic wind energy from the available wind flow in the atmosphere and convert it to electric energy. The most widely used wind turbine design is the gearbox-operated wind turbine, as shown in Fig. 2.1(a). The three blades rotate the main shaft which is connected to the generator via a gearbox. The gearbox can increase rotation speeds up to a typical 1500-1800 rpm, which allows the generator to connect to the electric grid [10]. Another popular design is the direct-drive wind turbine, as shown in Fig. 2.1(b), which lacks a gearbox. Compared with gearbox operated wind turbines, direct-drive turbines eliminate the most complicated gearbox, but the size of the generator becomes larger [11, 12].

The large-scale bearings in wind turbines are critical components supporting heavy loads and handling large moments. Different from general-purpose industrial bearings, these large-scale wind turbine bearings are operated under harsh conditions and mounted at high altitudes with higher failure rates and repair costs [15]. In order to increase wind turbine production and reduce operation and maintenance (O&M)

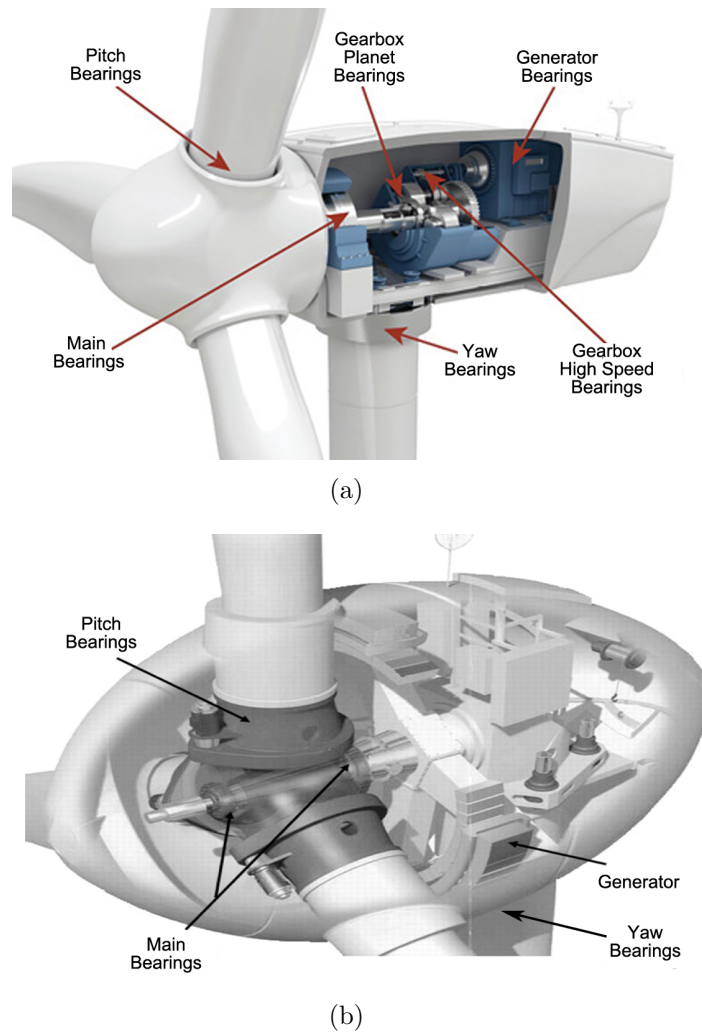


Fig. 2.1. Wind turbine configuration (a) gearbox operated wind turbine [13] and (b) direct-drive wind turbine [14].

costs, condition monitoring and fault diagnosis (CMFD) of these bearings is vitally important to guarantee reliability in wind turbine operations. However, wind turbines have different types of large-scale bearings in terms of their rotation speeds: (i) very slow-speed bearings (yaw bearings and pitch bearings), (ii) slow-speed bearings (main bearings and gearbox low-speed bearings) and (iii) high-speed bearings (gearbox high-speed bearings, gearbox intermediate-speed bearings and generator bearings). Their different rotation speeds and unique working mechanisms lead to different failure modes. Whereas, as the research on wind turbines is still in an initial stage due to its short history, majority CMFD techniques of wind turbine bearings mainly focus on indicating the defective components of the bearing (inner race, outer race and balls) without incorporating the failure mode assessment. Thus, it can cause the immaturity of the developed CMFD techniques. Usually, these techniques can be applied to idealized laboratory environments properly, but may not be utilized for *in-situ* CMFD of wind turbine bearings because of complex failure modes and unique bearing working mechanisms. As a result, it is highly important to classify their failure modes, and then apply sophisticated CMFD techniques.

2.2 Types of large-scale wind turbine bearings

In general, large-scale bearings in wind turbines can be classified into two categories: drive system bearings and adjustment system bearings. The drive system bearings including main bearings, gearbox bearings and generator bearings often use roller bearings with a large capacity to carry heavy radial loads. The adjustment system bearings such as blade and yaw bearings have to use slewing bearings to handle both large thrust and radial loads. The details of large-scale wind turbine bearings are introduced below:

- a) **Main bearings:** The main bearings or main shaft bearings are used to hold the hub and the blades; and they can transmit torque to the gearbox. For modern MW-turbines, the size of the main bearings is usually greater than 1 m,

which is able to support a heavy radial load; therefore, the types of main bearings are normally chosen as spherical roller bearings, cylindrical roller bearings and tapered roller bearings. These bearings can work in a harsh and unstable environment [16]. To reduce the failure rates, the main bearings are supported through frequent greasing with an adequate amount of lubricant.

- b) **Gearbox bearings:** Wind turbine gearbox bearings are used to support shafts in different gear stages i.e. a low-speed stage, intermediate-speed stage and high-speed stage. For different gear stages, the choices of bearings are different, which depend on the type of loads. For low-speed stage bearings, they are usually the largest bearings in the gearbox where the loads they support are subject to the wind turbine main bearings. The suitable types of low-speed stage bearings are cylindrical roller bearings and tapered roller bearings. For the intermediate-speed and high-speed stage bearings, they support heavy radial and axial loads. Tapered roller bearings, cylindrical roller bearings, four-point contact bearing and tube roller bearings are suitable for this application [17].
- c) **Generator bearings:** The generator bearings support the shaft in the generator. They are operated at a high speed, but should have low vibration and good insulating properties [18–20]. Electrical pitting is the first concern when designing generator bearings [21]. In order to solve this issue, there are two common solutions for installing electrically insulated bearings. One is a coated bearing which is designed to perform an insulated treatment on the bearing's ring surface. Ceramic and conductive microfibers are two frequently used insulation materials mounted on the bearing's ring surface. The other solution involves hybrid bearings, where the rolling elements are made by ceramic balls, but the rest of the unit is metal. In addition, some tactics, such as using a conductive lubricant and grounding the bearings, can also reduce electrical damage to generator bearings [22].
- d) **Blade bearings/pitch bearings:** The functions of blade bearings are to pitch the blades, optimize the electrical energy output, and stop the wind turbine for protection if the wind speeds are larger than a cut-out speed. In modern wind turbines, blade bearings are either single line or double lines four-point contact

ball slewing bearings with either internal gear teeth arrangements (electrical pitch systems) or no teeth arrangements (hydraulic pitch systems) [23, 24]. The outer bearing ring is fixed to the hub and the blade is mounted on the inner bearing ring [25].

- e) **Yaw bearings:** The yaw bearings in wind turbines are used to angularly realign the nacelle into the predominant wind direction in order to optimize power input [26, 27]. The types of yaw bearings are a single line or double lines four-point contact ball slewing bearings with external gear teeth arrangements. Electric motors drive a yaw bearing via the gear system to enable wind turbines to track and follow the wind direction.

2.3 Failure modes of large-scale wind turbine bearings

For large-scale wind turbine bearings, different-types of bearings may have different failure modes due to their different designed mechanism and operation conditions. Furthermore, each type of bearings could have multiple failure modes. For these two reasons, it is highly desirable to clearly classify the failure modes in terms of failure mode characteristics and to understand how different data acquisition techniques and signal processing methods can cope with these failure modes, so as to effectively diagnose the faulty bearings of wind turbines. As a result, the investigations of representative failure modes of large-scale wind turbine bearings are presented.

2.3.1 Plastic deformation

Plastic deformation is very complicated and its progress is irreversible [28]. It comes from the motion of dislocations and is controlled by a thermally-activated motion from a large segment of the stress-temperature region [28, 29]. For plastic deformations of bearings, there are two different types. The first is on a macroscale, and happens over a large area of the contact footprint because of either heavy load or misalignment.

The second type is on a microscale where plastic deformation only occurs over a small part of the contact footprint, such as indentation [30]. The specific types of plastic deformation are explained as follows:

- a) **Excessive load/overloading:** Excessive load or overloading can cause some areas of the bearing to wear faster than others [31, 32]. For large-scale wind turbine bearings, transient wind loads can easily give rise to overloading, thus leading to plastic deformations in a bearing. The position of the deformation due to overloading relates to the pitch of the rolling elements [30]. Fig. 2.2 displays the damaging consequence of excessive loads on wind turbine gearbox bearing rolling elements.
- b) **Misalignment:** Misalignment happens when raceway edges are not parallel to the ball wear path which can lead to overheating, vibration and deformation [33]. One common reason for the misalignment is that the crankshaft has elastic deflection which is subjected to inertial force [34]. Fig. 2.3 shows a schema of the misalignment which indicates that the ball path runs from one side of the raceway to the other. Misalignment is a very common problem for drive system bearings as the bearings are mounted on rubber bushings. The bushings may be deflected under the condition of large torque and extreme environment, both of which will cause bearing misalignment [35].
- c) **Loose fit/incorrect seating fit:** Loose fit occurs if a bearing ring is in relative motion to a mounting shaft or house. If the relative motion continues vibrating, fretting will happen and can further lead to adhesive wear and overheating [30, 36, 37]. If the issue is not solved in a timely manner, the looseness will become worse, leading to noise and cracking [37]. Loose fit also happens on drive system bearings because of the deterioration of rubber bushings.

2.3.2 Lubricant

The purpose of the lubricant is to protect the rolling contact surface with a piece of thin oil film, avoiding balls contacting the raceway directly. An effective lubricant



Fig. 2.2. The damaging consequence of excessive load on gearbox bearings roller elements [38].

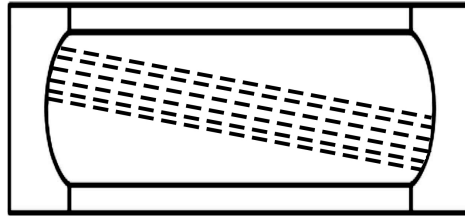


Fig. 2.3. An example of misalignment.

can reduce wears, transport heat generated by friction, extend service life and keep contamination away from bearings [39]. For these purposes, the lubricant is key to maintaining wind turbine bearings, helping them to continue working properly. The followings are two common failure modes:

- a) **Lubricant failure:** The causes of lubricant failures include insufficient lubricant, over-lubricate, inadequate lubricate and using the wrong kind of lubricant [40]. Different lubricants may be incompatible even though each solo lubricant is completely adequate [40]. The direct symptom of lubricant failure is that the surface of ball tracks or balls change to dark color with the odor of burnt petroleum oil [31, 40]. Finally, lubricant failures can lead to excessive wear, overheating, noise and the catastrophic failure of large-scale wind turbine bearings [31, 37, 39–41].
- b) **Lubricant contamination:** Lubricant contamination is another major cause of large-scale wind turbine bearing failures which can dent the bearing raceways. Wear debris, residual particles, dirty lubricants and water are the most common sources of contaminations [42, 43]. Fig. 2.4 shows wear debris particles embedded in the gearbox bearing roller surface.

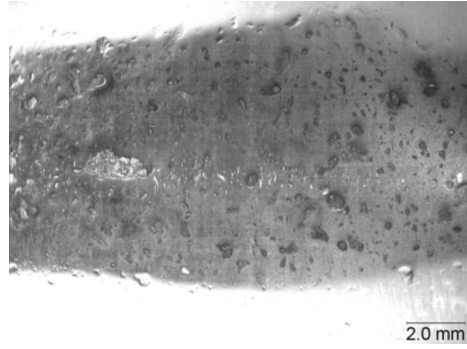


Fig. 2.4. Embedded wear debris particles on the wind turbine gearbox bearing roller surface [38].

2.3.3 Electrical arc erosion

Electric arcing or arc discharge is an electric current breakdown at the connective surfaces between rolling elements and raceway [44]. Electric arc can remove materials from the contact surface [30]. There are possibilities for electric arcing to contain excessive voltage (electrical pitting) and current leakage (electrical fluting); this commonly happens to wind turbine generator bearings [44, 45].

- a) **Excessive voltage/electrical pitting:** Excessive voltage (electrical pitting) is intentionally or accidentally induced by building up particles or charged lubricants. When voltage differences are induced between the bearing house and the shaft because of the dissymmetrical effect, the current subsequently produce sparks and arcing, which could melt the bearing's surface [46].
- b) **Current leakage/electrical fluting:** Current leakage (electrical fluting) occurs from a relatively lower continuous AC or DC current [36, 45], so it is gentler compared with electrical pitting. In the beginning, the damaged surface resembles shallow craters which are closely located. After that, clusters of shallow craters form the equally spaced flutes in a dark color, which can only be found on rollers and raceway surfaces [30]. Fluting is the washboard effect on raceways which causes noise and vibration of the damaged surface [36]. Fig. 2.5 shows a schema of a bearing electrical fluting.

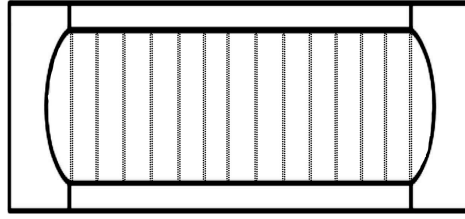


Fig. 2.5. A schema of electrical fluting.

2.3.4 Cracks and fractures

Cracks are the materials failures and fractures are the results of crack propagation. A number of factors, such as temperature, stress concentration, thermal shock and speed of loading, can affect the fractures of materials [47]. Cracks and fractures are the predominant failure modes for large-scale wind turbine bearings, which can lead to significant repair costs. The followings are some specific failure modes of cracks and fractures:

- a) **Forced fracture:** If the stress concentration of the material tensile strength is excessive, the bearing can suffer a forced fracture [30]. White etch cracks (WECs) are a form of forced fracture which may be created by overloaded tensile stresses [48–50]. The appearances of WECs are metallographically similar to butterflies, which can be seen in Fig. 2.6. The connections of small WECs may form larger WEC networks or white structure flaking (WSF) leading to severe noise and vibration [51].
- b) **Fatigue fracture:** Fatigue fracture, also called fatigue failure or spalling (Fig. 2.7), are fractures to the running surface [41,52]. If the limitations of fatigue strength are frequently exceeded through bending, tension or torsion conditions, fatigue fractures can occur [30].
- c) **Thermal cracking:** High frictional heating due to a sliding motion can lead to thermal cracking. Cracks always vertically happen to the bearing movement direction in relation to the contacting surfaces [53]. As a result, misalignments, lubricant failures, contaminations and bearing overheating are the incentives that may cause thermal cracking [53]



Fig. 2.6. Wind turbine gearbox bearing WECs [38].



Fig. 2.7. Fatigue fracture of blade bearing inner raceway [54].

2.3.5 Wear

Wear is another type of material failure, which happens when the base body and counterbody come into contact with poor lubricant [55]. Wear is defined as a continual loss of material by the mechanical action of a solid, fluid or gaseous counterbody [47, 55]. The removed materials are wear particles and debris which can change the bearing frictional characteristics. According to the type of tribological load and removed materials, there are four types of wear process: adhesive wear, abrasive wear, brinelling and corrosion. Table 2.1 gives the typical wear phenomena of these four wear types.

- a) **Adhesive wear:** Adhesive wear happens due to relative motion between contacting surfaces, resulting in plastic deformation and material transfer from one surface to another [30, 36, 58], which can be seen in Fig. 2.8(a). Therefore, adhesive wear modifies the original surface texture [36]. According to different damage levels, the adhesive wear is defined by different names: scuffing, seizing, smearing, skidding and galling. Scuffing indicates the least severe situation. Seizing, smearing and skidding show it middle severe degree (see Fig. 2.8(b)), while galling represents the most serious and extensive plastic flow and metal transfer [30, 36], as shown in Fig. 2.8(c).

Table 2.1

Wear phenomenon of main wear types.

Wear type	Wear phenomenon
Adhesive wear	Material transfer, plastic deformation [55]
Abrasive wear	Scratches, grooves [55]
Corrosion	Red/brown stains or deposits [41]
Brinelling	Indentations [56] [57]

- b) **Abrasive wear/three body wear:** Abrasive wear is also called particle wear or three body wear [30]. The most intensive abrasive wear happens when a soft surface is cut by another hard surface. The second reason occurs when a third hard particle abrades another soft surface [30]. The mechanisms for abrasive wear include microcutting, microfracture, pull-out and individual grains, which are displayed in Fig. 2.9 [47,59]. Therefore, lubricant failures and contamination are incentives to cause wind turbine bearings abrasive wear [60–62]. This can be seen in Fig. 2.10. Adhesive wear and abrasive wear are two common failure modes for wind turbine drive system bearings [63].
- c) **True brinelling/False brinelling:** True brinelling happens when loads are over the elastic limit given to the bearing materials. Indentations in the raceways are called as brinell marks, and can lead to vibration noise. False brinelling is similar to true brinelling, but has no macroscopic plastic deformation. Fig. 2.11(a) shows the schema for true brinelling (left) and false brinelling (right) [56, 57], while Fig. 2.11(b) displays false brinelling on a blade bearing roller surface.
- d) **Corrosion:** Reference [30] defines that corrosion is a chemical reaction to bearing surfaces (Fig. 2.12). Corrosion mainly contains two types which are moisture corrosion and frictional corrosion. The moisture corrosion happens when a bearing is in contact with moisture (water or acid), while frictional corrosion is activated by relative movements between mating surfaces given certain friction conditions [30].

2.3.6 Mounting failure/improper mounting

Improper mounting can cause the imbalance load, improper load distributions, uneven heating and misalignments of bearings [31]. Before installation, it is necessary to

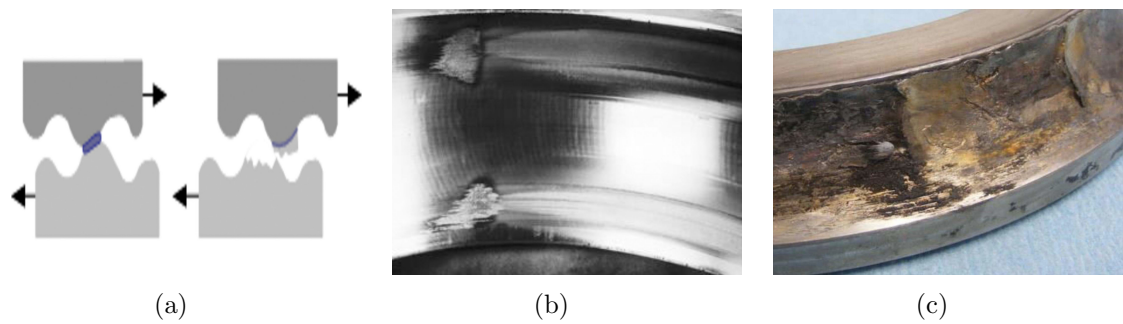


Fig. 2.8. (a) Mechanisms of adhesive wear, (b) smearing of bearing outer ring [64] and (c) galling of bearing outer ring [64].

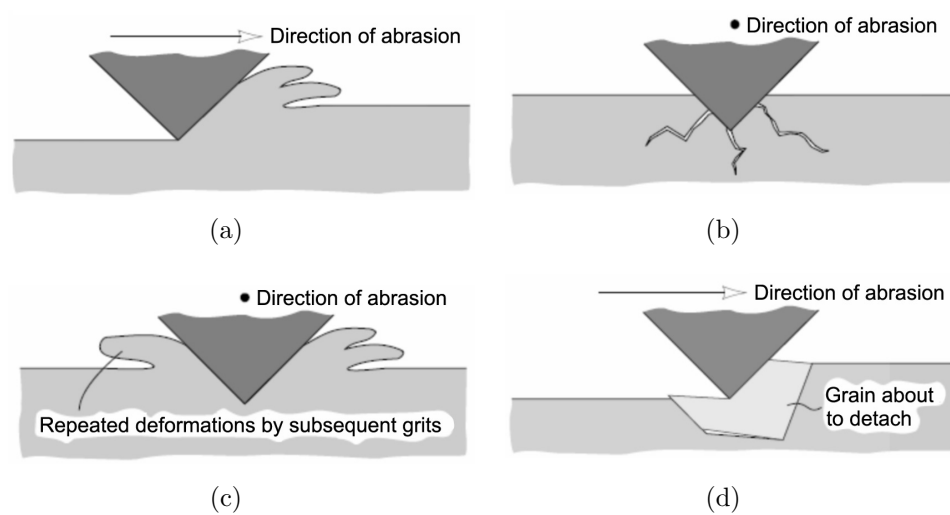


Fig. 2.9. Mechanisms of abrasive wear: (a) microcutting, (b) microfracture, (c) pull-out and (d) individual grains [47].



Fig. 2.10. Abrasive wear of wind turbine gearbox bearing inner raceway with visible dents [38].

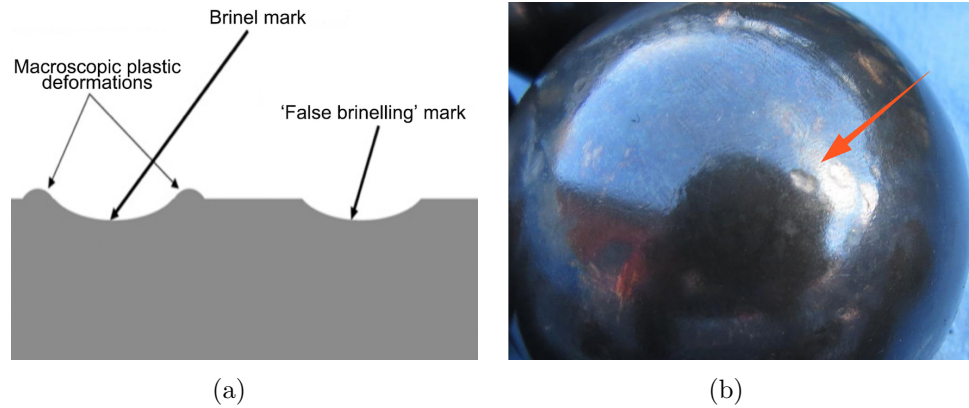


Fig. 2.11. (a) The schema of true brinelling (left) and false brinelling (right) [56, 57] with (b) false brinelling on a blade bearing roller surface [54].



Fig. 2.12. Corrosion phenomenon on a wind turbine gearbox bearing inner raceway [65].

confirm that the size of the shaft and housing are ready for the bearing [66]. A tiny error will lead to unpredictable vibration levels and excessive temperatures. The followings are two possible results of mounting failure:

- a) **Bearing overheating:** Overheating is one of the results of mounting failure generated within the bearing itself which happens on rings, balls and cages. The symptoms are discoloration from gold to blue [53]. Fig. 2.13 gives an example of the overheating blade bearing outer ring surface [54]. The incentives for overheating contain heavy loads, inadequate heat paths and poor cooling systems. As a result, both drive system bearings and adjustment system bearings can easily be subjected to this kind of failure. The inappropriate treatment of overheating has the potential to damage or even explode the wind turbine.
- b) **Inadequate bearing selection:** The possibility of inadequate bearing failure should be taken into consideration after other types of failures have been researched [31, 67]. The most common mistake is choosing a larger or stronger bearing improperly which can easily lead to overloading and vibration.

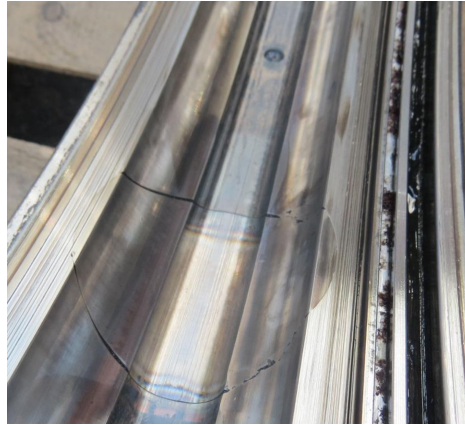


Fig. 2.13. Overheating blade bearing outer ring surface [54].

2.3.7 Failure mode classification

There are many causes and modes for bearing failures which have been introduced in the previous subsections. Normally, one failure is induced via many reasons and there is a combination of causes. During the last decades, the development of tribological research has led to a noticeable increase in outstanding failure mechanisms and failure modes classifications. For example, ISO 15243:2004 [30] classified six groups of failure modes based on bearing failure types. For this thesis, based on the classifications in Refs. [30, 47], the failure modes of large-scale bearings introduced in this chapter are classified into two main aspects: failure of material and premature fatigue (see Fig. 2.14). The failure of materials is caused by components and structures, and can only be reflected with cracks, wear and other similar phenomena [47]. The second aspect is premature fatigue which is based on mechanical failures. All bearing failures not attributed to material failures are attributed to premature fatigue. The majority of topics on premature fatigue are on plastic deformation, improper lubricant, electrical erosion, improper mounting and improper maintenance.

Compared with ISO 15243:2004 [30], Fig. 2.14 provides a more detailed summary and each of the specific failure modes for wind turbine bearings can be easily categorized. However, the faults from wind turbines are not isolated and this type of classification cannot reflect the interrelationship between premature fatigue and material failures. Fig. 2.15 gives four networks illustrating the causes and effects of bearing failure and shows a comprehensive bearing failure analysis.

Table 2.2

Failure modes of large-scale wind turbine bearings [30, 47].

			Drive bearings			Adjustment bearings	
			Generator bearing	Main bearing	Gearbox bearing	Blade bearing	Yaw bearing
Material failure	Cracks and fracture	Forced fracture	X	X	X	X	X
		Fatigue fracture	X	X	X	X	X
		Thermal cracking	X	X	X		
	Wear	Adhesive wear	X	X	X		
		Abrasive wear	X	X	X		
		Corrosion				X	X
		Brinelling				X	X
Premature fatigue	Plastic deformation	Excessive load	X	X	X	X	X
		Loose fits	X	X	X		
		misalignment	X	X	X		
	Electrical arc erosion	Excessive voltage	X				
		Current leakage	X				
	Mounting failure	Overheating	X	X	X	X	X
		Inadequate bearing					
	Lubricant	Lubricant failure	X	X	X	X	X
		Contamination	X	X	X	X	X

After having classified bearing failure modes, it is necessary to conclude the specific fault types of large-scale wind turbine bearings. As mentioned before, large-scale bearings working under different working conditions, such as environment, temperature and load distribution, may generate some particular failures. For the fault diagnosis of wind turbine bearings, if researchers can master these failure modes, it may be easier to identify the particular bearing fault types combining some signal processing analyses and bearing working conditions. Table 2.2 concludes the most common failure modes of specific large-scale wind turbine bearings.

2.4 The failure mode of blade bearings

Blade bearings are critical components of wind turbines which have to bear high bending moments and rotate at very slow speeds. However, they are the weak part and bottleneck for large-scale wind turbines. As can be seen in Table.2.2, the possible failure mode of blade bearings are fracture, abrasive wear, corrosion, excessive load, overheating, lubricant failure and contamination. As a result, it is necessary to develop effective fault detection methods for blade bearings with the aim of reducing the unplanned downtime and maintenance cost, and improving reliability and energy efficiency of wind turbine power generation.

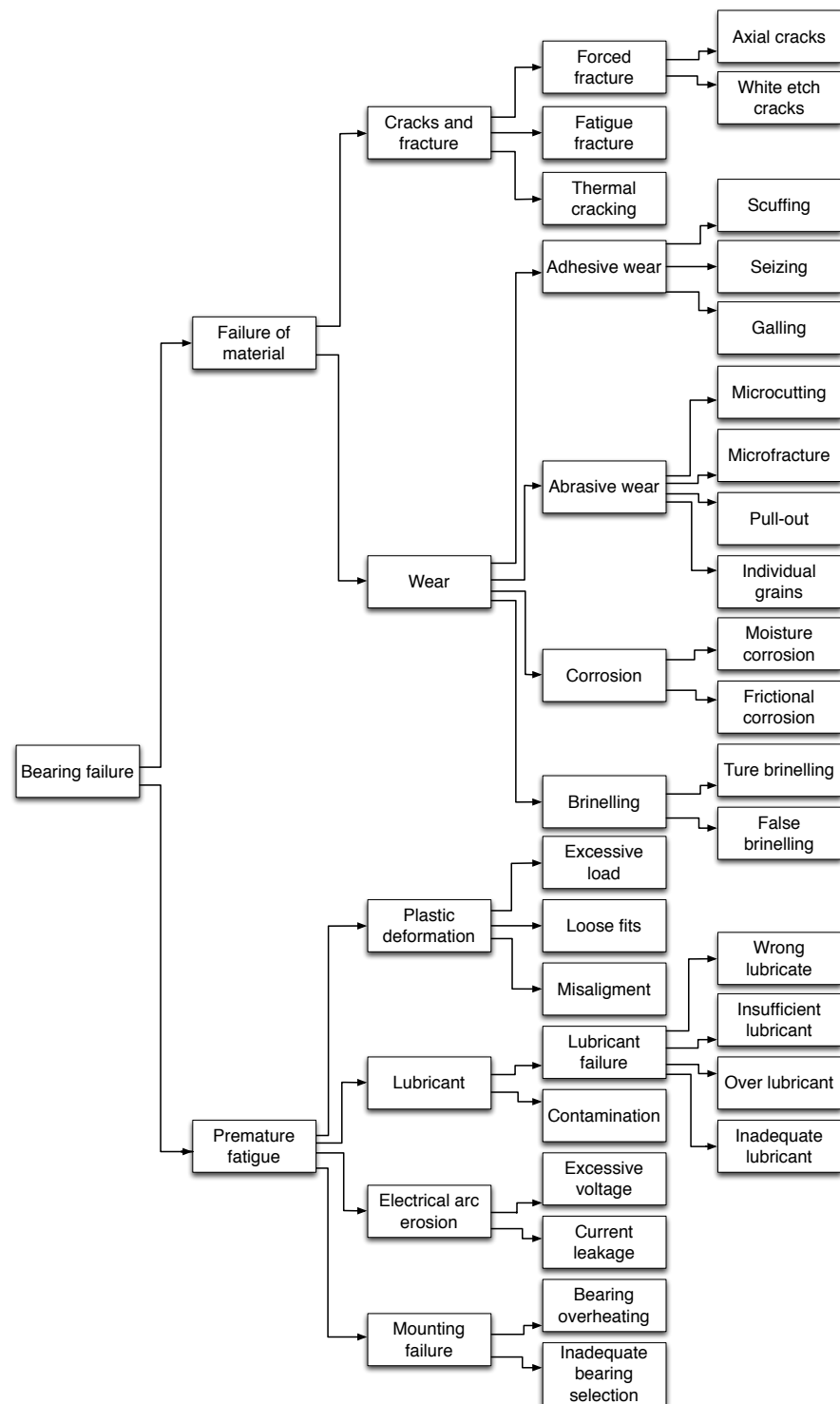


Fig. 2.14. Failure mode classifications of large-scale wind turbine bearings [30, 47].

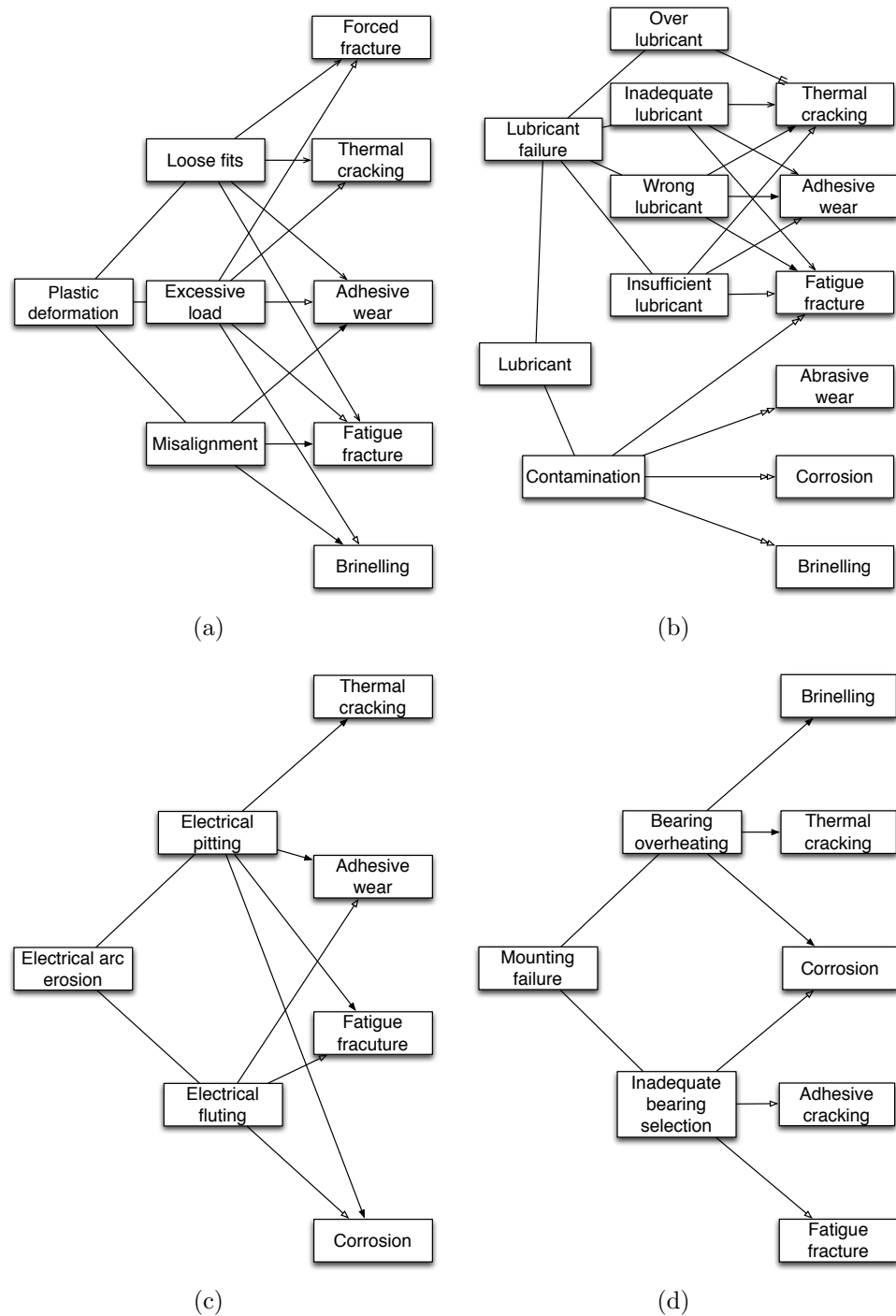


Fig. 2.15. Interrelationships between (a) plastic deformation (b) lubricant (c) electrical arc (d) mounting failure/improper mounting and materials failures [30, 47].

2.5 Conclusion

In this chapter, the literature review surrounding the types of large-scale wind turbine bearings is given firstly. As different-type of bearings may have different failure modes due to their different designed mechanism and operation conditions, the representative failure modes are systematically and comprehensively reviewed which can help to understand the causes and effects of the tribological issues of the large-scale wind turbine bearings.

Chapter 3

Review of Condition Monitoring and Fault Diagnosis for Large-scale Wind Turbine Bearings

3.1 Introduction

In Chapter 2, the failure modes of large-scale wind turbine bearings are classified. In order to evaluate bearing health conditions, it is important to develop CMFD systems which can detect, identify, localize and even prognose the failures of wind turbine bearings [68]. In this chapter, both existing and potential CMFD methods for large-scale wind turbine bearings are summarized. The reviewed articles are extensively searched from Scopus, Sciencedirect, IEEE Xplore, along with an Internet search of articles published using a number of keywords including but not limited to wind turbine bearings, fault detection, condition monitoring and fault diagnosis [12].

3.2 Data acquisition techniques

Data acquisition techniques have been developed to collect failure information using different sensors or equipment. These techniques have been validated for large-scale

wind turbine bearings CMFD including vibration analysis, acoustic emission (AE) analysis, lubricant/debris analysis, power quality analysis and microscope analysis, which are introduced in the following subsections.

3.2.1 Vibration

The vibration happens when a ball strikes a fault in the track which can be applied to warn that failure is occurring. Vibration signals can be collected using vibration sensors including accelerometers, velocity sensors and displacement sensors; accelerometers are the most commonly used sensors [68]. The construction of an accelerometer contains several piezoelectric-crystal elements and a mass. The main characteristic of accelerometers is that they have a wide frequency range. At present, vibration analysis is the most popular and useful measurement for wind turbine bearing condition monitoring, due to its wide frequency range (often 1 to 30 kHz) and easy usage.

3.2.2 Acoustic emission

The publication of [69] reports that if the system has fast pressure pulses with a period of around 5 us, the normal accelerometers may not react accurately because their natural frequencies are not high enough. Although a piezoresistive accelerometer usually has wide bandwidth, from a few hundred Hz to over 130 kHz, this kind of accelerometer generally has low sensitivity [70].

An acoustic emission(AE) transducer works in the frequency range from 20 kHz to 1 MHz [71]. Fundamental to AE is the phenomenon of radiation of elastic wave generation in solids under stress. If the solid undergoes stress over a particular level, the fast release of strain energy will be transmitted in the form of elastic waves which can be collected by the AE sensor [72]. At present, the AE method is already used in small-scale bearing condition monitoring, but there are very few publications on the diagnosis of large-scale wind turbine bearings.

3.2.3 Lubricant/debris

Machinery lubricant systems always include an amount of solid debris which are from surroundings (minerals), component manufacture (core sand, weld spatter, grinding debris) and machinery operation (wear debris). The lubricating oils and grease of large-scale wind turbine bearings can be analysed by using filters, magnetic plugs, spectrographic oil analysis, ferrographic oil analysis, and X-ray fluorescence [73]. Tough or large hard debris potentially initiates rolling contact fatigues, leading to severe surface damage. In order to solve this issue, filtration systems are designed to remove large debris, thus increasing the bearing life cycles. Nonetheless, small debris which is greater than the lubricant film thickness still damages the bearing surface as it is too small to remove. The materials on the bearing surface will be removed after repeated damage by such small debris [74].

3.2.4 Power quality

In the future, wind farms will be required to meet the increasing criteria of grid integration of wind energy, so the power quality of wind energy will become more reliable than before [75]. The faults of mechanical components, such as bearings, can be detected by analysing the power quality of mechanical or electrical energy measured on a shaft or generator [76]. Peak power output, reactive power, voltage fluctuations, current fluctuations and harmonics are the main factors indicating power quality [77]. Also, the Supervisory Control and Data Acquisition (SCADA) system is another method to provide detailed power quality measurements that indicate whether bearings need to be maintained or replaced [78].

3.2.5 Borescope inspection

Borescopes are optical device to help visual inspection of the bearings. They are mostly used in nondestructive testing techniques in order to present defects of the bearings. The photos collected from borescopes can show a visual account of the bearing surface

and conclusive evidence if a bearing is damaged. Inspections could present the failure mode, such as cracks, wears and corrosion [79].

3.2.6 Temperature Monitoring

If there is a damage inside the wind turbine bearing, it will become noisy and further increase the operation temperature. Monitoring temperature can help to find out the incipient faults of the bearing. If the temperature of the bearing rises above the normal temperature, this may be an indication of imminent bearing damage [80].

3.2.7 Other techniques

There are many other data acquisition techniques, such as a shock pulse meter (SPM), sound analysis and jerk measurement, which have been applied to normal bearings, although very few publications have focused on large-scale wind turbine bearings. For future work, these techniques may need researchers to explore the large-scale wind turbine bearings in detail.

3.3 CMFD for main bearings

3.3.1 Vibration signal Analysis

Wind turbine main bearings work under non-stationary conditions with dynamic loadings, so the inconstant vibration signals are commonly transformed into stationary signals or decomposed into several quasi-stationary components with the aim of extracting weak fault vibration features. The current achievements of vibration analysis when used for main bearings basically contain time-frequency-energy analysis (e.g. Ref. [81]), frequency domain analysis (e.g. Refs. [82–84]), time-frequency analysis (e.g. Refs. [85, 86]) and artificial intelligence (AI) methods (e.g. Ref. [87]).

An et al. [81] used the intrinsic time-scale decomposition (ITD) method to decompose

the vibration signal of the non-stationary direct-drive wind turbine main bearing into several proper rotation components. For this, both instantaneous amplitude and frequency are defined. The dynamic features used for fault diagnosis were extracted from the proper rotation components. A lab scale experiment was performed to identify the artificial inner race crack, outer race crack and roller crack of the bearings.

Xin et al. [82] and Pan et al. [83] conducted a similar experiment. They received vibration signals of two main bearings from two 1.5 MW direct-drive wind turbines. One bearing worked normally and the other had a fault. The different characteristics of a normal bearing and a faulty bearing were compared by using cepstrum analysis [82], narrow-band envelope analysis [82] and spectral correlation analysis [83]. However, the authors were unable to diagnose the exact bearing fault type.

Zhang et al. [7] firstly proposed the generalized transmissibility damage indicator (GTDI) method which was based on transmissibility function (TF) analysis. This can be defined as the ratio of spectral of two different output measurements. The advantage of GTDI is that it can eliminate dynamic loadings and noise effects. After that, the authors conducted a field test to diagnose wind turbine main bearings via the proposed method. The results showed that GTDI has the potential for online fault diagnosis because the bearing fault can be rapidly detected (around 1.5 s) without mis-recognition. Based on this technique, Zhang et al. [88] developed a novel wavelet energy transmissibility function (WETF) which can further reduce the effects of non-stationary operations and noise. The results of the analysis can better evaluate the health conditions of wind turbine main bearings.

Bodla et al. [85] proposed Hilbert-Huang transform (HHT), feature extraction and logistic regression (LR) for a real data set of 18 wind turbines to evaluate the health condition of the wind turbine main bearings with an accuracy of 87%. Chen et al. [86] proposed a multifractal method based on the wavelet transform modulus maxima (WTMM) method to investigate the non-stationary vibration signals of wind turbine main bearings. The field test was conducted and the data was collected from a real wind farm. The results showed that incipient fault features can be extracted from a

multifractal spectrum. Han et al. [89] utilized Teager energy operator for signal enhancement and Complementary Ensemble Empirical Mode Decomposition (CEEMD) for signal denoising. A scale-down wind turbine was built, and a seeded crack was induced in the outer race of the main bearing with the aim of validating the proposed diagnostic framework. The results showed that CCEMD could effectively filter the background noise and obtain bearing defect frequency components.

Purarjomandlangrudi et al. [87] combined Anomaly Detection (AD) and Support Vector Machine (SVM) machine learning algorithms for wind turbine main bearings fault detection. The research performed a lab scale experiment proving that the AD method has more ability than SVM to detect incipient bearing faults.

3.3.2 Stator current analysis

For direct-drive wind turbines, the main bearing health conditions can be detected via generator stator current signals; this is because the main shaft is directly connected to the generator and any faults in the main bearings will pollute the generator current signals. The researches of references [90–95] analysed stator current signals to diagnose the main bearings of direct-drive wind turbines.

Gong et al. [90] applied a wavelet filter to stator current signals which can increase the signal-to-noise ratio (SNR) of the raw data and extract incipient faults. Gong et al. [91–93] used stator current power spectral density (PSD) analysis on stator current signals. The method converted the variable fundamental frequency of the stator current into a fixed frequency in order to identify the bearing faults. Wang et al. [94] proposed the multiscale filtering spectrum (MFS) method to transform the time domain signal into energy distribution in the order domain based on the Vold-Kalman filter (VKF) and the bearing fault characteristic orders can be identified from the weighted energy spectrum. Wang et al. [95] applied a current-aided order tracking method to directly extract the shaft rotating frequency from the stator current signal. Based on the extracted shaft rotation frequency, the raw variable speed vibration data can be resampled into a constant vibration signal which can then be easily used for bearing fault diagnosis.

Table 3.1

Summary of the review for main bearings CMFD.

Signals	Ref(s).	Processing methods	Problem(s)	Experiment	Failure modes
Vibration	[81]	ITD	Non-stationary	Lab scale	Inner, outer, roller cracks
	[82]	Cepstrum analysis	Characteristic comparison	Field test	Fault alarm
	[83]	Spectral analysis	Characteristic comparison	Field test	Fault alarm
	[84]	GTDI	Non-stationary/noise	Field test	Fault alarm
	[88]	WETF	Non-stationary/noise	Field test	Fault alarm
	[85]	FFT, HHT and LR	Non-stationary/noise	Field test	Fault alarm
	[86]	WTMM	Non-stationary	Field test	Incipient fault extraction
	[89]	CCEMD	Noise	Field test	Seeded outer race crack
Current	[87]	AD/SVM	Noise	Lab scale	Incipient fault extraction
	[90]	Wavelet filter	Noise	Lab scale	incipient fault extraction
	[91–93]	PSD	Non-stationary	Lab scale	Inner, outer, cage cracks
	[94]	MFS	Non-stationary	Lab scale	Inner, outer, cage cracks
	[95]	Order tracking	Non-stationary	Lab scale	Inner, outer, cage cracks

The references of [91–95] performed lab scale experiments to evaluate the proposed methods which can effectively detect naturally damaged and artificially damaged main bearings. The failure modes of the bearings are outer ring fracture, inner ring fracture and cage fracture.

3.3.3 Summary of the review for main bearings CMFD

The signals used for wind turbine main bearings mainly contain vibration and stator current signals. Table 3.1 provides a comprehensive summary of using these signals for main bearings CMFD. As can be seen, the CMFD techniques for main bearings are merely implemented at the experimental level. Seeded faults can be diagnosed under stationary and non-stationary conditions at relatively high rotation speeds. However, for the field test, the current techniques can only present a fault alarm (e.g. with a distinct fault or without a distinct fault).

3.4 CMFD for gearbox bearings

3.4.1 Vibration signal analysis

A wind turbine gearbox has three stages and each stage produces different bearing rotation speeds. This complicated design heavily increases the difficulty of collecting vibration fault signals because the useful information can be submerged by noise. The

signal processing methods of [96] utilized time domain analysis. Refs. [97–102] used frequency domain analysis and Refs. [103–108] used time-frequency analysis. These can be explained as follows.

Wang [96] proposed the autoregressive (AR) filter for wind turbine gearbox bearing vibration signals. The gearbox noise was eliminated via the AR filter and the fault signals were retained in the residual signals. After that, the envelope method was applied to the filtered signals in order to find the bearing fault frequencies. The data for the research was provided by a lab scale experiment and the bearing inner race spalling was identified.

Xu et al. [100] collected vibration signals of a naturally damaged wind turbine gearbox and its fault type was unknown. After analysing the raw data in both time domain and frequency domain, the authors found that the planetary bearing most likely had faults. Finally, endoscope inspection and disassembly of the gearbox confirmed that the vibration signal analysis was accurate. Antoniadou et al. [98] performed a lab scale experiment to diagnose seeded inner race electrical erosion with 0.2 mm deep and 0.2 mm wide via envelope analysis. Sawalhi et al. [99] presented both the envelope method and cepstrum method to diagnose different stages of wind turbine gearbox bearings. The research data was provided by National Renewable Energy Laboratory (NREL). The results showed that the high-speed stage bearing with overheating, and a minor scratch on the inner raceway and balls were detected; while, the intermediate stage bearings with debris, false brinelling and corrosion were not diagnosed. Jain et al. [101] combined the high-pass filtering and envelope method to process the vibration data of a wind turbine planetary gearbox bearing. The proposed method is able to diagnose the artificial fracture of a bearing's inner raceway and outer raceway. Shanbr et al. [102] combined a fast kurtogram with the envelope method which detected inner race faults on high-speed stage gearbox bearings. Peeters et al. [97] utilized the cepstral editing procedure analysis to separate gears and shaft noise from raw vibration data. After that, envelope spectrum analysis was applied to the denoised signal with the aim of finding the bearing defect frequencies. The data of this research was provided by the NREL. The diagnostic results showed that the faults on intermediate-speed stage bearings and high-speed stage bearings could be confidently identified. However, the

researchers were not confident with the diagnosis results of low-speed stage bearings as the envelope spectrum spike is too small to make any conclusion.

The researches of [103,104] used undecimated wavelet transform and second-generation wavelet transform to decompose wind turbine gearbox bearing vibration signals. Then, a proper analysis, such as frequency analysis or envelope analysis, was applied to the decomposed components in order to identify the bearing fault types. Ref. [103] identified the inner race crack of a high speed gearbox bearing from a field test and Ref. [104] identified the bearing inner race fault from a lab test.

Hu et al. [105] combined ensemble empirical mode decomposition (EEMD) and SVM to diagnose the noise masked non-stationary vibration signals of a wind turbine gearbox bearing. Li et al. [106] combined variational mode decomposition (VMD) and convolutive blind-source separation (CBSS) to process vibration signals of multi-channels. The first stage of [105,106] was to decompose the raw vibration data into a collection of intrinsic mode functions (IMFs). Compared with empirical mode decomposition (EMD), EEMD and VMD have the ability to eliminate the mode mixing problem. Finally, Hu et al. [105] identified an inner race fault, outer race fault and rolling element fault via SVM, while Li et al. [106] diagnosed artificial cracks on bearing outer raceway where the cracks had three different depths (i.e., 1.0, 2.0, 3.3 mm). Additionally, Guo et al. [107] further proposed the local mean decomposition (LMD) to diagnose the high-speed stage gearbox bearing. The LMD was first proposed by Smith to decompose amplitude and frequency modulated signals into a small set of product functions (PFs) [108]. Each PF is defined as the product of an envelope signal and a frequency modulated signal. From PF, a time-varying instantaneous phase and instantaneous frequency can be collected. Similar to the EMD-based approach, LMD can also separate the noise in decomposed PFs. Thereafter, synchrosqueezing transform was applied to convert the defined PF in the time-frequency plane where fault frequencies could be seen. This proposed method successfully diagnosed bearing inner race scratch under non-stationary conditions. Zhang et al. [109] combined VMD and adaptive maximum correlated kurtosis deconvolution (AMCKD) to filter raw vibration signals. The authors conducted different cases studies to validate the proposed diagnostic framework where the damages on inner race and balls were diagnosed.

Teng et al. [110] used artificial neural network (ANN) to train data-driven models in order to predict the remaining useful life of the wind turbine gearbox bearing. The researchers conducted a field test which collected the vibration signals of 1.5 MW wind turbine gearbox bearings. The prognosis results can predict several days before the failure happens. Saari et al. [111] utilized SVM for the bearing fault identification. The diagnostic results showed that the wind turbine gearbox bearing inner race spalling was detected. Ali et al. [112] proposed adaptive resonance theory 2 (ART2) for an unsupervised classification which could classify the degradation of wind turbine gearbox bearing into three status (failure, degraded and healthy). Compared with conventional feature extraction methods, such as time-domain analysis, frequency domain analysis and time-frequency analysis, the proposed method can estimate the bearing degradation level immediately. Li et al. [113] developed a reliability assessment method, degradation-Hidden-Markov model (DHMM), which can provide the guide for wind farms to make optimal operation and maintenance strategies. The advantage of DHMM is that it can achieve the reliability analysis with fewer sampling data when compared with traditional reliability analysis methods, such as Hidden-Markov model (HMM). The author verified the proposed method on a 1.5 MW wind turbine gearbox bearing and found that the bearing began to degradation from the 99th month.

3.4.2 Electrical signal analysis

Zhang et al. [114] used electrical signature analysis (ESA) for monitoring gearbox bearings in wind turbines with the aim of avoiding mechanical noise. The signal processing method of ESA in [114] was the electrical multiphase imbalance separation technique (EMIST) which was able to improve the signal-to-noise-ratio (SNR) of the raw electrical signals by transforming the healthy signals to DC components and measuring the difference between the healthy condition and the faulty conditions of the bearings. After that, bearing fault types can be identified in the EMIST spectrum.

The proposed algorithm was validated by a lab test and a field test. For the lab test, the vibration signals were received from a 25-hp wind drivetrain simulator. The experimental results indicated that the proposed algorithm was capable of diagnosing

a high speed bearing artificial inner race crack and outer race crack (1-2 mm deep and 1 mm wide). In the field test, the authors collected electrical signals for 1.5 MW double-fed induction generators (DFIG). The proposed method can diagnose inner race cracks of high-speed stage bearings and outer race cracks of planetary bearings.

3.4.3 Microscope analysis

Evans et al. [51] designed a large-scale industrial transient test rig to simulate the real working conditions of wind turbine gearbox bearings. Transient speeds with dynamic load were applied to the gearbox bearing which is able to reproduce WECs and WSF on the bearing inner ring. After analysing the WECs and WSF via optical microscopy, the authors deduced that the formation of WECs and WSF relates to the steel cleanliness because MnS associated inclusions (D_{sulf} and D_{Dup}), Duplicates and type D inclusions were the incentive to form WECs and WSF.

Bruce et al. [115] used optical microscopy and electron microscopy to observe the WECs on wind turbine gearbox bearings. The authors found that the WECs are subsurface-initiated by manganese sulphide inclusions.

Gould et al. [116] used X-ray tomography to determine the characteristics of wind turbine gearbox bearing white etching cracks (WECs). After observing four crack networks on the bearing inner ring, three properties of WECs were concluded. Firstly, WECs can be formed in the bearing without direct connection with the bearing raceway. That is to say, the lubricant is not a necessary factor in causing WECs. Secondly, an improper running condition is an element for accelerating the formation of WECs. Lastly, some inclusions in WECs lead to the direction of crack growth.

Gegner et al. [117] applied X-ray diffraction based residual stress analysis on a wind turbine gearbox bearing. The author concluded that the fatigue cracks were induced by brittle spontaneous incipient cracks from the bearing raceway surface.

Table 3.2

Summary of the survey for gearbox bearings CMFD.

Signals	Ref.	Processing methods	Problem(s)	Speed	Failure modes
Vibration	[96]	AR filter	Noise	High	Inner race spalling
	[100]	frequency analysis	Unknown conditions	Low	Fault alarm
	[98]	Envelope analysis	Noise	High	Seeded inner race erosion
	[99]	Envelope/Cepstrum	Noise	High	Inner overheating/scratch
	[101]	High-pass/envelope	Noise	Low	Seeded Inner race cracks
	[102]	Kurtogram/envelope	Noise	High	Inner race fault
	[97]	Cepstral editing	Noise	High	Inner,outer,roller fault
	[103]	Wavelet-based	Noise	High	Inner race crack
	[104]	Wavelet-based	Noise	High	Inner race fault
	[105]	EEMD/SVM	Non-stationary/noise	High	Inner,outer,roller fault
	[106]	VMD/CBSS	Non-stationary/noise	High	Seeded outer race cracks
	[107]	LMD	Non-stationary/noise	High	Inner race scratch
	[109]	VMD and AMCKD	Noise	High	Inner and ball fault
	[110]	ANN	Fault prediction	High	Fault prognosis
	[111]	One-class SVM	False alarms	High	Inner race spalling
Electrical	[113]	DHMM	Reliability assessment method	High	Bearing Degradation
	[112]	ART2	Non-stationary/noise	High	Fault classification
Electrical	[114]	EMIST	Noise	High	Naturally damaged cracks
Microscope	[51]	Optical microscopy	Failure mode properties		WECs and WSF
	[115]	Optical microscopy	Failure mode properties		WECs
	[116]	X-ray tomography	Failure mode properties		WECs
	[117]	X-ray diffraction	Failure mode properties		Fatigue cracks
Lubricant	[118]	Oil debris monitoring	Unknown condition		Spalling

3.4.4 Lubricant/debris analysis

Dupuis [118] utilized oil debris monitoring sensors to diagnose the health condition of a wind turbine gearbox bearing. Large wear debris over $200\text{ }\mu\text{m}$ proved that the bearing surfaces had the fault of spalling. Moreover, the rate of generation for particles could be used as an indicator to evaluate the remaining useful life of the bearing.

3.4.5 Summary of the review for gearbox bearings CMFD

For the CMFD of wind turbine gearbox bearings, signals including vibration, electrical, microscope and lubricant are analysed. Table 3.2 summarizes the survey of gearbox bearing CMFD methods. For vibration and electrical signal analysis, most researches (e.g. Refs. [96–99, 102–107, 109–113]) have investigated fault detection for gearbox bearings on intermediate or high-speed stages. However, the CMFD for low-speed stage bearings (e.g. planetary bearing) is at an initial phase as the rotation speeds are very low (10–15rpm) and the potential fault signals are extremely weak. The only available publications are Refs. [97, 100, 101]. With regard to microscope and lubricant analysis, the properties of WECs, fatigue cracks and spalling are investigated.

3.5 CMFD for generator bearings

3.5.1 Vibration signal analysis

For vibration analysis of generator bearings, the bearing rotation speeds are higher than any other large-scale wind turbine bearings and they may vary heavily during operation. Therefore, a primary difficulty in CMFD of wind turbine generator bearings is to extract fault features from non-stationary and noise masked raw signals. To solve these problems, some researchers (e.g. [119–121]) utilized stochastic resonance (SR) based methods and other scholars (e.g. Refs. [122–127]) used the wavelet transform, EMD, and their variational forms, to process the inconstant signals and minimize noise levels. Additionally, scholars [127–129] used the order tracking technique to resample a non-stationary vibration signal into a stationary or quasi-stationary signal in the order domain (angular domain) which was helpful for further fault diagnosis analysis.

In order to denoise raw signal and extract weak fault features, SR-based methods are developed for wind turbine generator bearing fault diagnosis. The first step of SR is the frequency shift modulation which shifts the original signal with the carrier frequency f_0 to the desired frequency $f_0 + f_1$ and $f_0 - f_1$. Then, some parameter tuning SR methods, such as quantum particle swarm optimization (QPSO) [119] and discrete wavelet transform (DWT) [121], are used to detect the weak fault signals. In this framework, Li et al. [120] developed adaptive SR method based on coupled bistable systems (ACBSR) to further improve the SR filtering performance, which had a great ability to suppress low-frequency and high-frequency interferences. The proposed diagnostic frameworks of Refs. [120, 121] were verified on a high-speed wind turbine generator bearing. The diagnostic results showed that the proposed framework could clear demonstrate bearing inner race defect frequency.

Zimroz et al. [130] utilized the linear regression analysis for the longtime statistical data to implement and interpret the working condition of wind turbine generator bearing. The research triggered two case studies. The first presented the development of a wind turbine generator bearing fault. The second tracked data from a damaged bearing and its replaced bearing. Some differences can be seen before and after the

damaged bearing replaced. Teng et al. [124] conducted a large scale field test for a 2 MW wind turbine generator bearing. The vibration signals were analysed via the cyclic coherence function, conventional demodulation analysis, complex wavelet transform and spectral kurtosis methods. However, only the cyclic coherence function could detect the bearing inner race fault using intensive electromagnetic vibration (EV). The defects were proven after disassembling the bearing. The authors predicted the defective inner race was caused by shaft current corrosion. Liu et al. [128] used both the cyclostationary demodulation method and envelope method to extract defect shock impulses from the converted angular domain signal. The experiment of [128] was a lab test and the inner race fault of direct-driven wind turbine generator bearing was identified.

Sun et al. [122] used the multiwavelet denoising method with the data-driven block threshold technique to extract the defect shock spikes and eliminate noise. The research firstly performed a simulation experiment to prove the efficiency of the proposed method. After that, a field test for a real wind turbine generator bearing was conducted which detected an incipient inner race fault. Cheng et al. [125] proposed the empirical wavelet transform (EWT), combining the advantages of wavelet transform and EMD to extract inherent modulation information by decomposing a noise masked non-stationary signal into mono-components under an orthogonal basis. The research performed three experiments to evaluate the proposed method. The first one was a lab scale experiment which diagnosed the bearing outer ring with one crack. The second experiment was also a lab scale test for compound fault detection which identified outer race spalling and roller scrape. The last experiment was a field test for a real wind turbine generator bearing. Spalling in the outer race was detected. Teng et al. [131] utilized parameterless-based EWT to automatically segment raw vibration signal in the frequency domain. The segmentation approaches were based on the local maxima method and scale-space method that are capable to deal with the massive data. The authors diagnosed a 1.5 MW wind turbine generator bearing where the ball fault, inner race fault and cage fault were diagnosed. He et al. [123] proposed ensemble super-wavelet (ESW) transform to investigate vibration characteristics of wind turbine generator bearings. The ESW was a combination of wavelet transform and Hilbert

transform, which could effectively extract weak fault vibration features. The authors applied a field test for a wind turbine generator front bearing and back bearing. The proposed method could diagnose fault types with a slight scrape defect on the inner race of the front bearing.

Song et al. [127] transformed a non-stationary vibration signal into a stationary angular domain signal and detected impulse in the angular domain by using EMD and Hilbert transform. The generator bearing outer race groove was detected after a lab scale experiment. Mollasalehi et al. [132] applied a field test to acquire vibration signals from a wind turbine generator bearing. The raw data was decomposed via the EEMD method and an outer race fault was diagnosed. Zheng et al. [126] used VMD, a methodology for the adaptive and quasi-orthogonal signal decomposition, which is based on Wiener filtering and frequency mixing. The signal could be decomposed into various modes or IMFs to extract the incipient fault feature. The experiment was a lab scale which concluded an outer race fault in the bearing. Chen et al. [133] implemented VMD for raw signal denoising as it is insensitive to noise and extracts fewer IMFs when compared with EMD. The VMD denoising was verified by two experiments including a simulation and a lab test. The vibration signals of the lab tests were provided by the Case Western Reserve University (CWRU) Bearing Data Center, which were acquired from normal bearings, inner race fault bearings, outer race fault bearings and ball fault bearings. After filtering the raw signals, SVM was utilized in order to classify the bearing fault types. The diagnostic results showed that the combination of VMD and SVM could identify the bearing fault type with the accuracy of 98.75% which was superior to other EMD-based techniques.

Pezzani et al. [129] proposed a novel order tracking technique to resample the non-stationary vibration signal into a stationary signal under the estimated rotor position. This rotor position was obtained from the angle of the voltage vector which was calculated by using the phase-locked loop (PLL) method. Finally, the FFT was applied to the resampled signals in order to identify the specific bearing fault type. To prove the proposed method, the authors conducted a lab scale experiment to collect a 3.5kW permanent magnet synchronous machine (PMSM) electrical signals and faulty bearing vibration signals. The results showed that the proposed method can identify different

sizes of artificial fractures on a bearing outer raceway. The diameter of the fractures are 2 mm, 4 mm and 6 mm. Guo et al. [134] utilized the generator current signal as a reference to resample the non-stationary vibration signal into the stationary signal. As the resampled signal submerged noise interference, an adaptive stochastic resonance (ASR) filter is used to denoise the signal as well as enhance the weak fault signals. To verify the utilized methods, the authors conducted four experiments to diagnose the seeded defect bearings which have different sizes and types of faults.

Liu et al. [135] applied the Integral Extension Local Mean Decomposition (IELMD) method to extract obvious features from non-stationary signals. The experiment was a lab test which detected the generator bearing inner race fracture and outer race fracture. Chen et al. [136] applied the Nonlocal means algorithm (NLmeans) to extract the fault features and minimize the background noise in the time-domain. This approach discovered the inherent repeatability of the fault signals and tried to recover the original fault signals using the average of other similar ones. To demonstrate the feasibility of the NLmeans, the authors applied several simulations and experimental case studies. The results indicated that the generator bearing outer race crack and pitting fault can be diagnosed in both the frequency domain and the order domain.

Yang et al. [137] developed a data-driven fault diagnosis method based on the sparse representation and the shift-invariant dictionary learning for wind turbine generator bearings, which extracted different impulsive components from vibration signals. The advantage of this method is that it can select a proper dictionary without being dependent on prior knowledge. The research performed two experiments. The first research was a lab scale experiment which used an artificial outer ring scratched bearing to prove that the proposed method has the ability to distinguish the bearing health condition. The second experiment was a field test for a real wind turbine generator bearing, which diagnosed that the fault was on the bearing inner race. Sun et al. [138] utilized the sparse representation technique and dictionary learning to denoise the raw signal and extract weak fault signals. The author implemented a field test to diagnose a 2 MW wind turbine generator bearing. The diagnostic results indicated that the bearing most likely had an inner race fault. Guo et al. [139] used the k-means singular value decomposition (K-SVD) technique as the dictionary learning method. The field

test was conducted to validate the proposed method where the bearing outer race spalling fault was diagnosed. Wang et al. [140] improved a new spare representation method for generator bearings under non-stationary conditions. For the new spare representation method, a new dictionary consisting of a time-varying cosine packet has been designed which is able to vary with the shaft rotation frequency. The solved non-zero sparse coefficients related to the bearing fault types. The proposed method was validated by a lab test and a field test. From the lab test, the seeded outer race fault was identified; and from the field test, the naturally damaged generator bearing inner race fault was diagnosed. As a result, the spare representation can diagnose the bearing fault types under stationary and non-stationary conditions, but an improper dictionary choice will limit the success of the sparse representation method.

3.5.2 Electrical signal analysis

The faulty bearing can induce the wind turbine shaft fluctuation and further result in the modulations of the stator current at the bearing defect frequencies. In this scenario, the electrical signal collected from the wind turbine generator can be analysed to diagnose the bearing fault. For example, Shahriar et al. [141] acquired the generator current signal to estimate the bearing rotation speed and resample the non-stationary current signal; therefore, the bearing fault type can be diagnosed in the order domain based on the resampled signal. Amirat et al. [142–147] proposed EMD, EEMD and HHT to diagnose bearing fault types by using the wind turbine generator stator current signal. The signal was decomposed into a number of IMFs, with each of these a mono-component. After locating the most energized mode, the envelope method or statistical criterion analysis was applied to IMFs in order to reveal the generator bearing fault. The authors presented a lab based experiment which used artificial failures of generator bearings to prove that the proposed method has the ability to diagnose bearing fault types. The failures of the bearings were outer race fracture, inner race fracture, cage deterioration and ball deterioration. Chen et al. [148] utilized the modulation signal bispectrum (MSB) for the generator bearing fault diagnosis. The advantage of MSB is that it can avert the misdiagnosis by including phase information of stator current. The diagnostic framework was tested on a wind farm with thirty-three 1.5 MW wind

Table 3.3

Summary of the review for generator bearings CMFD.

Signals	Ref(s).	Processing methods	Problem(s)	Experiment	Failure modes
Vibration	[130]	Linear regression	Fault prediction	Lab scale	Fault alarm
	[119]	SR	Noise	Field scale	inner race fault
	[121]	SR	Noise	Lab scale	inner race fault
	[120]	ACBSR	Noise	Field scale	inner race fault
	[124]	Cyclic coherence function	Noise	Field scale	Seeded inner race corrosion
	[128]	Cyclostationary	Non-stationary/noise	Lab scale	inner race fault
	[122]	Multiwavelet denoising	Noise	Field test	Inner race fault
	[125]	EWT	Non-stationary/noise	Lab/Field	Crack,spaling and scrape
	[131]	Parameterless EWT	noise	Field	Inner, ball and cage fault
	[123]	ESW	Noise	Field test	Inner race scrape
	[127]	EMD/order tracking method	Non-stationary/noise	Lab scale	Outer race groove
	[132]	EEMD	Noise	Field test	Outer race fault
	[126]	VMD	Noise	Lab scale	Outer race fault
	[133]	VMD	Noise	Lab scale	Inner, outer and balls
	[129]	FFT and PLL	Non-stationary/noise	Lab scale	Seeded outer race fracture
	[134]	ASR	Non-stationary/noise	Lab scale	Seeded inner and outer fault
	[135]	IELMD	Non-stationary	Lab scale	Seeded inner, outer fault
	[136]	NLmeans	Non-stationary/noise	Lab scale	outer race crack/pitting
	[137]	Spare representation	Non-stationary/noise	Lab/field	Inner,outer scratch/fault
	[138]	Spare representation	noise	field	Inner race fault
	[139]	Spare representation	noise	field	Outer race spalling
	[150]	Spare representation	Non-stationary/noise	Lab/field	Inner,outer fault
Electrical	[141]	Electrical signature analysis	Non-stationary	Lab scale	Seeded outer race defect
	[142–147]	EMD, EEMD and HHT	Non-stationary/noise	Lab scale	Inner,outer,cage fracture
	[148]	MSB	Non-stationary/noise	Field	Electrical corrosion
SCADA	[149]	Neural network	Fault prediction	Field test	Fault prognosis

turbines. The failures subjected to electrical corrosion were identified.

3.5.3 Supervisory control and data acquisition (SCADA) analysis

Kusiak et al. [149] used neural network algorithms to build fault prediction models for wind turbine generator bearings. The data of bearing's temperature was collected at twenty-four 1.5MW wind turbines over a period of four months. The result of the research predicted 1.5h before the occurrence of any bearing faults.

3.5.4 Summary of the review for generator bearings CMFD

Table 3.3 concludes the survey of generator bearings vibration CMFD approaches. For vibration and current signal analysis, the proposed methods can extract noise masked raw data and diagnose the bearing faults under constant and variable speed conditions. However, only very few publications can be found for SCADA analysis which could be considered as a research direction for wind turbine generator bearings CMFD.

3.6 CMFD for blade bearings and yaw bearings

Wind turbine blade bearings and yaw bearings failure leads to poor pitching, low energy output and turbine shutdown. However, to our best knowledge, there is no standard method and very few publications are available for blade/yaw bearing condition monitoring. The only references about blade bearing fault detection are that Liu et al. [79, 151–153] developed empirical wavelet thresholding method, INF, BAL and DRS-CEL to diagnose a naturally damaged wind turbine blade bearing. Furthermore, the references about fatigue life analysis are summarized as follows. The methods include frequency spectrum analysis [154], circular domain analysis [155], spectrum kurtosis [156], peak-peak value analysis [156], average value analysis [157] and static load-carrying capacity analysis [158], which can detect changes in the condition of the blade/yaw bearing and track the bearing progressive deterioration during the long-time of measurement days by comparing working conditions of the good bearing. However, in practice, the working conditions of good blade/yaw bearing are usually not recorded for spare use. Therefore, there is a gap in blade/yaw bearing condition monitoring as the above-mentioned methods used in the fatigue life analysis cannot be used in real cases.

3.7 Potential CMFD methods for large-scale wind turbine bearings

The previous subsections have comprehensively reviewed existing works on large-scale wind turbine bearings CMFD. However, the technique of wind energy is still in an initial stage due to its recent history. Some popular CMFD methods have been used in other areas, especially in terms of the slow-speed and non-stationary aspects, which can potentially be used for large-scale wind turbine bearings.

With respect to slow-speed operations, it seems that AE signal analysis and lubricant analysis can be potentially used to diagnose high-speed bearing faults at an early stage. In respect of non-stationary operations, the research trend for bearings in CMFD

aims at improving non-linear, non-stationary feature extraction and fault classification algorithms to enhance fault diagnosis sensitivity and selectivity [159].

3.7.1 Slow-speed sensing

- a) **AE:** Recently, there has been a great increase in the research of AE analysis on high-speed rolling element bearings, whereas, the analysis of AE has not been very fruitful on slow-speed bearings, let alone large-scale and slow-speed wind turbine bearings. The main difficulties are as follows. Firstly, the AE signal is not strong and sensitive enough under very low rotation speed conditions. At a very low speed, the AE signal is primarily generated by the friction and rubbing between the rollers and raceway, while at a high speed, the AE signal is generated from the strike between two metal surfaces [160]. Furthermore, the sampling rates of the AE signal are much higher than the traditional vibration technique, normally from 500 KS/s to 40 MS/s. As the rotation speeds are very slow, in order to collect enough useful defect signals, the sampling time needs to take long enough resulting in making data processing difficult. To address these issues, the publications on CMFD of slow-speed bearings via AE signal analysis have been reviewed. Caesarendra et al. [160] reviewed some related articles and their signal processing approaches are mainly of conventional time domain and frequency domain analysis. In the last three years, in order to process a large amount data, some researchers have utilized EMD-based, EEMD-based and wavelet-based time-frequency domain analysis to decompose signals into different time scales, and then some data reduction approaches can be applied, such as Independent Component Analysis (ICA) and Principal Component Analysis (PCA), in order to recover the decomposed AE signals with higher signal-to-noise ratio. For example, Nikolakopoulos et al. [161] applied EMD and the envelope method to diagnose a slewing bearing with an inner race fault. Kang et al. [162] proposed the wavelet package transform to detect slow-speed bearings with different sizes of artificial inner race faults, outer race faults and ball faults. Aye et al. [163] utilized a PCA-based algorithm to successfully detect a bearing fault deterioration under varying slow speed conditions. Žvokelj et al. [164] combined

EEMD and ICA to diagnose an accelerated run-to-failure slewing bearing with rotation speeds of 1 to 8 rpm. This proposed method can successfully diagnose the bearing cracks and spall on an outer ring surface.

- b) **Lubricant:** Monitoring and analysing the contaminations of lubrication plays an important role as it can diagnose the tribological change of wind turbine bearings at an early stage. However, only one related publication [118] can be found for wind turbine gearbox bearings. References are drawn from other publications on slow speed bearings lubricant analysis, as summarized below. Bai et al. [165] analysed the health condition of ship loader slewing bearings and stacking crane slewing bearings via oil analysis. The authors suggested that the contents of Fe and Cr in oil samples were higher than the standard value which indicates the test bearings were worn and extrinsic contaminant particles could be removed from the lubrication by adding extra solvent. Patel et al. [166] applied a lab test to analyse the effect of different liquid contaminants, such as water, diesel, and salt water, in lubrication on the bearing failure. The results show that a high contamination concentration level in lubrication can lead to abnormal shake in the bearing and an increase in temperature.

3.7.2 Non-stationary methods

- a) **Instantaneous angular speed (IAS):** The principle of using an IAS signal as the CMFD tool is that the defects in the rotation machine have an instantaneous impact on the angular speed of the rotatory shaft where the IAS sensors, e.g. optical encoder and hall effect tooth sensors, can be used to detect variations [167]. Therefore, IAS with its great noise suppression performance has attracted significant attentions regarding rotating machines. For example, IAS-based approaches have been developed and verified on high-speed rotors, gearboxes, diesel engines, bearings and motors [168–171]. Li et al. [169] utilized EMD to decompose the IAS signal into several IMFs and applied Autocorrelation Local Ceptrum (ALC) for the fault detection of a multistage gearbox. Zhou et al. [170] proposed EEMD to decompose the IAS signal and applied the envelope method to the defined IMF to diagnose a feed-axis gearbox. However, the drawback of the IAS method is

that the IAS signal is easily disturbed by random load fluctuations, shaft misalignment and structure noise. In order to fill this gap, Li et al. [171] developed an instantaneous angular phase demodulation (IAPD) method which gathers normalization, narrowband filter and Hilbert phase demodulation to pre-process the raw IAS signal with the aim of increasing the IAS estimation accuracy.

- b) **Improved order tracking:** For the CMFD of wind turbines, order tracking has been applied to main bearings and generator bearings which is an effective approach for minimizing the effect of nonstationary speeds. However, this method requires an additional tachometer or encoder to record rotation speeds which will increase the cost. Additionally, the installation of a tachometer may not be convenient for some bearings. As a result, traditional order tracking methods still have some challenges for large-scale wind turbine bearing fault diagnosis. To address these issues, Lu et al. [172] improved a fast and online order analysis (FOOA) to realize nonstationary permanent magnet synchronous motor (PMSM) bearing fault detection. The authors utilized a current sensor to record the rotating phase information from the PMSM sinusoidal current and a microphone to collect the bearing sound signal with the aim of exposing the bearing fault characteristic order for fault identification. Wang et al. [173] proposed a computer-vision-based rotation speed estimation method for motor bearing diagnosis. Firstly, a high-speed camera was used to record and analyse the instantaneous rotating speed (IRS) of the motor. Meanwhile, a microphone was provided for order tracking based on the obtained IRS curve. These improved order tracking methods avoid the installation of a tachometer; however, for wind turbines, the additional instruments also increase measurement costs.
- c) **Tacholeless order tracking:** In practice, due to the technical and economical limitations, some instrumentation based order tracking methods may hardly be satisfied for large-scale wind turbine bearing fault detection. A further improvement is the tacholeless order tracking approach which can extract the speed reference signal from the raw vibration data itself. From Ref. [174], time-frequency representation (TFR) is seen as a powerful and reliable approach for non-stationary signal analysis. Extracting time-frequency curves from the TFR

can be applied to estimate the instantaneous rotating speed. Refs. [175, 176] introduced band-pass filtering methods to extract the instantaneous rotating speed from the raw vibration data where the chosen frequency band contains shaft speed variability. Hu et al. [177] presented a dynamic path optimization based ridge detection (DPORD) to extract the time-frequency curves which can overcome the drawbacks of noise interference and the local optimal. Huang et al. [178] proposed multiple time-frequency curve extraction from the TFR, based on a fast path optimization which is more reliable than single ridge curve extraction. Whereas, the proposed methods above are only applicable with restricted speed fluctuations. For large speed variation conditions, the instantaneous frequency ridges of different components on the time-frequency plane demonstrate spectrum overlap. Wang et al. [174] proposed a tacholeless filtering method with VKF which can separate mono-components from time-varying signals for instantaneous phase extraction. This method is capable of working on larger speed variation conditions. As a result, tacholeless order tracking methods can reduce measurement costs and effectively diagnose variable speed rotation machines; however, these approaches are usually complicated and require massive computation costs.

- d) **Stochastic resonance (SR):** SR is a non-linear phenomenon where a weak signal can be enhanced by adding an optimal amount of noise, as the frequencies of the added noise and the weak signal will resonate with each other to make the weak signal prominent [179]. Therefore, SR is a potential tool for diagnosing large-scale wind turbine bearings with incipient faults. Guo et al. [180] utilized the SR method to filter the vibration signal collected from a permanent magnet synchronous generator (PMSG) bearing. The results show that the proposed method can enhance the weak fault features and facilitate bearing fault identification. Lei et al. [181] employed the adaptive resonance stochastic (ASR) to extract weak fault signatures of a planetary gearbox. The method of ASR is to optimize bistable SR parameters via ant colony algorithms. The ASR incorporated SR weak signal enhancement and overcame untoward SR parameter selections. Qiao et al. [182] developed an adaptive unsaturated bistable SR (AUBSR) to avoid the output saturation of SR. This method has verified high

speed bearings with slight flaking faults and a planetary gearbox with a chipped tooth and a missing tooth.

These methods proposed above have effectively been proved on high-speed rotation machines, but their sensitivity, validity and feasibility still need to be verified on wind turbine bearings with slow variation speeds and large dynamic loadings.

3.8 Summary

In summary, the current CMFD achievements of large-scale wind turbine bearings are reviewed in order to present full-scale information for related researchers. Tables 3.1 to 3.3 compare different research cases based on data acquisition techniques, signal processing methods, main problems, experiment scale and failure modes. From Tables 3.1 to 3.3, some experiments can be seen as valid for specific failure modes (e.g. fracture, cracks, and electrical erosion); whereas, for the majority of researches, they only limit identifying bearing fault types (e.g. inner race fault, outer race fault and ball fault) or fault alarms (e.g. with distinct fault and without distinct fault).

With respect to potential CMFD approaches, two main research directions which are slow-speed sensing and non-stationary operations applied to traditional rotation machines are summarized. The knowledge of these applied techniques can be used as a reference for large-scale wind turbine bearings fault diagnosis.

Chapter 4

Detection Principle and Test-rig Facility

4.1 Introduction

This chapter introduces the theoretical background of bearing fault diagnosis and the test-rig construction. The three key parameters, f_o outer race defect frequency, f_i inner race defect frequency and f_b balls defect frequency, are discussed in detail. The test rig construction and data acquisition systems are described.

4.2 Bearing defect frequencies

Ball bearings, as shown in Fig. 4.1, are made up of outer races, inner races and rolling elements (e.g. balls). When the irregularity appears during rotation, it will cause a variety of impacts repeating periodically at a rate known as the fundamental defect frequency [184, 185]. The defect types can be divided as outer raceway defect, inner raceway defect, ball defect and combination defects. Different bearings have different fundamental defect frequencies which relate to their mechanical dimensions. The defect frequencies at the given rotation speed are demonstrated by the product of fundamental defect frequencies and the bearing rotation speed [186]. In the frequency

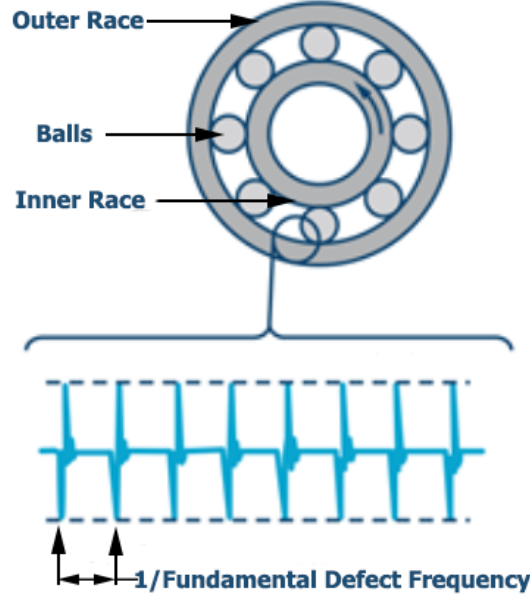


Fig. 4.1. The schematic of the blade bearing and defect signals. [183].

domain, if the signal has one or more dominant frequencies matching one of the defect frequencies, a certain fault type can be inferred [187]. The formulas for these defect frequencies are given as below [186]:

$$f_o = \frac{N_b}{2} \cdot \left(1 - \frac{d_b}{d_p} \cos \alpha \right) \cdot f_r \quad (4.1)$$

$$f_i = \frac{N_b}{2} \cdot \left(1 + \frac{d_b}{d_p} \cos \alpha \right) \cdot f_r \quad (4.2)$$

$$f_b = \frac{d_p}{2d_b} \cdot \left(1 - \left(\frac{d_b}{d_p} \cos \alpha \right)^2 \right) \cdot f_r \quad (4.3)$$

where f_o indicates the outer race defect frequency, f_i is defined as the inner race defect frequency and f_b is defined as the balls defect frequency. f_r is the rotational frequency of the bearing. N_b is the number of rolling elements; d_b is the rolling element diameter; d_p is the pitch diameter and α is the contact angle.

4.3 Test-rig Construction and Components

The real-world blade bearing operations include the starts, constant rotation, stops and direction changes. As can be seen in Fig. 4.2, blade bearings can be rotated back and forth within 100° , and rotation speeds can be controlled from 1 r/min to 2.5 r/min.

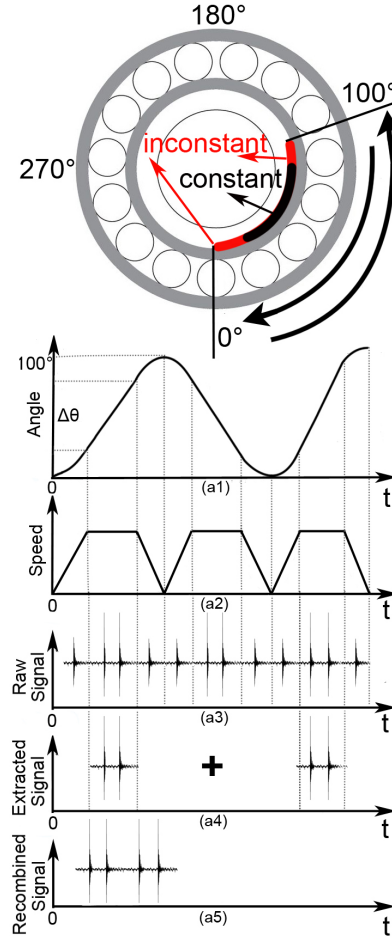


Fig. 4.2. The schematic of wind turbine blade bearings field operations.

The starting and stopping periods are inconstant and noisy, and only the middle part, e.g., 90° , is constant or quasi-constant. To avoid negative impacts caused by starts and stops, the work of this thesis is to investigate whether it is possible to diagnose the blade bearing fault types when non-stationary signals generated from starts and stops are abandoned, and only constant rotation parts are utilized. The blade bearing can be driven by the reciprocal motion to repeatedly collect the vibration characteristics of the same portion (Fig. 4.2(a3)). The same constant speed short portion collected from each swing can be recombined to extend the data length (Fig. 4.2(a4) and (a5)).

In order to imitate the configuration of a blade bearing pitch system, the authors designed a blade bearing lab at the University of Manchester, as shown in Figs. 4.3 and 4.4. The test wind turbine blade bearing was manufactured by Rollix, and was operational on a wind farm for over 15 years. The defects of the bearing were therefore naturally damaged under real wind turbine working conditions. The weight of this

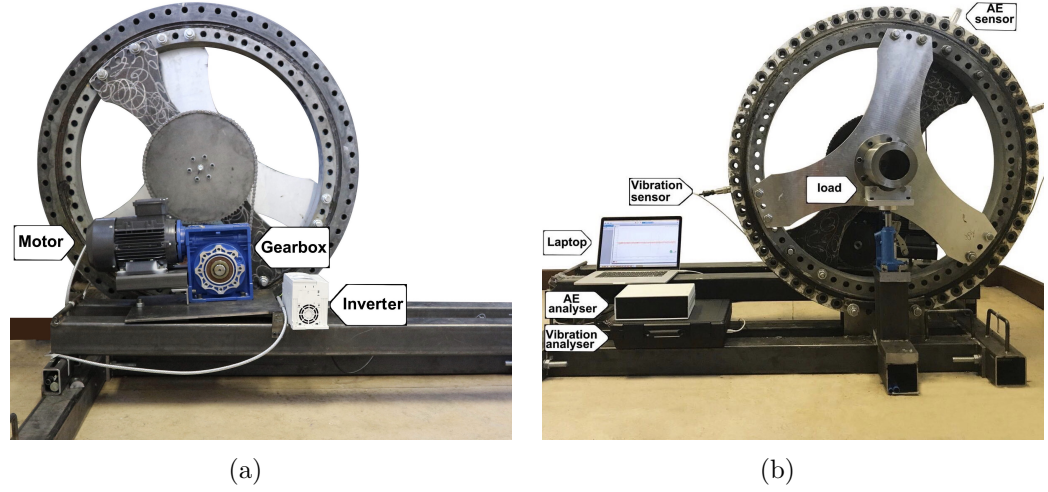


Fig. 4.3. Blade bearing test rig (a) front view (b) back view.

bearing is 261 kg and its pitch diameter, ball diameter, ball numbers and contact angle are 1000 mm, 54 mm, 60 and 50° respectively. Based on these geometric parameters, the bearing defect frequencies at different rotation speeds can be calculated using (4.1) to (4.3).

During the experiment, the outer ring of the bearing is fixed on the test rig, so the inner ring can be rotated for fault diagnosis. As can be seen in Fig. 4.3(a), the kinematic components of the test rig include the three-phase induction motor, gearbox and the blade bearing. The motor has the ability to drive the bearing in the test. Due to the gearbox, the maximum bearing rotation speed is reduced to 5 rpm. The motor inverter can adjust bearing rotation speeds from 0.5 rpm to 5 rpm. Fig. 4.3(b) displays the back view of the test rig. As can be seen, the bearing load can be adjusted via a jack [79,153]. In addition, as can be seen in Fig. 4.4, we can also assemble a real wind turbine blade (7.75 meter long and 139 kilogram) for a load. This design can imitate the blade bearing pitch process under more dynamic working conditions [152]. To the best of the author's knowledge, it is the first industrial-scale wind turbine blade bearing test rig in the UK.

To diagnose the bearing fault type, a self-designed data acquisition (DAQ) system is used to collect bearing vibration and AE signals and also involved accelerometers and AE sensors, as shown in Fig. 4.3(b). The accelerometers and AE sensors are mounted on the bearing outer ring surface. The accelerometer is Hansford HS-100-type sensor

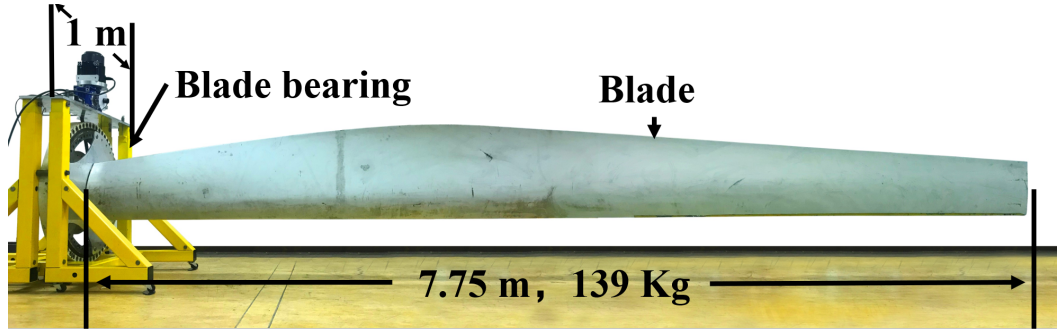


Fig. 4.4. Blade bearing test rig with the blade load.

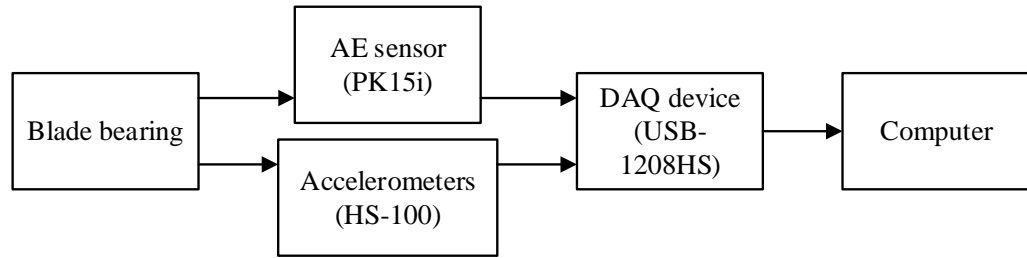


Fig. 4.5. General detection procedure.

with the frequency response from 2 Hz to 10 kHz. The AE sensor is PK15I type sensor with the frequency range from 10 kHz to 500 kHz. The collected signals are transmitted from the sensors to a laptop through the USB communication. A high-speed DAQ device named “USB-1208HS” is used, which can sample data up to 1 MS/s, and in this thesis, we implement 100 kS/s as the sampling rate. Furthermore, the acquired vibration and AE signals are saved using the DAQami software and analyzed using the MATLAB software [151]. Fig. 4.5 displays a flowchart which can show the general detection procedure.

4.4 Conclusion

In conclusion, the detection principle of bearing fault diagnosis is firstly introduced in detail. Then, the test rig construction and data acquisition systems are explained. The advantages of the built test rig is that, to the best of the author’s knowledge, it is the first industrial-scale wind turbine blade bearing test rig in the UK. Furthermore, the test blade bearing is naturally damaged and so it demonstrates real blade bearing vibration and AE characteristics. Lastly, the test rig can simulate blade bearing

pitch process under time-varying low speed and heavy blade load conditions. The disadvantage of the test-rig is that the noise conditions are simpler than the field tests.

Chapter 5

Vibration Fault Diagnosis Using Wavelet Filtering

5.1 Introduction

Wind turbine blade bearings work in a severer environment because they are exposed in harsh circumstances, such as moisture, sand, wind gusts and lightning strikes. Blade bearing failure leads to poor pitching and aerodynamic imbalance of blades. In serious cases, blades may lose control and crack which cause curtailment in energy productivity. The assemble and repair costs of blade bearings are high; therefore condition monitoring and fault diagnosis (CMFD) of wind turbine blade bearings are often needed in order to increase the wind turbine production and reduce operation and maintenance (O&M) costs [188]. However, CMFD of wind turbine blade bearings is still at an initial stage because of the following challenges:

- The effective vibration data is very limited because blade bearings swing in small angles.
- The fault signals are weak under slow rotation speed conditions (less than 5 rpm). This is because that low rotation results in low kinetic energy according to Newton's law.

To address these issues, vibration analysis is utilized in our project to collect the vibration characteristics of the wind turbine blade bearing, because it is a promising technique for rotating machine CMFD. Moreover, in order to improve the reliability of vibration analysis, various kinds of fault diagnosis methods are developed. According to Ref. [189], fault detection and diagnosis can be divided into two main categories: observer-based diagnosis and signal-based diagnosis. In regard to observer-based approaches, such as sliding mode observer and Laplace ℓ_1 Huber based filter, they can identify the fault types based on the inconsistency between the model-predicted outputs and the measured outputs of the practical systems. Nonetheless, these methods require the dynamic and physical parameters of the bearings which may not be practicable in some cases.

The other category is the signal-based diagnostic approach, so fault signal detections are often accomplished by denoising and feature extraction. The conventional signal-based diagnostic method is band-pass filter method, so the filter band determination is a vital process. At present, there are numerous approaches to determine the filter. One of the useful method is the short-time Fourier transform (STFT) which can draw a 3-D plot to specify complex signal amplitude versus frequency and time. Based on this 3-D plot, the optimal frequency band can be determined. However, the calculation speed of this method is often very slow, especially for a large amount of vibration data. To overcome this issue, Antoni proposed the fast kurtogram method which can quickly determine the defect signal frequency range [190], but its resolution is often less than STFT. In recent years, some scholars have utilized SFTF and fast kurtogram to develop tachometer-based or tachometer-less methods which can diagnose the bearing fault types with or without measured rotation speeds [190–195]. However, the drawback of these band-pass filtering methods is that frequency components beyond the determined frequency band are rejected meaning that some fault signals may be degraded which may affect the diagnostic accuracy. Drawing on these insights, in this chapter, we propose a new method, empirical wavelet thresholding, to minimize the heavy noise as much as possible so that the weak fault signals can be extracted.

The new denoising method, empirical wavelet thresholding, is the combination of

the empirical wavelet transform and the wavelet thresholding, which denoises extracted modes by thresholding in the wavelet domain. The recently-developed empirical wavelet transform was firstly proposed by Gilles which is based on segmentation of the Fourier spectrum [196]. As a result, the way to segment the Fourier spectrum or to detect the boundaries is very important. So far, segmentation approaches are mainly based on algorithm, such as local maxima [196], lowest minima [197], histogram segmentation [198] and scale space [199], but these approaches still have some drawbacks. For the parameter-based approaches (e.g. local maxima, lowest minima), the main difficulty is to choose a suitable amount of boundaries for long sampling time vibration signals. For the parameterless-based algorithm (e.g. histogram and scale space), they can automatically select the number of modes, but the calculation speed is very slow. In this chapter, in order to overcome these issues, a novel experimental-based methodology for the spectrum segmentation is investigated. Firstly, the energy distribution of potential fault signals can be analysed under a low noise environment so that the boundaries can be determined based on the properties of fault signals. Secondly, the extracted modes are denoised and reconstructed according to the wavelet thresholding. By utilizing the proposed method, the noise level can be reduced to minimum and the defect frequencies can be seen distinctly in the frequency domain of the reconstructed signals [151].

5.2 Theoretical background

5.2.1 Empirical wavelet thresholding

The empirical wavelet transform develops from the Empirical Mode Decomposition (EMD), which designs a family of wavelets to adaptively extract different signal modes [196]. Therefore, the empirical wavelet transform ensures that each extracted mode inherits the property of wavelet transform and can be denoised by thresholding in the wavelet domain.

Considering the Fourier point of perspective, in order to extract different modes, the

designed wavelets are equivalent to construct a family of corresponding filters. To explain the idea of empirical wavelet transform, the normalized Fourier axis having a 2π periodicity is considered and the derivation is limited to $\omega \in [0, \pi]$ because of Shannon criterion. Assuming the Fourier support $\bigcup_{n=1}^N \Lambda_n = [0, \pi]$ is partitioned into N contiguous segments where each segment is expressed as $\Lambda_n = [\omega_{n-1}, \omega_n]$. The way to determine the number of segments N will be introduced in Section 5.3. The empirical wavelets are built based on the construction of both Littlewood-Paley and Meyer's wavelets which are also defined as a series of bandpass filters on each segment Λ . The Fourier spectrum of the empirical scaling function Φ_0 and the empirical wavelets Ψ_n are defined as follows [196]:

$$\Phi_0(\omega) = \begin{cases} 1 & \text{if } |\omega| \leq (1 - \gamma)\omega_1 \\ \cos[\frac{\pi}{2}\beta(\frac{1}{2\gamma\omega_1}(|\omega| - (1 - \gamma)\omega_1))] & \text{if } (1 - \gamma)\omega_1 \leq |\omega| \leq (1 + \gamma)\omega_1 \\ 0 & \text{otherwise} \end{cases} \quad (5.1)$$

and

$$\Psi_n(\omega) = \begin{cases} 1 & \text{if } (1 + \gamma)\omega_n \leq |\omega| \leq (1 - \gamma)\omega_{n+1} \\ \cos[\frac{\pi}{2}\beta(\frac{1}{2\gamma\omega_{n+1}}(|\omega| - (1 - \gamma)\omega_{n+1}))] & \text{if } (1 - \gamma)\omega_{n+1} \leq |\omega| \leq (1 + \gamma)\omega_{n+1} \\ \sin[\frac{\pi}{2}\beta(\frac{1}{2\gamma\omega_n}(|\omega| - (1 - \gamma)\omega_n))] & \text{if } (1 - \gamma)\omega_n \leq |\omega| \leq (1 + \gamma)\omega_n \\ 0 & \text{otherwise} \end{cases} \quad (5.2)$$

where $\beta(x) = x^4(35 - 84x + 70x^2 - 20x^3)$ and $\gamma < \min_n(\frac{\omega_{n+1} - \omega_n}{\omega_{n+1} + \omega_n})$ are determined to make the filter bank tight [196].

Therefore, the approximation coefficients $a(0, m)$ are given by the convolution between the raw vibration signal $f(m)$ and the empirical scaling function:

$$\begin{aligned} a(0, m) &= f(m) * \phi_0(m) \\ &= \sum_{\tau=0}^{\infty} f(\tau)\phi_0(m - \tau) = \mathcal{F}^{-1}(F(\omega) \times \Phi_0(\omega)) \end{aligned} \quad (5.3)$$

where $F(\omega) = \mathcal{F}(f(m))$ and $\phi_0(m) = \mathcal{F}^{-1}(\Phi_0(\omega))$, and $\mathcal{F}(\cdot)$ and $\mathcal{F}^{-1}(\cdot)$ correspond to the discrete Fourier transform (DFT) and the inverse discrete Fourier transform (IDFT), respectively.

In the same way, the detail coefficients $d(n, m)$ are expressed as follows:

$$d(n, m) = \sum_{\tau=0}^{\infty} f(\tau) \psi_n(m - \tau) = \mathcal{F}^{-1}(F(\omega) \times \Psi_n(\omega)) \quad (5.4)$$

where $\psi_n(m) = \mathcal{F}^{-1}(\Psi_n(\omega))$.

The next step is to use the wavelet thresholding method to reduce the noise wavelet coefficients to zero. There are two common wavelet threshold techniques which are hard and soft thresholding where only the hard-thresholding method has the property to retain the original amplitudes of defect signals without any distortion which can be used for the bearing fault extraction. The hard-thresholding functions applied to approximation coefficients and detail coefficients are described as [200]:

$$a_{\text{thres}}(0, m) = \begin{cases} a(0, m) & \text{if } |a(0, m)| > T(0) \\ 0 & \text{if } |a(0, m)| \leq T(0) \end{cases} \quad (5.5)$$

and

$$d_{\text{thres}}(n, m) = \begin{cases} d(n, m) & \text{if } |d(n, m)| > T(n) \\ 0 & \text{if } |d(n, m)| \leq T(n) \end{cases} \quad (5.6)$$

where $T(r), r = 0 \dots n$ is the new designed universal threshold given by [201]

$$T(0) = \frac{\sqrt{2 \log m} \times \text{median}(a(0, m))}{0.45} \quad (5.7)$$

and

$$T(n) = \frac{\sqrt{2 \log m} \times \text{median}(d(n, m))}{0.45} \quad (5.8)$$

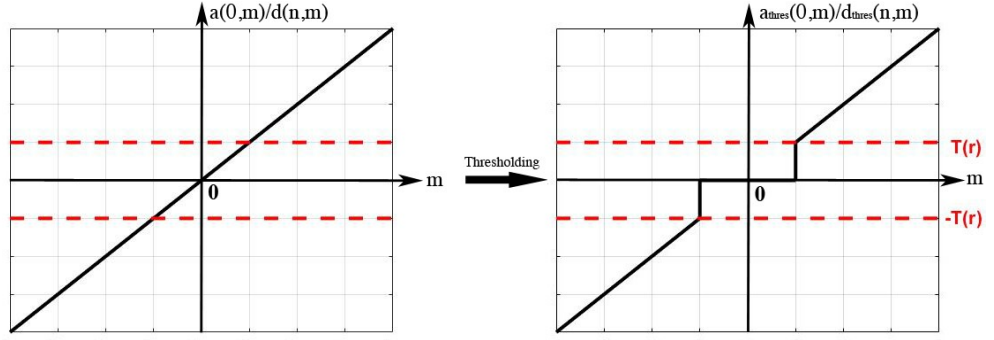


Fig. 5.1. Hard-thresholding rule.

Fig. 5.1 shows the hard-thresholding rule. Finally, the hard-thresholding coefficients can be reconstructed via the wavelet reconstruction method to obtain the empirical wavelet thresholding signal $f_{\text{thres}}(m)$:

$$\begin{aligned}
 f_{\text{thres}}(m) &= \sum_{\tau=0}^{\infty} a_{\text{thres}}(0, \tau) \phi_0(m - \tau) + \sum_{n=1}^N \sum_{\varsigma=0}^{\infty} d_{\text{thres}}(n, \varsigma) \psi_n(m - \varsigma) \\
 &= \mathcal{F}^{-1}(A_{\text{thres}}(0, \omega) \times \Phi_0(\omega)) + \sum_{n=1}^N (\mathcal{F}^{-1}(D_{\text{thres}}(n, \omega) \times \Psi_n(\omega)))
 \end{aligned} \tag{5.9}$$

where $A_{\text{thres}}(\omega) = \mathcal{F}(a_{\text{thres}}(m))$ and $D_{\text{thres}}(\omega) = \mathcal{F}(d_{\text{thres}}(m))$.

5.2.2 Envelope analysis for fault diagnosis

After denoising the raw vibration signal via the empirical wavelet thresholding, the next process is to extract the envelope of the denoised signal and the defect frequencies can be seen in the frequency spectrum of the envelope. Specifically, the Discrete Hilbert transform (DHT) of the denoised signal $f_{\text{thres}}(m)$ is [202]

$$\mathcal{H}[f_{\text{thres}}(m)] = \mathcal{F}^{-1} \{ \mathcal{F}[f_{\text{thres}}(m) \times u(m)] \} \tag{5.10}$$

where $\mathcal{H}[\cdot]$ indicates the DHT, and $u(m)$ is defined as:

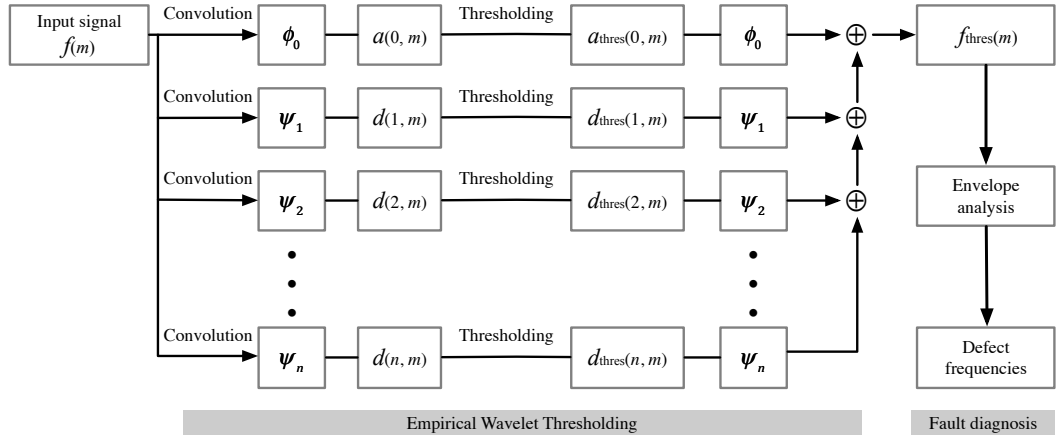


Fig. 5.2. Flowchart of the empirical wavelet thresholding and fault diagnosis method.

$$u(m) = \begin{cases} 1, & m = 0, \frac{M}{2} \\ 2, & m = 1, 2, \dots, \frac{M}{2} - 1 \\ 0, & m = \frac{M}{2} + 1, \dots, M - 1 \end{cases} \quad (5.11)$$

The Discrete Hilbert envelope, denoted $e_D(n)$, can be expressed as follows:

$$e_D(n) = \sqrt{f_{\text{thres}}^2(n) + \{\mathcal{H}[f_{\text{thres}}(n)]\}^2} \quad (5.12)$$

Finally, the frequency spectrum of the Discrete Hilbert envelope $E_D(f) = \mathcal{F}(e_D(n))$ is analysed in order to find bearing defect frequencies. Fig. 5.2 shows a flowchart of the proposed method.

5.3 Case 1: manual rotation and spectrum segmentation

In order to simulate operations of blade bearings and diagnose blade bearing fault types, we designed two rotation methods. The first one is the manual rotation and the other is the motor driving. From Fig. 5.3, the bearing can be manually rotated by two experimenters. They can use a metal bar as a lever and the bearing can be pushed down in either clockwise direction or pulled up in the anticlockwise direction. The purpose of the manual rotation is to detailedly investigate naturally damaged blade bearing fault characteristics at a very low external noise level without noise caused by

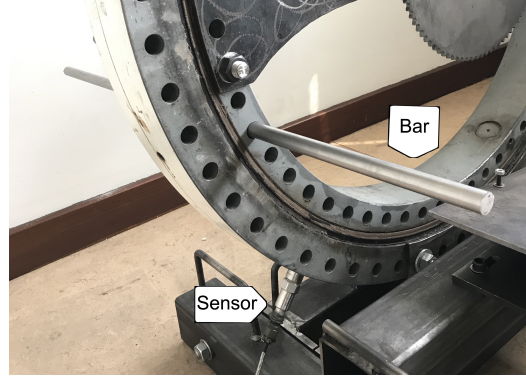


Fig. 5.3. Wind turbine blade bearing test rig.

driving systems. A natural question for the manual rotation is whether rotation speeds are constant. Therefore, we use a video camera to record manual rotations and then analysis bearing rotation speeds. It is found that speeds are fairly constant except the starting and ending periods which are very similar to real-world conditions. As can be seen in Fig. 5.4, only the middle part is used for further analysis and starting and ending parts are eliminated.

5.3.1 Raw vibration data at different manual rotation speed conditions

First of all, the bearing inner ring is manually rotated in the clockwise direction at rotation speeds of 1.2 r/min, 2.1 r/min and 4.1 r/min respectively and the quasi-constant speed rotation angle is 45° . Fig. 5.5(a) displays the raw vibration signals with a sampling rate of 50 kS/s. As can be seen, there are a number of small spikes and several large spikes in each test. These spikes may indicate fault signals. As the bearing is naturally damaged, the extents of the faults inside the bearing are noticeably different. The amplitudes of weak fault signals are smaller than 0.1 volts, but the amplitudes of severe fault signals are greater than 0.25 volts. However, because of the noise generated from the bearing itself, more representative or useful information cannot be observed in the raw data. Therefore, the frequency spectrums of these three tests are presented in Fig. 5.5(b) using the fast Fourier transform (FFT) method. It can be seen in Fig. 5.5(b), these three tests have similar frequency distributions and dominant frequency components are concentrated in the frequency range from 0 to

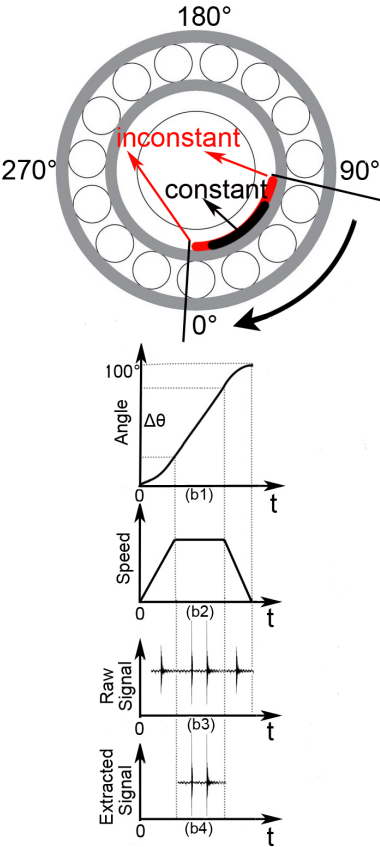


Fig. 5.4. The schematic of manual rotation operation.

Table 5.1

Defect frequencies of the test blade bearing.

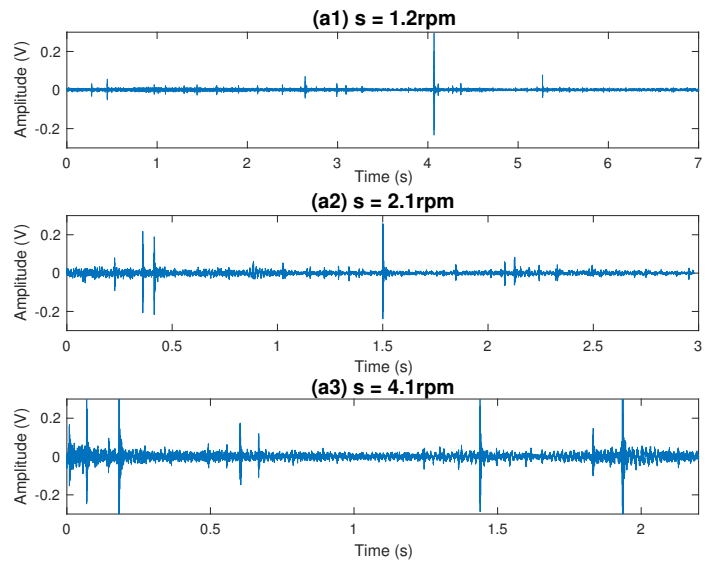
Rotation speeds (r/min)	f_I (Hz)	f_O (Hz)	f_B (Hz)	Comments
1	0.5173	0.4826	0.1541	Fundamental defect frequency
1.2	0.6208	0.5791	0.1850	Manual rotation
2.1	1.0863	1.0135	0.3236	
4.1	2.1209	1.9787	0.6318	
3.19	1.6502	1.5395	0.4916	Motor driving
3.05	1.5778	1.4719	0.4700	

3600 Hz. From Figs. 5.6(a) and 5.6(b), due to the noise, the defect frequencies listed in Table 5.1 cannot be observed in the frequency spectrum of raw data. Therefore, we need to remove these noise with the aim of extracting fault features in the following subsections.

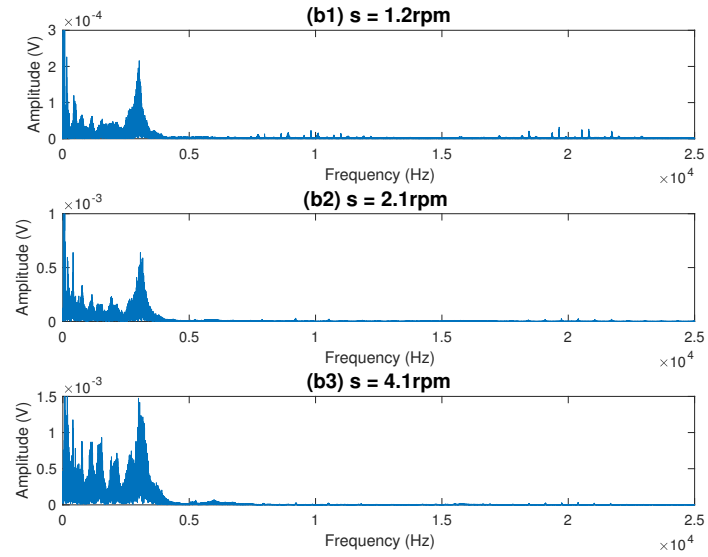
5.3.2 Spectrum segmentation

For the empirical wavelet transform, segmentation of the Fourier spectrum is a vital procedure as it provides the adaptability with respect to the raw vibration data. Some segmentation methods, such as local maxima, scale space, etc., can estimate different modes when the signal is composed as sinusoidal waveforms with short length [203]. However, for complex signals generated by the naturally damaged wind turbine bearings with long sampling time and high sampling rate conditions, the number of segments N is very difficult to determine. If N is very small, the extracted modes will be covered a great deal of noise. If the number of N is very big, the calculation will be very slow. For this reason, we propose to use a novel experimental-based spectrum segmentation approach to quickly determine the boundaries.

Fig. 5.7(a) displays the frequency spectrums of three manual rotation vibration signals from 0 to 4000 Hz where nine spike groups can be seen clearly for each test. As a result, in the frequency domain, different rotation speeds change the spectrum amplitudes. However, no significant changes are reflected on frequency components. This situation is due to the fact that the variations of different speeds are very small. Therefore, for different slow rotation speed tests, the same boundaries can be used to remove noise and extract fault features.

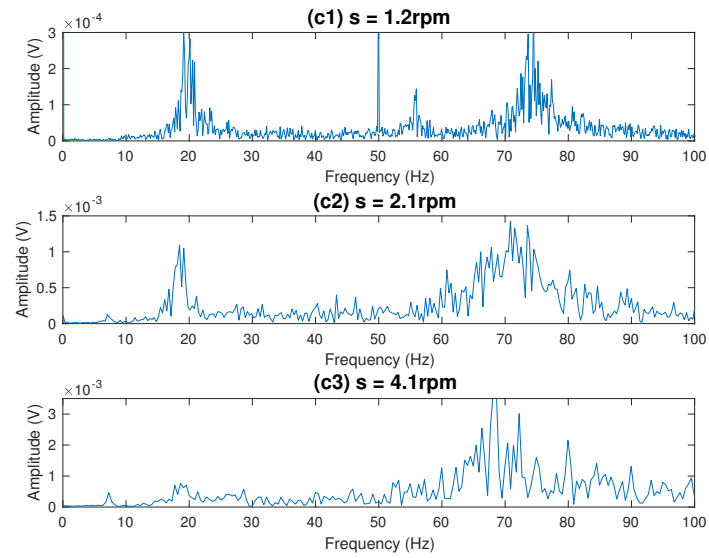


(a)

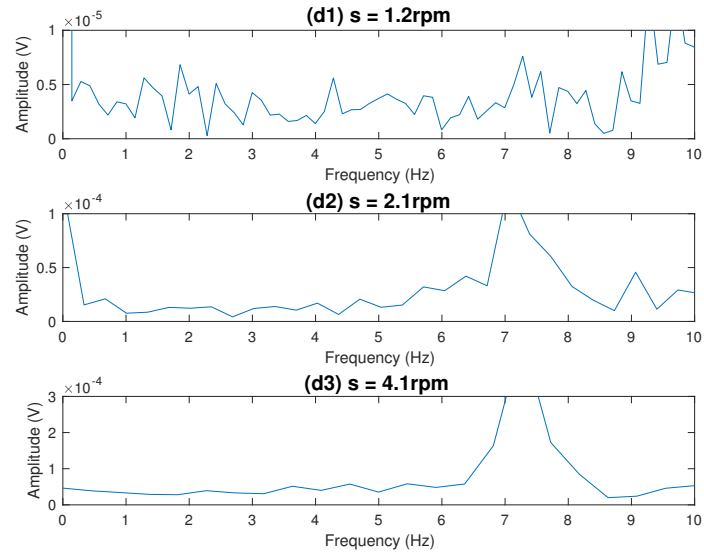


(b)

Fig. 5.5. (a) The raw vibration data plots, (b) the frequency spectrum plots.

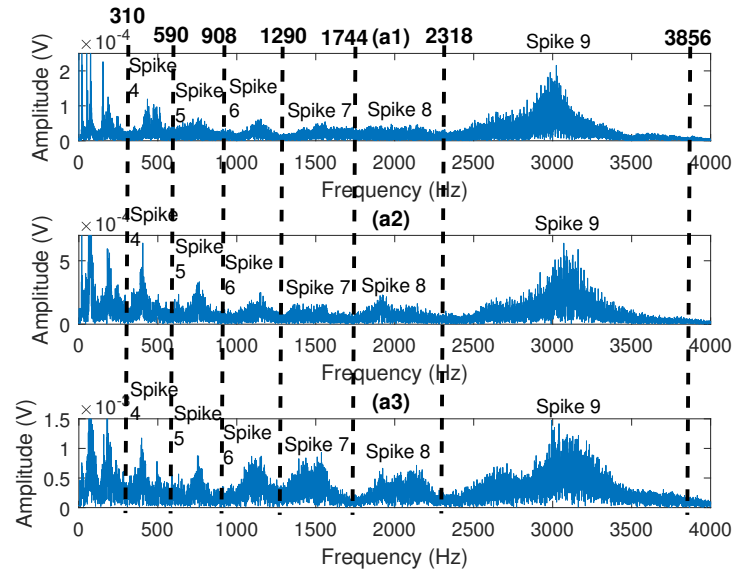


(a)

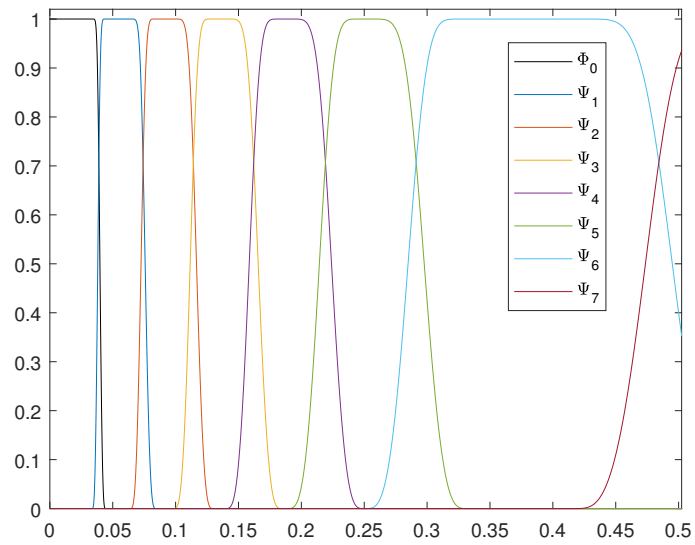


(b)

Fig. 5.6. (a) 0-100 Hz frequency spectrum plots and (b) 0-10 Hz frequency spectrum plots.



(a)



(b)

Fig. 5.7. Segmentations of frequency spectrums at (a1) 1.2 r/min (a2) 2.1 r/min (a3) 4.1 r/min and (b) empirical wavelet filter bank in the normalized Fourier axis.

Based on the spike group distributions shown in Fig. 5.7(a), the boundaries make a trial of $B_1 = 310$ Hz, $B_2 = 590$ Hz, $B_3 = 908$ Hz, $B_4 = 1290$ Hz, $B_5 = 1744$ Hz, $B_6 = 2318$ Hz and $B_7 = 3856$ Hz. As can be seen in Fig. 5.7(b), these seven boundaries have separate the whole frequency band into eight portions. Φ_0 is the scaling function and $\Psi_n(n=1\dots7)$ indicates empirical wavelets.

5.3.3 Empirical wavelet thresholding

Fig. 5.8(c) displays the spectrum of each decomposition respectively with the 4.1 r/min rotation speed. In order to quantify the fault signals in each mode, kurtosis is used in this chapter which is defined as the fourth standardized moment [204].

$$\text{Kurt} = \frac{E(x - \mu)^4}{\sigma^4} = \frac{\frac{1}{n} \sum_{i=1}^n (x_i - \mu)^4}{\left(\frac{1}{n} \sum_{i=1}^n (x_i - \mu)^2 \right)^2} \quad (5.13)$$

where μ is the mean value of x and σ is the standard deviation of x . From (5.13), this global kurtosis can reflect an overall probability distribution of the whole signal in the time domain. The high kurtosis value may be caused by a high amount of spikes. As can be seen in Fig. 5.8(c), kurtosis values are very small for Mode 1 and Mode 2; therefore, there are very few fault energies distributed below 590 Hz. From Mode 3 to Mode 8, many large fault signals and weak fault signals are reflected, especially for Mode 5, Mode 6, Mode 7 and Mode 8. For the empirical wavelet transform, the extracted modes can be denoised via the hard-thresholding, and defect signals in each mode can be reconstructed for the further fault diagnosis.

In Fig. 5.8(c), red dash lines in each mode indicate the universal threshold value calculated by Eqs. (5.7) and (5.8). For each mode, all wavelet coefficients within the upper threshold and lower threshold will be set to zero. Fig. 5.8(a) and Fig. 5.8(b) compare the raw vibration signal and the empirical wavelet thresholding signal. The kurtosis of the raw vibration data is only 246.8, but it increase to 545.0 after applying the empirical wavelet thresholding technique. In Fig. 5.8(b), some small spikes and large spikes are clearly presented with extremely low noise disturbances. Compared

with the conventional band-pass filtering method, such as kurtogram, the empirical wavelet thresholding can fully use defect signals distributed in the whole frequency band. As a result, the empirical wavelet thresholding method can successfully reduce the noise of blade bearing vibration signals to minimum, which presents the superiority of the proposed method higher than traditional decomposition or band-pass filtering methods.

5.4 Case 2: vibration signals collected by motor driving

For the motor driving rotation, as shown in Fig. 4.3, the motor is able to generate constant rotation speeds in the test conducted. As can be seen in the schematic shown in Fig. 5.9, to simulate real-world conditions, only part of the data is extracted per revolution. The same constant speed short parts collected from each revolution can be recombined to increase the data length (Fig. 5.9(c4) and (c5)).

Fig. 5.10(a) shows the raw data in the time domain at 3.19 r/min and Fig. 5.10(b) illustrated the recombined signal with three 90° portions vibration data. Each part is extracted from each revolution and they have similar vibration characteristics. In the same way, Fig. 5.11(a2) displays the recombined signal at the rotation speeds of 3.12 r/min. Consequently, the FFT is applied to the recombined data to present the signal in the frequency domain. Fig. 5.11(b) displays the frequency spectrums of the recombined data. Comparing with Fig. 5.7(a) and Fig. 5.11(b), the frequency distributions below 2318 Hz for two situations are very similar which have 8 spike groups. Above 2318 Hz, the amplitudes in Fig. 5.11(b) become small due to external mechanical and electrical noise. Therefore, the boundaries for the recombined signals can be the same as Section 5.3.2 which are $B_1 = 310$ Hz, $B_2 = 590$ Hz, $B_3 = 908$ Hz, $B_4 = 1290$ Hz, $B_5 = 1744$ Hz, $B_6 = 2318$ Hz and $B_7 = 3856$ Hz.

Fig. 5.12(c) shows the extracted modes at 3.19 r/min. For Mode 8, the noise type is different from other modes which is asymmetry to x-axis. Therefore, the calculated

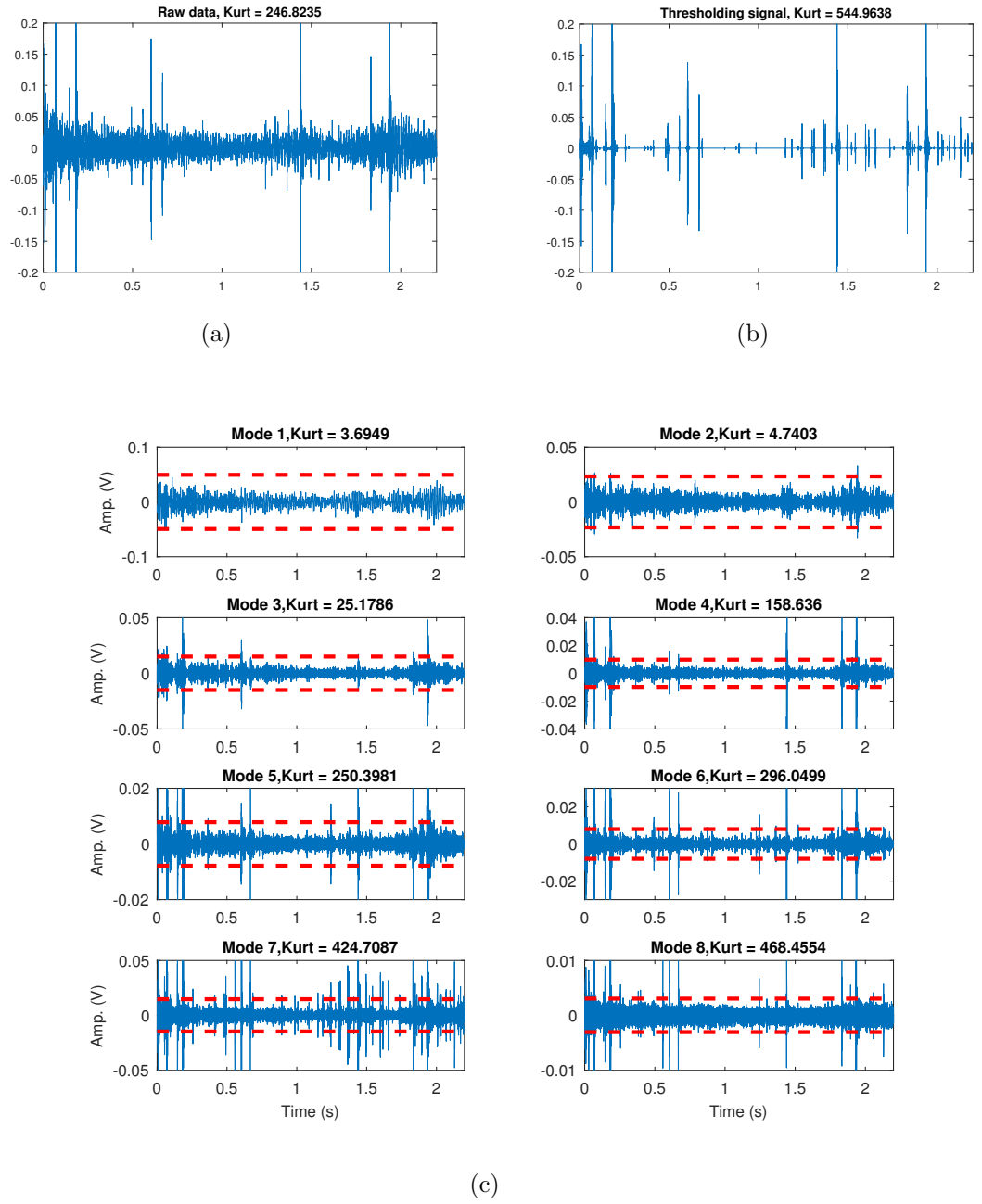


Fig. 5.8. (a) raw vibration signal at 4.1 r/min and (b) empirical wavelet thresholding signal and (c) modes extracted by the empirical wavelet transform.

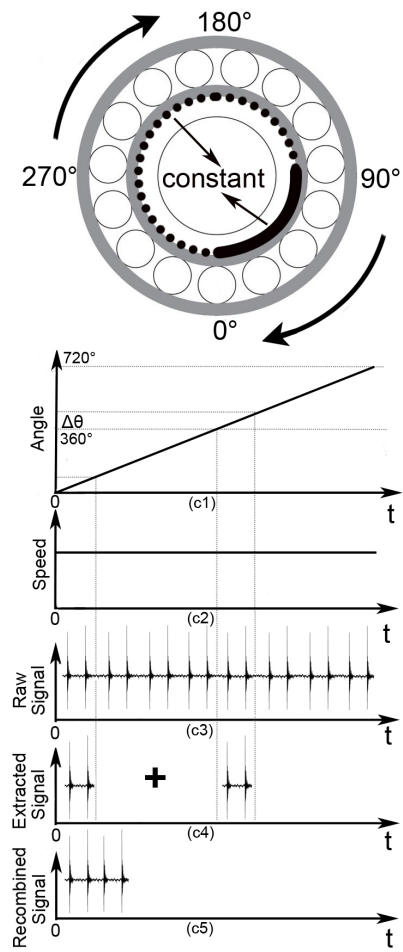


Fig. 5.9. The schematic of motor driving.

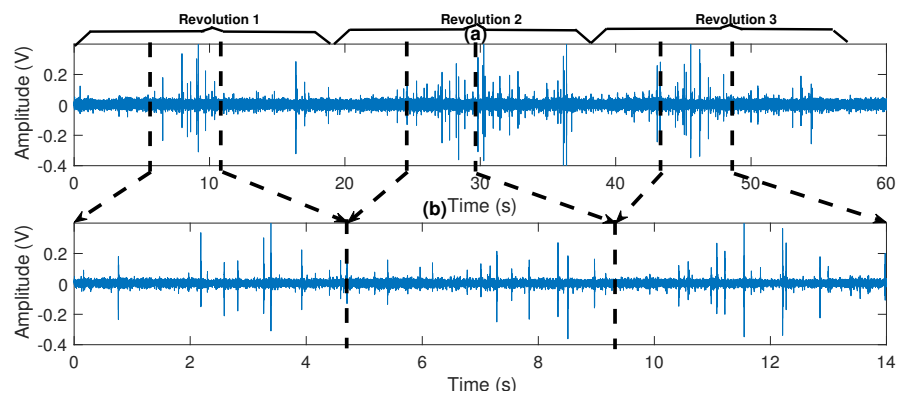


Fig. 5.10. raw and recombined vibration data at 3.19 r/min.

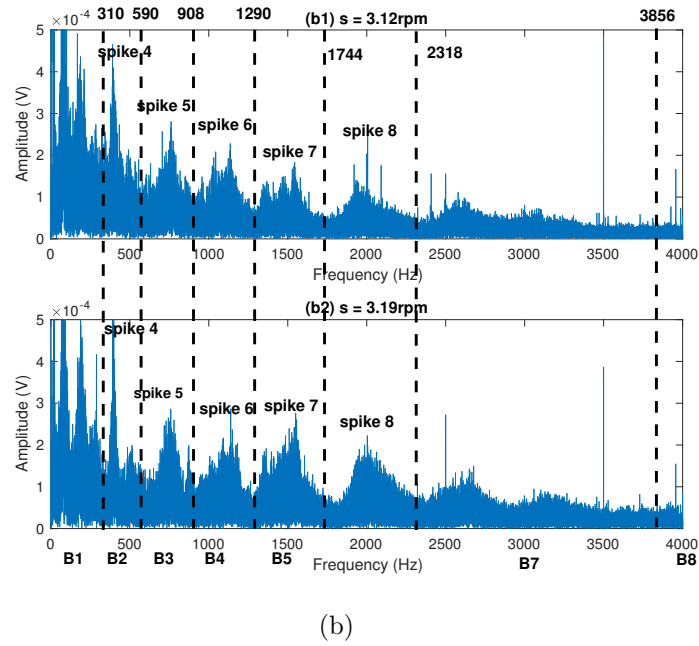
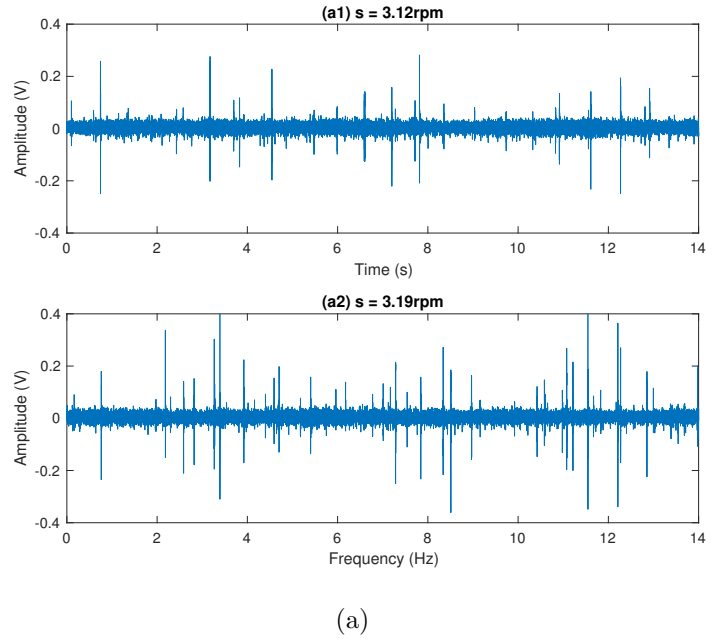


Fig. 5.11. The recombined vibration data plots at (a1) 3.19 r/min (a2) 3.12 r/min and the frequency spectrum plots at (b1) 3.19 r/min (b2) 3.12 r/min.

Table 5.2

Diagnosis accuracy at 3.19 r/min and 3.12 r/min.

Rotation speed	Defect frequency matching accuracy		
	Inner race fault	Outer race fault	Ball fault
3.19 r/min	98.90%	92.97%	63.54%
3.12 r/min	98.43%	95.79%	67.13%
Average	98.67%	94.38%	65.34%

thresholding value (red dash line) for Mode 8 is manually modified to 0.07 V (blade dash line) in order to minimize the noise influence. Fig. 5.12(a) and Fig. 5.12(b) indicate the raw vibration data and the empirical wavelet thresholding signal. Similarly, Fig. 5.13 presents both the time domain signal and the empirical wavelet thresholding signal at 3.12 r/min. It is clearly seen the proposed method can extract fault signals under slow rotation speed conditions.

After that, the Hilbert envelope method is applied to find defect frequencies of denoised signals. As can be seen in Fig. 5.14, the dominant frequencies are 1.630 Hz at 3.19 r/min and 1.553 Hz at 3.12 r/min.

The equation below is used to evaluate the defect frequency matching accuracy which is the ratio between the identified dominant frequency and the theoretical defect frequency:

$$\text{Accuracy} = (1 - |f_{\text{rotation}} - f_{\text{fault}}| / f_{\text{fault}}) \times 100\% \quad (5.14)$$

where f_{rotation} indicates the dominant frequencies for each test and f_{fault} can be chosen as f_i , f_o and f_b shown in Table 5.1. Table 5.2 lists the matching accuracy. It is found that the bearing most likely has on inner fault with an average diagnosis accuracy 98.67%.

5.5 Conclusion

In this chapter, the vibration signals of a large-scale wind turbine blade bearing are collected by two cases which are the manual rotation and motor driving. For the manual rotation case, it can simulate the real-world blade bearing working condition

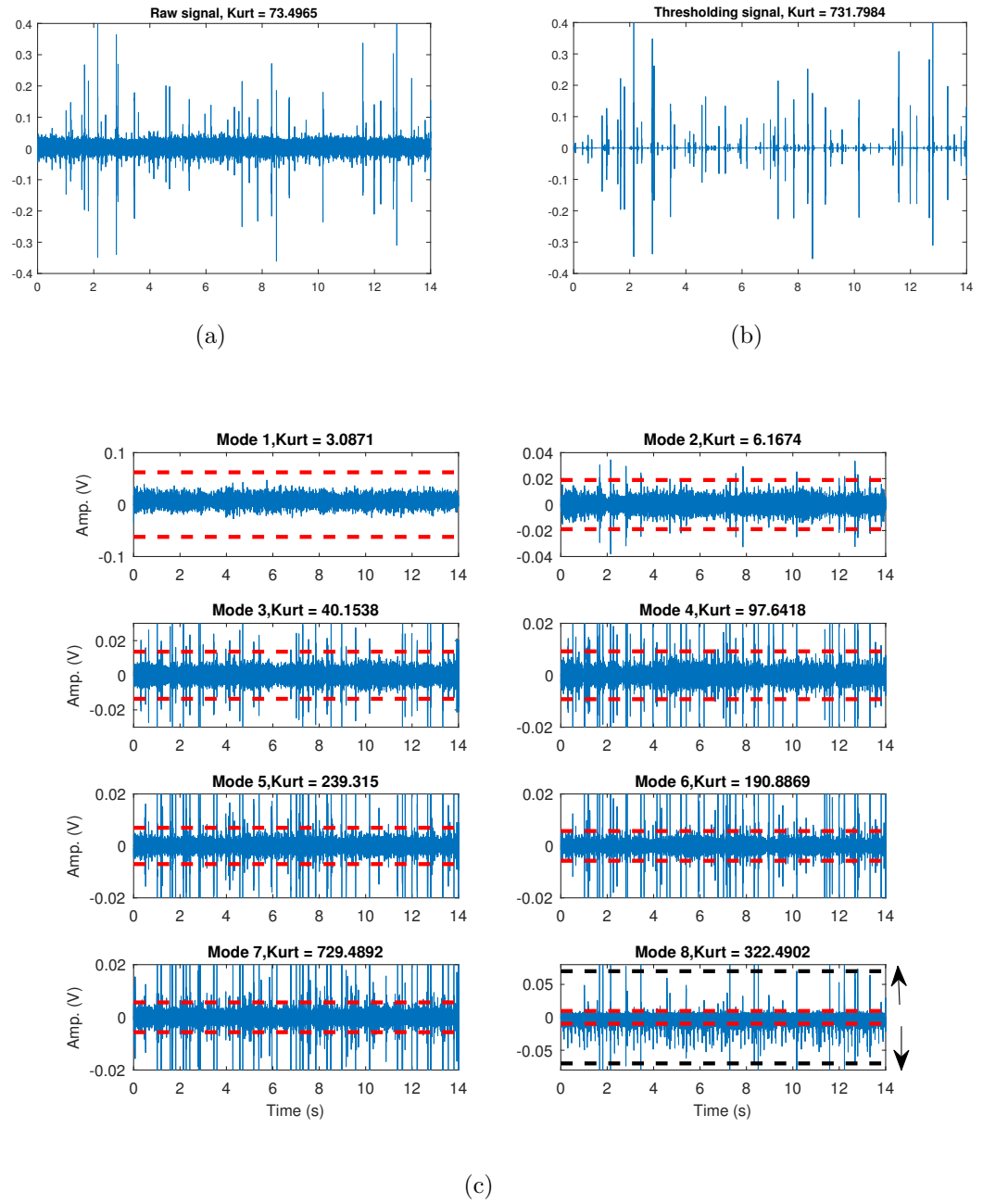
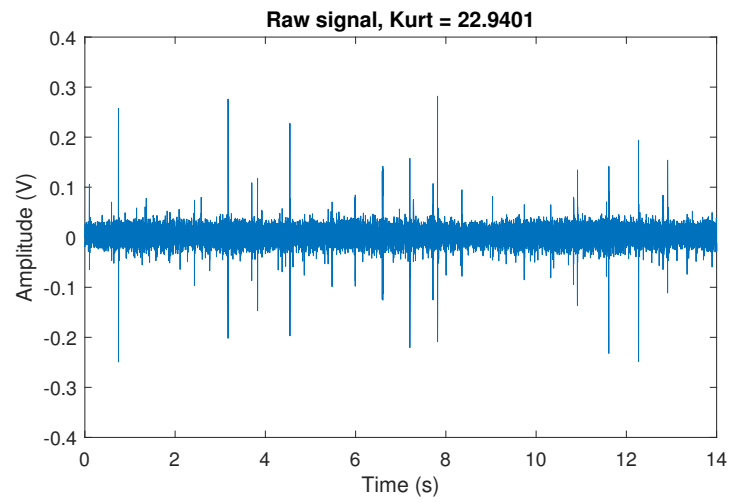
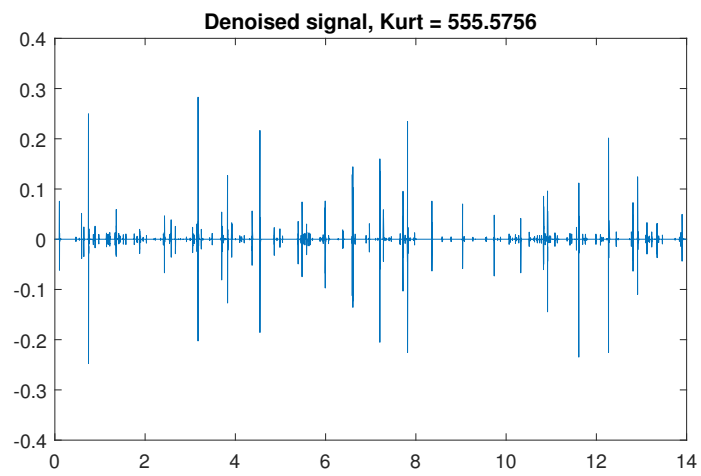


Fig. 5.12. (a) raw vibration signal at 3.19 r/min and (b) empirical wavelet thresholding signal and (c) modes extracted by the empirical wavelet transform.

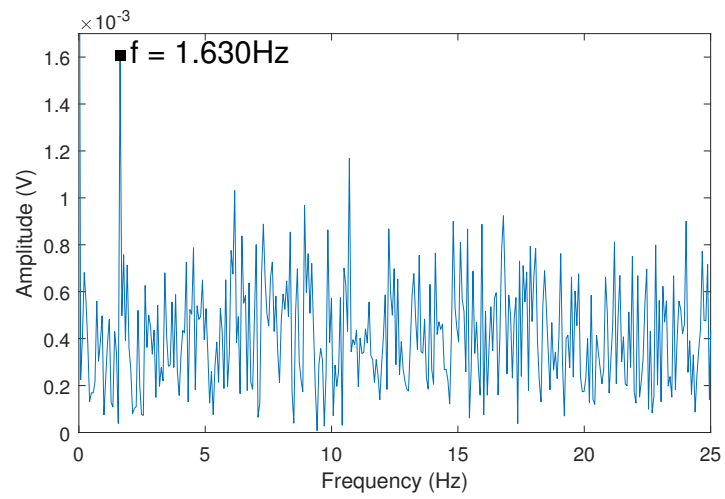


(a)

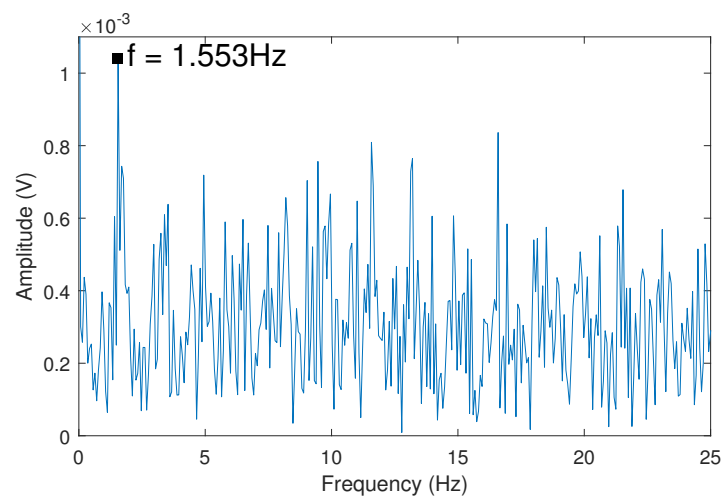


(b)

Fig. 5.13. (a) raw vibration signal at 3.12 r/min and (b) empirical wavelet thresholding signal.



(a)



(b)

Fig. 5.14. Defect frequencies at (a) 3.19 r/min, (b) 3.12 r/min.

at a very low external noise level. Therefore, this case can easily study severe fault and weak fault characteristics so that the frequency boundaries of fault signals can be determined. For the motor driving condition, the limited vibration signals are recombined in order to improve the diagnostic accuracy. This procedure can effectively solve the lack of data issue at constantly rotating speeds for field tests of wind turbine blade bearing CMFD. The empirical wavelet thresholding method is applied to denoise the recombined signals and the envelope analysis is implemented to diagnose the bearing fault.

Chapter 6

Vibration Fault Diagnosis Using Iterative Nonlinear Filter and Morphological Analysis

6.1 introduction

As introduced in Section.1.2, wind turbine blade bearings work at slow rotation speeds with limited angles, so it is necessary to design effective methods to maximally extract and utilize the limited weak fault signals. This generally involves the techniques of signal denoising and fault characteristics analysis.

For signal denoising, the purpose is to reduce the noise components of the raw vibration signal so that the weak fault signals are extracted. As the bearing fault signals and noise components are often two uncorrelated parts [205], signal denoising can be achieved via two approaches, namely fault signal extraction and noise component elimination. With regard to the first approach, some band-pass filtering methods such as fast kurtogram [206], can directly extract fault signals in a narrow frequency band. However, some useful frequency components beyond this frequency band are also abandoned. As a result, under slow-speed conditions, some weak fault signals may be degraded or diffused, which may affect the accuracy of the diagnostic results.

The other denoising manner is noise component elimination. The noise components generated from blade bearing rotation movements have a periodic property in the time domain. The noise cancellation method such as discrete/random separation (DRS), is to eliminate the periodic noise from raw vibration data. Then, the weak fault signals are extracted when the noise is cancelled [207, 208]. Nonetheless, in practice, the drawbacks of the noise cancellation method are that the noise components may not be completely removed and some signals (often in high frequency) may leak. Therefore, signal denoising may be unsatisfactory in some cases.

In regard to fault characteristics analysis, the envelope method is often implemented to detect the presence of defect frequencies relating to rolling elements that pass over the defect point [209]. The Hilbert transform-based envelope method (Hilbert envelope method) has been widely used in bearing fault diagnosis [210]. However, for blade bearing fault detection, the Hilbert envelope is very sensitive to noise which can submerge weak fault signals, meaning that defect frequencies are unnoticeable in the frequency domain.

As a result, the conventional methods mentioned above may not be the ideal solutions for blade bearing fault detection because the noise level cannot be maximally suppressed. In order to minimize noise to an insignificant level and fully utilize weak fault signals, this chapter proposes a novel iterative nonlinear filter (INF) for signal denoising. The new INF method combines a fault signal extraction method, a nonlinear diffusion filter, and a noise cancellation method, DRS. In other words, the INF is a linear combination of a nonlinear diffusion filter and a noise cancellation filter with the aim of maximally exploiting their benefits and overcoming their weakness. This can be explained more specifically as follows:

- The nonlinear diffusion filter was firstly used on image denoising and edge detection by Perona and Milik [211] and further utilized by Li et al. [212] as an edge-preserving denoising method for 1-D signals. However, this chapter is the first attempt to apply nonlinear diffusion filter to bearing vibration signal denoising. The advantage of the nonlinear diffusion filter is that it can smooth the signal waveform in the time domain and directly extract weak fault signals

by capturing impulse-like or sharp edge type fault signals with minimal useful information loss. This could effectively increase the defect signal-to-noise ratio.

- The nonlinear diffusion filter may not effectively reduce periodic noise. To overcome this drawback, one possible solution is to utilize the advantage of the noise cancellation method DRS to reduce periodic noise.
- The new INF iteratively and gradually filters the vibration signal by extracting the fault signals and cancelling out the periodic noise. The process continues until the filtering performance criterion is maximized. In this chapter, a kurtosis value is chosen as the criterion because a high kurtosis value can indicate that the signal has a great deal of impulsive-type fault signals.

After that, in order to diagnose the bearing fault type in the frequency domain, the morphological transform-based envelope method (morphological envelope method) is employed for fault characteristic analysis. The morphological transform is a nonlinear analysis method which was first utilized to denoise images [213]. Then, Nikolaou et al. [214] developed the morphological transform for bearing vibration signal envelope analysis. Unlike the conventional Hilbert envelope method, the morphological envelope method can further denoise the residual noise leaked from the INF filter and enhance the weak fault signals, so the bearing defect frequencies can be identified distinctly. Extensive experimental results demonstrate that the proposed INF and morphological envelope methods outperform conventional filtering methods or the Hilbert envelope method when diagnosing the naturally damaged slow speed blade bearing fault type [79].

6.2 Background theory

6.2.1 Iterative Nonlinear Filter (INF)

The new denoising method INF is a linear combination of a nonlinear diffusion process and a noise cancellation process, which can iteratively and gradually smooth the signal

waveform and remove periodic noise. On the one hand, if only the nonlinear diffusion process is applied, the signal waveform, which is influenced by the high frequency signal, can be smoothed but the periodic noise cannot be removed; on the other hand, if only the noise cancellation method DRS is adopted, the periodic noise can be eliminated but the high frequency signals may leak. As a result, the combination of the nonlinear diffusion process and DRS can fully exploit their benefits and overcome their weaknesses.

Nonlinear diffusion process

The main idea of INF is the nonlinear diffusion filter which is a multi-scale smoothing and impulse signal detection scheme [215]. In other words, the nonlinear diffusion filter can reduce noise and extract impulsive-type fault signals with minimal useful information loss. The nonlinear diffusion filter is summarized as follows:

Let $X(n)$ be a raw vibration signal of length N . The equation for the nonlinear diffusion process based on the Perona-Malik model is expressed below [211]:

$$\frac{\partial}{\partial t}X(n, t) = \frac{\partial}{\partial n} \left[c(n, t) \cdot \frac{\partial}{\partial n} X(n, t) \right] \quad (6.1)$$

with an initial condition $X(n, 0) = X(n)$, $n = 1, \dots, N$. $c(n, t)$ indicates the diffusion function which controls the diffusion strength and denoising strength, and $X(n, t)$ is the current signal intensity. The variable t is the process ordering parameter.

The diffusion function $c(n, t)$ varies with the magnitude of the gradient of the signal intensity $X(n, t)$, which is a monotonically decreasing function $c(n, t) = f(\frac{\partial}{\partial n}X(n, t))$. In general, $c(0, t) = 1$ and $c(n, t) > 0$ for n tending to infinity. The diffusion function is expressed below:

$$c(n, t) = \exp \left(- \left(\left| \frac{\partial}{\partial n} X(n, t) \right| / \kappa \right)^2 \right) \quad (6.2)$$

where the parameter κ is the noise threshold. If $\frac{\partial}{\partial n}X(n, t)$ is large, $c(n, t)$ becomes small which indicates the diffusion is weak and the spikes can be prevented. On the contrary, if $\frac{\partial}{\partial n}X(n, t)$ is small, $c(n, t)$ is large; therefore, the diffusion is strong which can smooth the signal waveform.

In order to find the solution for the nonlinear diffusion equation, the discrete approximation is considered. For one iteration step of (6.1), the expression of $\frac{\partial}{\partial t}X(n, t)$ and $\frac{\partial}{\partial n}X(n, t)$ are approximated as [212]

$$\frac{\partial}{\partial t}X(n, t) \approx \frac{X(n, t + \Delta t) - X(n, t)}{\Delta t} \quad (6.3)$$

and

$$\frac{\partial}{\partial n}X(n, t) \approx \frac{X(n + \Delta n/2, t) - X(n - \Delta n/2, t)}{\Delta n} \quad (6.4)$$

respectively.

Moreover, the discrete approximation of $\frac{\partial}{\partial n} [c(n, t) \cdot \frac{\partial}{\partial n}X(n, t)]$ is [215]

$$\begin{aligned} & \frac{\partial}{\partial n} \left[c(n, t) \cdot \frac{\partial}{\partial n}X(n, t) \right] \\ & \approx \frac{\partial}{\partial n} \left[c(n, t) \cdot \frac{1}{\Delta n} \left(X\left(n + \frac{\Delta n}{2}, t\right) - X\left(n - \frac{\Delta n}{2}, t\right) \right) \right] \\ & \approx \frac{1}{\Delta n^2} \left[c\left(n + \frac{\Delta n}{2}, t\right) \cdot (X(n + \Delta n, t) - X(n, t)) \right. \\ & \quad \left. - c\left(n - \frac{\Delta n}{2}, t\right) \cdot (X(n, t) - X(n - \Delta n, t)) \right] = \Phi_r - \Phi_l \end{aligned} \quad (6.5)$$

where $\Phi_r = \frac{1}{\Delta n^2} \cdot c(n + \frac{\Delta n}{2}, t) \cdot (X(n + \Delta n, t) - X(n, t))$ and $\Phi_l = \frac{1}{\Delta n^2} \cdot c(n - \frac{\Delta n}{2}, t) \cdot (X(n, t) - X(n - \Delta n, t))$

Substituting (6.3) and (6.5) into (6.1), yields

$$X(n, t + \Delta t) - X(n, t) = (\Phi_r - \Phi_l) \cdot \Delta t \quad (6.6)$$

For convenience, denoting $X^{k+1}(n)$ and $X^k(n)$ to $X(n, t + \Delta t)$ and $X(n, t)$ respectively, therefore, the next iteration can be expressed as:

$$X^{k+1}(n) = X^k(n) + \Delta t \cdot (\Phi_r - \Phi_l) \quad (6.7)$$

where $X^k(n)$ indicates the nonlinear diffusion filtered signal at the k th iteration.

For example, Fig.6.1(a) shows an enlarged raw vibration signal within 0.1 seconds. After the first iteration shown in Fig.6.1(b), the edge of the signal waveform has been smoothed and the potential fault signal is preserved; therefore, the contrast between weak fault signals and the signal waveform is increased so that the defect signal to noise ratio is increased.

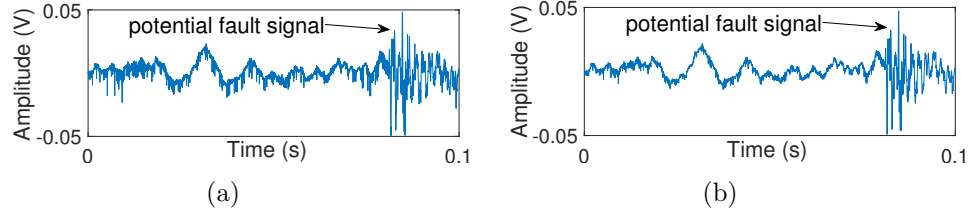


Fig. 6.1. (a) Enlarged raw vibration signal within 0.1s (b) Nonlinear diffusion filtered signal after the first iteration.

Noise cancellation process

After the signal waveform is smoothed via the nonlinear diffusion filter, the next step of INF is to eliminate periodic noise via the noise cancellation process. As mentioned in Introduction, fault signals and noise components are often two uncorrelated parts, so the expression of the nonlinear diffusion filtered signal $X^k(n)$ at the k th iteration can be expressed as $X^k(n) = p^k(n) + r^k(n), n = 1, \dots, N$ where $p^k(n)$ represents a periodic process including noise components and $r^k(n)$ represents a stochastic process containing bearing faults [207]. $r^k(n)$ and $p^k(n)$ are independent with each other. Based on the prediction theory, the periodic process can be predicted using past values, while the stochastic part cannot be predicted from its previous values which is estimated from the prediction error [207].

More specifically, from Ref. [207], define $\hat{X}^k(n)$ as the predictor of $X^k(n)$ from a finite number of past values $X^k(n - \Lambda - i)$ where $i = 0, \dots, M - 1$ with Λ satisfies the autocorrelation equation $\mathbb{E}[r^k(n)r^k(n - \lambda)] = 0$ for all $|\lambda| > \Lambda$. The notation $\mathbb{E}[\cdot]$ is the expectation operator. The expression of $\hat{X}^k(n)$ is given by a linear regressor of the form

$$\hat{X}^k(n) = \sum_{i=0}^{M-1} h_i^k X^k(n - \Lambda - i) \quad (6.8)$$

Therefore, from the above discussion, the estimator of the periodic process is $\hat{p}^k(n) = \hat{X}^k(n)$; and the prediction error which is the estimator of the stochastic process is expressed as $\hat{r}^k(n) = \hat{X}^k(n) - X^k(n)$. In order to find the best $\hat{X}^k(n)$ that can minimize the prediction error $\hat{r}^k(n)$, the following mean squared error σ_e^2 is used,

$$\sigma_e^2 = \frac{1}{N} \sum_{n=1}^N \left[\hat{X}^k(n) - X^k(n) \right]^2 \quad (6.9)$$

To find out the minimum σ_e^2 , we can compute the gradient of (6.9):

$$\sum_{i=1}^{M-1} \frac{\partial(\sigma_e^2)}{\partial h_i^k} = \frac{2}{N} \sum_{n=1}^N \left[\sum_{i=0}^{M-1} h_i^k r^k(n, i) - r^k(n) \right] \quad (6.10)$$

where $r^k(n, i) = \sum_{j=0}^{M-1} X^k(n - \Lambda - j) X^k(n - \Lambda - i)$ and $r^k(n) = \sum_{j=0}^{M-1} X^k(n - \Lambda - j) X^k(n)$.

Then, at the minimum, the condition that should hold is $\sum_{i=0}^{M-1} h_i^k r^k(n, i) - r^k(n) = 0$.

Finally, the optimal set of weights h_i^k , $i = 0, \dots, M - 1$ verifies the Wiener-Hopf equations

$$r^k(n) = \sum_{i=0}^{M-1} h_i^k r^k(n, i), n = 1, \dots, N \quad (6.11)$$

Antoni et al. [208] proposed a faster approach DRS to process (6.11) in the frequency domain.

$$\begin{aligned} \mathcal{F}[r^k(n)] &= R_1^k(f) = \mathcal{F} \left[\sum_{i=0}^{M-1} h_i^k r^k(n, i) \right] \\ &= \sum_{n=1}^N r^k(n, i) e^{-j\omega(n-i)} \sum_{i=0}^{M-1} h_i^k e^{-j\omega i} = R_2^k(f) H^k(f) \end{aligned} \quad (6.12)$$

where $\mathcal{F}[\cdot]$ corresponds to the Discrete Fourier Transform (DFT). As can be seen in (6.12), the Wiener-Hopf equation is simplified into the product and the filter $H^k(f)$ can be solved via a current signal block $R_1^k(f)$ and a past signal block $R_2^k(f)$. Assuming $R_1^k(f) = \mathcal{F}[X^k(n - \xi)]$ and $R_2^k(f) = \mathcal{F}[X^k(n - \Delta - \xi)]$ where $\xi = 0, \dots, \Xi - 1$ and $\Delta > 0$. Labelling $\hat{R}_\Phi^k(f)$ and $\hat{R}_\Phi^{k,\Delta}(f)$ are the estimators of $R_1^k(f)$ and $R_2^k(f)$ respectively, which are the Φ -long ($\Phi = 2\Xi$ due to possible zero-padding) DFT of the two blocks at frequency f , the estimator of $H^k(f)$ is given by [208]

$$\hat{H}^k(f) = \hat{R}_\Phi^{k,\Delta}(f) \cdot \hat{R}_\Phi^k(f)^* / \left| \hat{R}_\Phi^{k,\Delta}(f) \right|^2 \quad (6.13)$$

The estimator $\hat{H}^k(f)$ is a Φ -long noise cancellation filter which can be used directly on the k th iteration signal denoising. Finally, the INF filtered signal $X_D^k(n)$ at k th iteration can be expressed as:

$$X_D^k(n) = X^k(n) * \hat{h}^k(\phi), \phi = 1, \dots, \Phi \quad (6.14)$$

where $\hat{h}^k(\phi) = \mathcal{F}^{-1}(\hat{H}^k(f))$ and $\mathcal{F}^{-1}[\cdot]$ corresponds to the inverse DFT, and $*$ indicates the convolution.

If the noise reduction of $X_D^k(n)$ is unsatisfactory, it can be substituted into (6.7) for the next iteration of denoising. Fig.6.2 shows a real example to illustrate the INF denoising procedure. In Fig.6.2(b), there is remarkable noise after the first INF iteration and the kurtosis is only 69.28. After nine iterations shown in Fig.6.2(c), the noise level has been reduced gradually with the kurtosis varying from 69.28 to 1076.61.

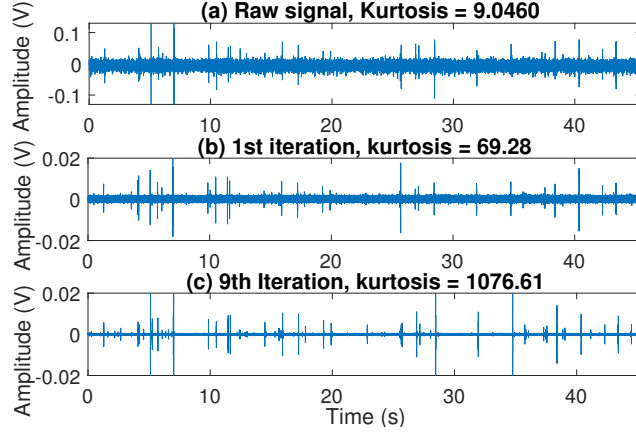


Fig. 6.2. (a) Raw vibration signal, and INF denoised signals after the (b) first INF iteration and (c) ninth INF iteration.

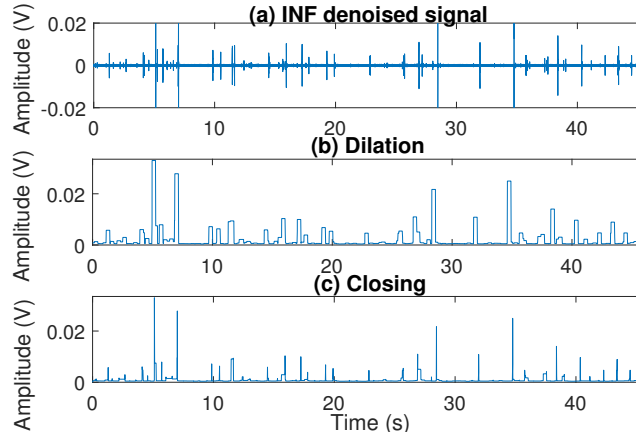


Fig. 6.3. (a) INF denoised signal, and different kinds of morphological envelopes: (b) dilation and (c) closing.

6.2.2 Morphological analysis

The vibration signals are characterised by the presence of impulsive-type fault signals modulated by high-frequency harmonic components [214]. However, for bearing fault characteristic analysis, the useful information is only the repetition rate of these impulsive-type fault signals (this is also referred to as the defect frequency), rather than detailed frequency contents of the full signal. To extract this repetition rate,

morphological analysis is employed in this chapter as it can extract impulsive-type fault signals and eliminate the impact of background noise. The implementation of morphological analysis is based on two basic set operations: Minkowski set addition (also termed dilation shown in (6.15)) and Minkowski set subtraction (also termed erosion shown in (6.16)) [214].

$$(X_D^k \oplus S)(n) = \max[X_D^k(n - \tau) + S(\tau)] \quad (6.15)$$

$$(X_D^k \ominus S)(n) = \min[X_D^k(n + \tau) - S(\tau)] \quad (6.16)$$

where \ominus indicates the operation of erosion and \oplus represents the operation of dilation. $X_D^k(n)$ is the INF denoised signal after k th iteration with $n = 1, \dots, N$; and the discrete function $S(\tau)$ is the structuring element (SE) over a domain $\tau = 1, \dots, T$ with $T < N$.

The combinations of the aforementioned two operations can demodulate two other signal envelopes: closing and opening. For example, to get the morphological closing envelope, the vibration signal is firstly added with the SE through the operation of Minkowski set addition and then subtracted with the SE through Minkowski set subtraction [214]. As for the operation of opening, the order of the set addition and set subtraction is reversed. The equations are as follows:

$$(X_D^k \bullet S)(n) = (X_D^k \oplus S \ominus S)(n) \quad (6.17)$$

$$(X_D^k \circ S)(n) = (X_D^k \ominus S \oplus S)(n) \quad (6.18)$$

where \circ and \bullet indicates the operation of opening and closing.

The equations from (6.15) to (6.18) can plot four types of envelopes, and here we will demonstrate dilation and closing as examples. The INF denoised signal (shown in Fig.6.3(a)) can be further processed via dilation and closing presented in Fig.6.3(b) and Fig.6.3(c). As can be seen, the morphological transform can further reduce the residual noise leaked from the INF processing. Comparing dilation and closing, it is observed that the closing of the signal presents a better visual inspection, whose shape is more close to the bearing fault signals. In respect of erosion and opening, they can only demonstrate negative impulses; for our research, we prefer to use the positive envelope. Therefore, in this chapter, we employ the closing of the signal as the morphological closing envelope which is used for fault characteristics analysis.

Finally, the frequency spectrum of the morphological closing envelope $\mathcal{F}[(X_D^k \bullet S)(n)]$ is calculated to identify the bearing defect frequencies.

6.2.3 Summary of the algorithm and parameter tuning

As can be seen in the flowchart (Fig.6.4), the procedure of the blade bearing fault detection is conducted in two stages: the INF denoising stage and the fault diagnosis stage. The INF denoising stage produces an iterated processing scheme to gradually denoise the raw vibration signal until noise reduction reaches a satisfactory level. The morphological analysis is then used to detect bearing defect frequencies.

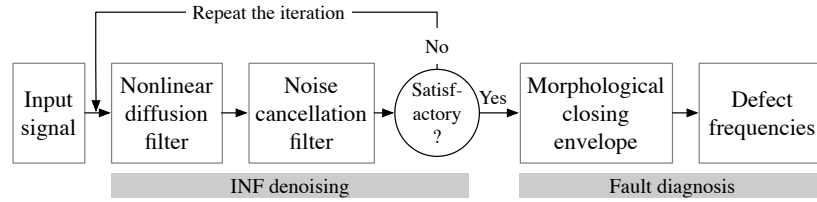


Fig. 6.4. The flowchart of the proposed method.

For the INF denoising stage shown in Fig.6.4, each iteration consists of two steps: smoothing via a nonlinear diffusion process and periodic noise elimination via a noise cancellation process. In respect of the nonlinear diffusion process, the integration constant Δt is the first parameter that has to be determined. For the 1-D case, Gerig et al. [215] derived the upper bound of Δt up to $\frac{1}{3}$; therefore, in this chapter, $\Delta t = \frac{1}{3}$ is used. The other important parameter is the noise threshold κ which controls the amount of diffusion applied in the gradient direction [216]. The selection of κ is based on trial-and-error. To obtain a better denoising performance, a test series with different κ must be generated and compared. Concerning the DRS noise cancellation process, the filter length Φ can influence the quality of the denoised signal and it should exceed a potential fault signal length. The second parameter of DRS is to choose a suitable time delay Δ . The optimal value of Δ can enable the constructed filter to minimize the mean squared error shown in (6.9). The value of Δ can be incrementally increased and the one with the least mean squared error is chosen. The last parameter for INF denoising is the number of iterations k . To evaluate the denoising performance for each iteration, the kurtosis is preferred as an indicator. The iteration continues until the

maximal kurtosis value is found. For example, as can be seen in Fig.6.5, the highest kurtosis is 1077 at Iteration 9. Therefore, we can repeat 9 times to denoise the raw vibration signal.

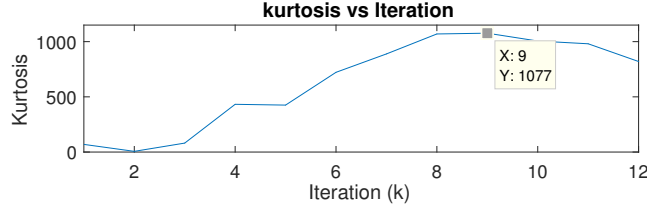


Fig. 6.5. Kurtosis versus iteration k .

With respect to the fault diagnosis stage in Fig.6.4, flat SEs (e.g., amplitude = 0) are utilized in this chapter. Therefore, the length of the SE is the only tunable factor for morphological analysis. Generally speaking, a shorter SE can extract more signal impulses enhancing higher frequency components. On the contrary, a longer SE can extract a smaller number of spikes enhancing lower frequency components. A proper SE can help produce defect frequency accurately in terms of both frequency components and amplitude. When changing the length of SE, each extracted defect frequency can be compared with the theoretical defect frequency. The SE value that produces the distinct defect frequency will be used.

6.2.4 Validation on a small-scale bearing

In this subsection, we aim to evaluate the effectiveness of the INF and morphological analysis on a widely used small-scale bearing with a seeded inner race fault from the SpectraQuest Machinery Fault Simulator test rig [217]. The theoretical inner race defect frequency is 157.4 Hz. After applying INF to the raw vibration signal (Fig.6.6(a1)), the denoised signal shown in Fig.6.6(a2) can clearly present the submerged bearing fault signals. Furthermore, morphological envelope analysis is utilized in order to present the bearing defect frequency. It can be found in Fig.6.6(b), the dominant frequency component is 156 Hz which corresponds to the bearing inner race fault frequency. As a result, this validation experiment demonstrates that our proposed method is effective and accurate.

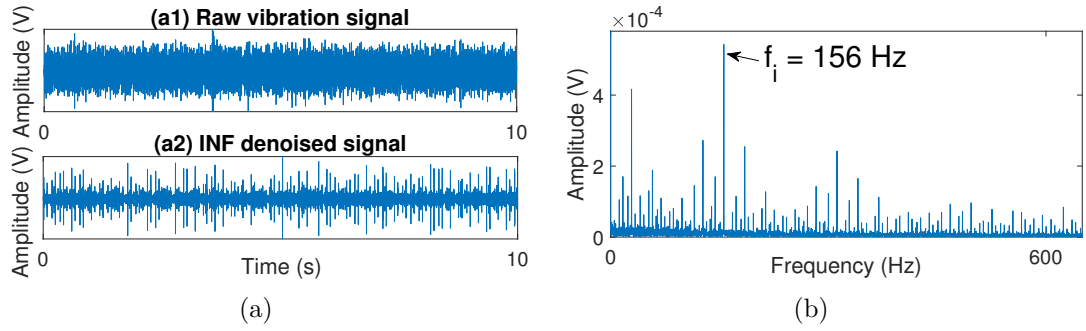


Fig. 6.6. High-speed bearing (a1) raw vibration signal (a2) INF denoised signal and (b) frequency spectrum processed by morphological envelope method.

Table 6.1

Bearing defect frequencies.

Test	Rotation speeds (r/min)	f_i (Hz)	f_o (Hz)	f_b (Hz)
Test 1	2.13	1.1019	1.0279	0.3282
Test 2	1.27	0.6569	0.6129	0.1957

6.3 Experiment and results

In order to diagnose the failure type of this blade bearing, the bearing test-rig is designed as shown in Fig.4.3. The weight of this bearing is 261 kg and its pitch diameter, ball diameter, ball numbers and contact angle are 1000 mm, 54 mm, 60 and 50° respectively. Based on these geometric parameters, the bearing defect frequencies are calculated using (4.1) to (4.3) and are listed in Table 6.1.

Vibration signals of the blade bearing shown in Fig.4.3 are collected from accelerometers installed on the bearing outer ring surface. The accelerometers are Hansford HS-100-type sensors with 1000 mV/g sensitivity and constant frequency gain between 2 Hz to 10 kHz. To simulate the schematic of field operation shown in Fig.4.2, Fig.6.7(a) shows Test 1 raw vibration data at a sampling rate of 100 kS/s. The bearing rotating process includes accelerating, constant speed and decelerating within 100° . Fig.6.7(b) shows the recombined signals with four 90° portions of vibration data. Each part is extracted from each revolution and the extracted parts have similar vibration characteristics with the rotation speed of 2.13 r/min. As can be seen, the kurtosis of the recombined raw signal is only 125.46. The new INF is a combination of the nonlinear diffusion filter and DRS method. To demonstrate its performance, only the nonlinear

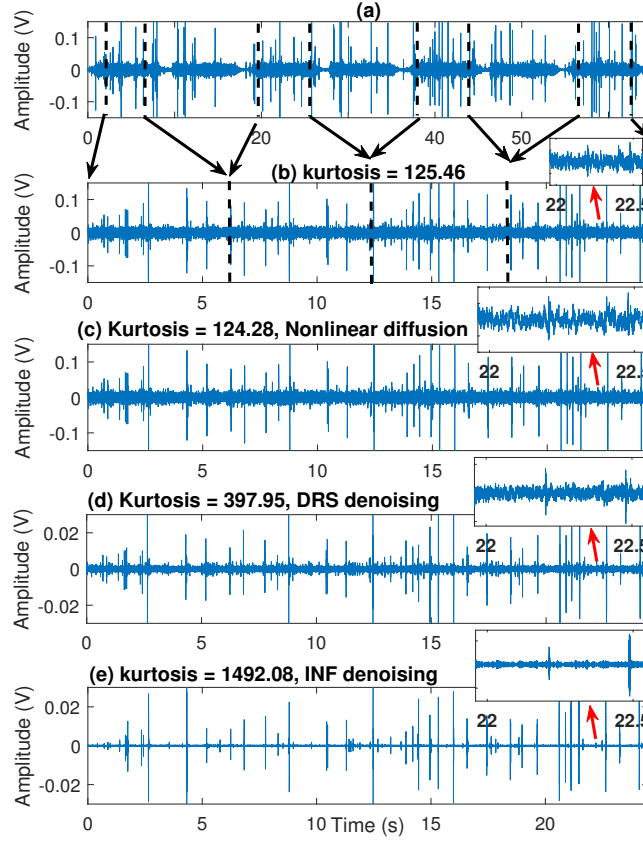


Fig. 6.7. Test 1, (a) raw vibration signal collected under the reciprocating operation condition, (b) recombined signal at 2.13 r/min, (c) nonlinear diffusion denoised signal, (d) DRS denoised signal and (e) INF denoised signal.

diffusion filter is firstly utilized to denoise the recombined signal. After carefully tuning the parameters, the kurtosis of the nonlinear diffusion denoised signal decreases to 124.28 (Fig.6.7(c)). Then, we utilize DRS to denoise the recombined signal. As can be seen in Fig.6.7(d), the kurtosis of the DRS denoised signal improves to 397.95. However, some weak fault signals are still corrupted by noise. In order to overcome this issue, the proposed INF method is then used, with the denoised signal depicted in Fig.6.7(e). Compared with the DRS denoised signal, Fig.6.7(e) shows very low noise interference, with the kurtosis of the filtered signal improving to 1492.08. In order to show the effectiveness of the INF method, some enlarged signals from 22 s to 22.5 s are presented in Fig.6.7(b)(c)(d) and (e). It can be clearly seen that the new INF method can produce better filtering results with clearer defect signals than the nonlinear diffusion filter and DRS method.

With regard to Test 2, Fig.6.8(a) displays the raw vibration signal where the constant part has a speed of 1.27 r/min. Fig.6.8(b) shows the recombined signal. As can

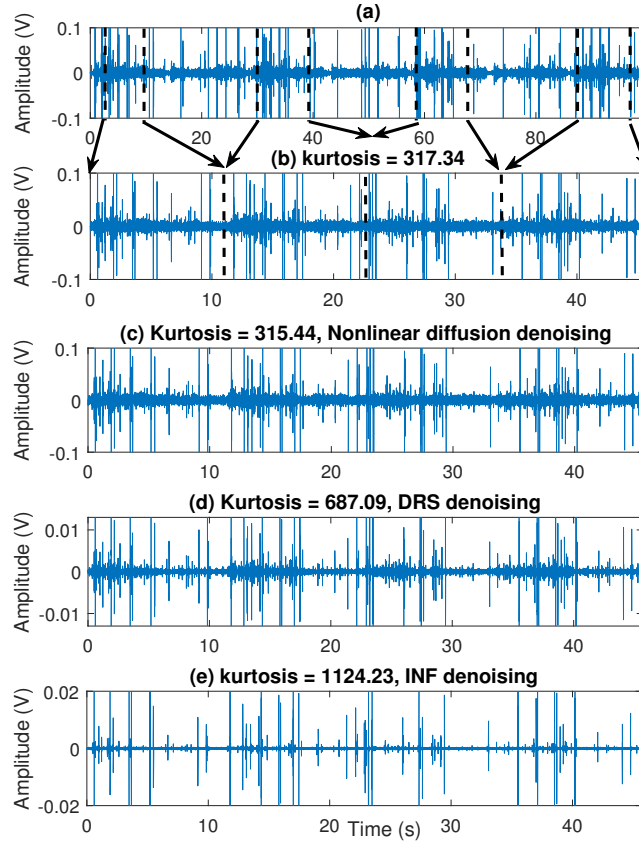


Fig. 6.8. Test 2, (a) raw vibration signal collected under the reciprocating operation condition, (b) recombined signal at 1.27 r/min, (c) nonlinear diffusion denoised signal, (d) DRS denoised signal and (e) INF denoised signal.

be seen in Fig.6.8(b), the kurtosis of the recombined raw signal is 317.34. Then, we utilize nonlinear diffusion filter to denoise the recombined signal and the kurtosis value decreases to around 315.44 (see Fig.6.8(c)). After applying DRS to filter the recombined signal, the kurtosis value improves to 687.09 (see Fig.6.8(d)). In order to further denoise the recombined signal and extract weak fault signals, the novel INF is utilized. As shown in Fig.6.8(e), the compounded fault signals are clearly presented with minimal noise interference and the kurtosis value improves from 317.34 to 1124.23.

The second stage is to extract morphological closing envelopes with the aim of finding defect frequencies in the frequency domain. The morphological closing envelope modifies the geometrical characteristics by morphologically processing the signal which can further extract impulsive-type fault signals. After applying FFT to the morphological closing envelopes, the dominant frequencies are 1.102 Hz for 2.13 r/min and 0.657 Hz for 1.27 r/min shown in Fig.6.9(a) and Fig.6.10(a), respectively.

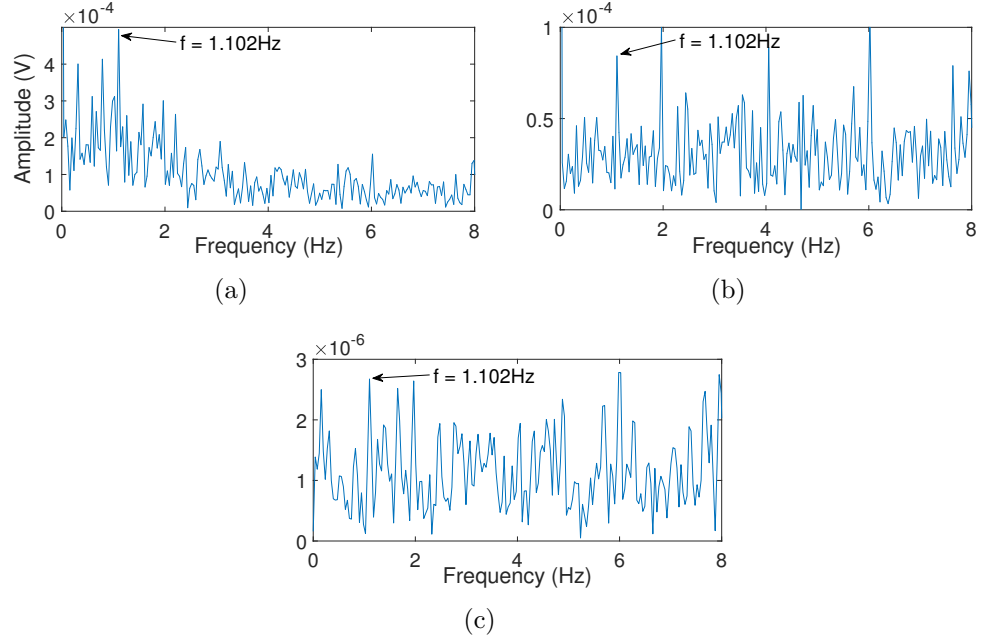


Fig. 6.9. Test 1 at 2.13 r/min, frequency spectrums processed by (a) INF/morphological closing envelope method, (b) INF/Hilbert envelope method and (c) fast kurtogram/Hilbert envelope method.

As our proposed blade bearing diagnostic method has two parts containing INF filtering and morphological envelope analysis, in order to evaluate the performance of the proposed method, some comparisons with Hilbert envelope method and conventional band-pass filtering method are carried out. Fig. 6.9(b) and Fig.6.10(b) display the combination of INF and the Hilbert envelope method. Although this method can show defect frequencies, some other unknown frequency components are also presented, meaning that the defect frequencies are unnoticeable.

Fig.6.9(c) and Fig.6.10(c) demonstrate the frequency spectrum processed by the fast kurtogram analysis [206]. As can be seen, the defect frequencies are relatively weaker and harder to distinguish when compared with the results produced by the new method.

The equation below is used to evaluate the defect frequency matching error (DFME) which is the ratio between the identified dominant frequency and the theoretical defect frequency:

$$\text{Error} = (|f_{\text{rotation}} - f_{\text{fault}}| / f_{\text{fault}}) \times 100\% \quad (6.19)$$

where f_{rotation} indicates the dominant frequencies for each test and f_{fault} can be chosen as f_i , f_o and f_b shown in Table 6.1. Table 6.2 lists the DFME of Test 1 and Test 2. It

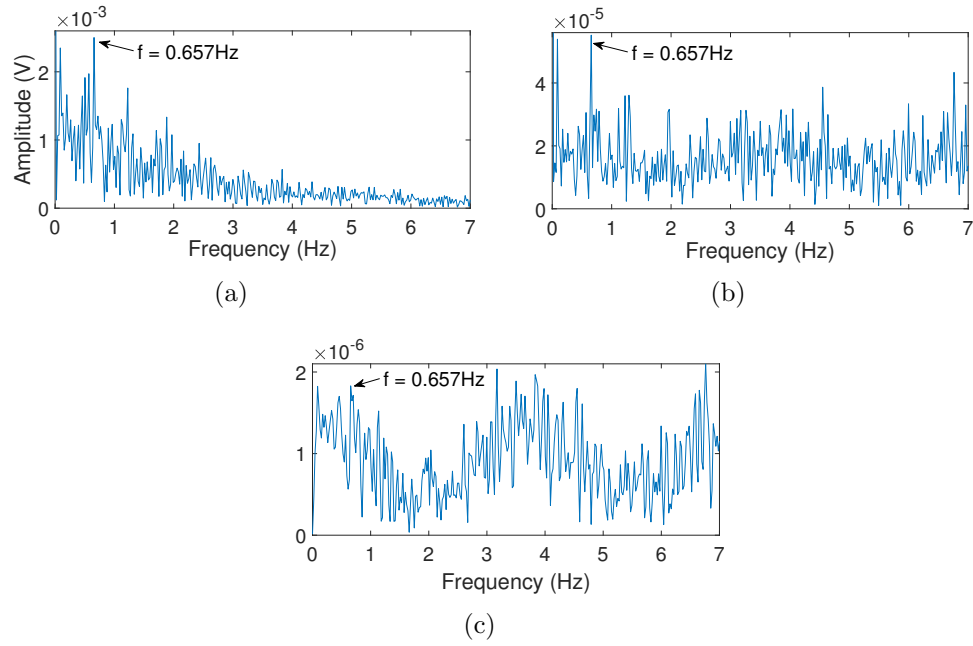


Fig. 6.10. Test 2 at 1.27 r/min, frequency spectrums processed by (a) INF/morphological closing envelope method, (b) INF/Hilbert envelope method and (c) fast kurtogram/Hilbert envelope method.

Table 6.2

DFME of Test 1 and Test 2.

Test	r/min	Inner race fault	Outer race fault	Ball race fault
Test 1	2.13	0.10%	7.21%	235.77%
Test 2	1.27	0.01%	7.20%	235.71%
	Average	0.05%	7.20%	235.74%

is found that the bearing most likely has an inner race fault with an average matching error of 0.05%. To further evaluate our proposed method, the authors conduct extensive experiments to simulate different slow-speed and limited angle cases. As shown in Table 6.3, the bearing defect frequencies can be identified and they all match the theoretical inner race defect frequencies.

6.4 Conclusion

This chapter has diagnosed a naturally damaged wind turbine blade bearing. The blade bearing pitch processes include launching periods, constant speeds and ending periods. To avoid the non-stationary signals caused by launching and ending periods, the work of this chapter is to diagnose the blade bearing fault types when the

Table 6.3

DFME of extensive experiments.

Rotation speeds (r/min)	1.07	1.31	2.14	2.21	3.10	3.12
Identified defect frequency (Hz)	0.552	0.666	1.106	1.116	1.602	1.612
Inner race DFME	0.13%	1.65%	0.09%	2.38%	0.10%	0.12%
Outer race DFME	7.05%	5.42%	7.09%	4.64%	7.08%	7.06%
Balls DFME	235.2%	230.1%	235.3%	227.6%	235.3%	235.2%

signals generated from launching and ending periods are abandoned, and only constant rotation parts are utilized. As blade bearings rotate at very slow speeds within small angles, vibration signals are short and weak. To improve the diagnostic accuracy, we firstly recombined the segmented constant speed short parts to extend the data length. Then, a novel iterative nonlinear filter was proposed to iteratively and gradually smooth the signal waveform and extract weak fault signals. Lastly, the morphological closing envelope method was used to diagnose the bearing fault in the frequency domain. The proposed method was successfully applied to diagnose a naturally damaged blade bearing under different slow-speed conditions and it was effective and superior to other conventional filtering methods or the Hilbert envelope method.

Chapter 7

Vibration Fault Diagnosis Using Bayesian Augmented Lagrangian Analysis

7.1 Introduction

Blade bearings are vital components to achieving blade pitch processes, performing aerodynamic braking and transmitting blade loads into the hub. Their failure can result in lost control of blades, which can further reduce energy production. To diagnose blade bearing fault types, the following two significant challenges need to be solved: 1) the fault signals are weak under slow speed conditions and 2) the disturbances from the blade flapping and dynamic wind loads can cause fluctuating rotation speeds. As a result, it is necessary to design effective denoising methods to extract weak fault signals under fluctuating or variable speed conditions, and then resample the speed-related vibration signals into stationary operations.

For wind turbine blade bearing fault diagnosis, the weak fault signals mean that the signal-to-noise ratio (SNR) is low and a good filtering method is desirable. Furthermore, for fluctuating rotating operations together with the nonlinear vibration introduced by the blade, bearing and drive, this could result in noise signals (or non-fault

signals). As the dominant components of the noise signals are primarily generated by the aforementioned mechanical operations, they are time-series signals. If the raw signals can be estimated using a linear combination or superposition of their previous values (linear auto-regression), the noise signals will be linearly dominated. If the raw signals can be approximated by nonlinear relations (e.g. polynomial based nonlinear auto-regression), the noise signals will be non-linearly dominated. The conventional noise cancellation methods, such as Self-Adaptive Noise Cancellation (SANC) [207] and Discrete/Random Separation method (DRS) [208], can only solve the linear autoregressive problem and remove the linear noise effects from the noise components. If the nonlinear noise effects are inconspicuous, the unsupervised noise cancellation method can be adopted. However, if the nonlinear noise are significant, the nonlinear filter will be desirable. In order to remove the nonlinear noise effects, we investigate the use of sparse representation to produce sparse models for vibration signal denoising.

With respect to sparse representation, its efficiency has been demonstrated in many machinery fault diagnoses, including some works on bearing fault diagnosis. For example, the review papers [218, 219] cover extensive overviews of sparse representation applications to bearing fault diagnosis. When the sparse method is used, the first step is to design a dictionary that captures statistical structures of the raw signal. Then, signal denoising can be achieved through sparse representations within which redundant information is eliminated [220, 221]. The choice of the dictionary is divided into two categories which are the analytic-based and learning-based dictionary [222]. In the analytic-based approach, the dictionary is constructed based on a mathematical model derived from the signal transform, such as time-frequency dictionaries, cosine-packet dictionary, wavelet dictionary, Gabor dictionary, etc. For example, Yang et al. [223] used time-frequency dictionaries to extract impulsive-type fault signals generated from rolling elements bearings. Wang et al. [224] designed a time-varying cosine-packet dictionary. Then, a sparse coefficient spectrum (SCS) of the vibration envelope is built based on the designed dictionary and the wind turbine generator bearing faults can be diagnosed from the SCS. Du et al. [225] used Gabor dictionaries to sparsely represent different kinds of gearbox vibration signals, and spectrum analysis is employed to identify the gearbox characteristic frequency. Liu et al. [226] directly utilized the

defective impulse as the dictionary and then built a sparse model for bearing vibration signal denoising. The aforementioned literature is helpful for bearing fault detection; while it requires many additional constraints or assumptions for dictionary design. To overcome this issue, the second approach is that the dictionary is inferred by some learning techniques, such as singular value decomposition (SVD), K-singular value decomposition (K-SVD), principal component analysis (PCA), etc. The previous studies based on the learning-based dictionaries are briefly summarized as follows. Hou et al. [227] diagnosed the rolling element bearings by using dictionary learning and sparse representation. The designed dictionary is constructed through singular value decomposition (SVD). Zhao et al. [228] constructed a dictionary based on K-singular value decomposition (K-SVD) and orthogonal matching pursuit (OMP) for sparse classification. Yang et al. [229] designed a shift-invariant K-SVD dictionary for wind turbine generator bearing fault diagnosis. After analysing the sparse model, the bearing faults can be diagnosed. However, the process of dictionary learning usually requires a large amount of data for training, which is time-consuming and may be more suitable for off line diagnosis.

In this chapter, to design a fast and easily implemented sparse representation technique for blade bearing fault diagnosis, the dictionary design is simplified by using a nonlinear autoregressive model but without sacrificing the filtering performance, which can effectively describe the nonlinear noise effects of the pitch system under fluctuating rotation speeds. Then, a novel method called Bayesian Augmented Lagrangian (BAL) algorithm is used to build a sparse solution [230]. The characteristic of this method is that it can convert the original denoising problem into several sub-optimization problems under the Bayesian framework and these sub-optimization problems can be solved separately. Therefore, BAL reduces computational requirements and further saves running time [230]. Finally, as the blade bearing rotates under fluctuating speed conditions because of dynamic wind loads or blade flapping, the BAL denoised signals are resampled through angular resampling based on the collected shaft speeds, and the bearing fault can be diagnosed in the order domain. This process can eliminate spectrum smearing and improve diagnostic accuracy [152].

7.2 Theoretical background

7.2.1 Sparse Bayesian Learning

The noise components are often generated from blade bearing rotation movements having some deterministic properties in the time domain.

Let $x(t)$ be a raw vibration signal of length $M + B$ where the parameters M and B are related to the dimensions of the designed dictionary used later in this chapter. Assuming $x(t)$ can be partitioned into segments where each segment is $y(n)$ with length $M + N$. The parameter N also represents the dimension of the designed dictionary. The expression of the segmented signal can be described as [207]:

$$y(n) = d(n) + \xi(n), \quad n = 1, \dots, M + N \quad (7.1)$$

where $y(n)$ is the model signal. $d(n)$ represents the deterministic components containing noise components and $\xi(n)$ demonstrates stochastic components including bearing fault signals. The deterministic components $d(n)$ can be estimated by using a nonlinear autoregressive model

$$\begin{aligned} \hat{d}(n) &= \sum_{i_1=1}^M y(n - i_1)\theta_{i_1} + \sum_{i_2=1}^M y(n - i_2)^2\theta_{i_2} + \dots \\ &\quad + \sum_{i_\Upsilon=1}^M y(n - i_\Upsilon)^\Upsilon \theta_{i_\Upsilon} \\ &= \sum_{j=1}^{\Upsilon} \sum_{i_j=1}^M y(n - i_j)^j \theta_{i_j} \end{aligned} \quad (7.2)$$

where $\Upsilon \in \mathbb{Z}$ which is named as the Nonlinear Order Index (NOI). (7.2) introduced above can be represented as the following matrix format

$$\hat{\mathbf{D}} = \mathbf{P}\mathbf{\Theta} \quad (7.3)$$

where the vector $\hat{\mathbf{D}} = [\hat{d}(M+1), \hat{d}(M+2), \dots, \hat{d}(M+N)]^T$ indicates the deterministic components and $\mathbf{\Theta} = [\theta_1, \theta_2, \dots, \theta_{\Upsilon M}]^T$ demonstrates the sparse coefficient vector. The

dictionary matrix \mathbf{P} as shown in (7.4) is an $N \times \Upsilon M$ matrix.

$$\mathbf{P} = \begin{bmatrix} y(M) & y(M-1) & \cdots & y(1) & \cdots & y(M)^\Upsilon & y(M-1)^\Upsilon & \cdots & y(1)^\Upsilon \\ y(M+1) & y(M) & \cdots & y(2) & \cdots & y(M+1)^\Upsilon & y(M)^\Upsilon & \cdots & y(2)^\Upsilon \\ \vdots & \vdots & \vdots & \vdots & \cdots & \vdots & \vdots & \vdots & \vdots \\ y(M+N-1) & y(M+N-2) & \cdots & y(N) & \cdots & y(M+N-1)^\Upsilon & y(M+N-2)^\Upsilon & \cdots & y(N)^\Upsilon \end{bmatrix} \quad (7.4)$$

As a result, (7.1) describes as follows

$$\mathbf{y} = \mathbf{P}\boldsymbol{\Theta} + \boldsymbol{\Xi} \quad (7.5)$$

where the vector $\mathbf{y} = [y(M+1), y(M+2), \dots, y(M+N)]^\text{T}$ indicates the model signal; $\boldsymbol{\Xi} = [\xi(M+1), \xi(M+2), \dots, \xi(M+N)]^\text{T}$ demonstrates stochastic components including bearing fault signals.

In order to obtain an ideal representation of the deterministic components $\hat{\mathbf{D}}$, the size of the dictionary matrix \mathbf{P} should be large enough to cover sufficient information so that the unknown deterministic components can be precisely described. However, the elements inside the dictionary matrix \mathbf{P} are often redundant and may not be needed for model representation. As a result, a sparse representation is always desirable [224, 230]. In recent years, sparse Bayesian learning (SBL) has been developed under the Bayesian framework which can build a sparse model by selecting suitable dictionary elements and iteratively calculate the solution. According to SBL, the sparse solution of $\mathbf{y} = \mathbf{P}\boldsymbol{\Theta} + \boldsymbol{\Xi}$ can be obtained by solving the following optimization problem with l_1 -norm minimization problem [230]:

$$\hat{\boldsymbol{\Theta}}_k = \arg \min_{\boldsymbol{\Theta}} \left\{ \frac{1}{2} \|\mathbf{P}\boldsymbol{\Theta} - \mathbf{y}\|_2^2 + \lambda \|\mathbf{G}\boldsymbol{\Theta}\|_1 \right\} \quad (7.6)$$

where $\hat{\boldsymbol{\Theta}}_k$ is the estimated sparse coefficient vector at k th iteration, λ is the penalty parameter and \mathbf{G} is a diagonal matrix. The k th iteration of \mathbf{G} can be expressed as follows

$$\mathbf{G}_k = \text{diag}[\mathbf{P}^\text{T}(\lambda\mathbf{I} + \mathbf{P}\boldsymbol{\Gamma}_k\mathbf{P}^\text{T})^{-1}\mathbf{P}]^{\frac{1}{2}} \quad (7.7)$$

where \mathbf{I} is the identity matrix and $\mathbf{\Gamma}_k = \text{diag}[\hat{\gamma}_k]$ with $(\hat{\gamma}_k)_j = |(\hat{\boldsymbol{\Theta}}_k)_j| / (\mathbf{G}_{k-1})_j$ and j indicates the j th element.

7.2.2 Bayesian Augmented Lagrangian algorithm for signal denoising

In order to solve (7.6) in a fast and efficient way, BAL is utilized in this chapter which can construct a sparse model by converting the weighted l_1 -norm minimization problem into some subproblems. Furthermore, at each iteration, the penalty parameter λ is updated which can reduce the iteration steps and increase the calculation speeds.

From Ref. [230], the weighted l_1 -norm minimization problem of (7.6) can be further transformed into a quadratic penalty problem

$$\min_{\boldsymbol{\Theta}, v \in \mathbf{R}^M} f_1(\boldsymbol{\Theta}) + f_2(v) + \frac{\mu}{2} \|\mathbf{G}\boldsymbol{\Theta} - v\|_2^2 \quad (7.8)$$

where $f_1(\boldsymbol{\Theta}) = \frac{1}{2} \|\mathbf{P}\boldsymbol{\Theta} - \mathbf{y}\|_2^2$, $f_2(v) = \lambda \|v\|_1$ and μ indicates Lagrange multiplier. As the value μ increases, the solution of the (7.8) is consequently approximate to the weighted l_1 -norm minimization problem (7.6). According to the Augmented Lagrangian method, the optimization problem (7.8) can be expressed as follows [230]:

$$\begin{aligned} L_\mu(\boldsymbol{\Theta}, v, u) = & f_1(\boldsymbol{\Theta}) + f_2(v) - u^T(\mathbf{G}\boldsymbol{\Theta} - v) \\ & + \frac{\mu}{2} \|\mathbf{G}\boldsymbol{\Theta} - v\|_2^2 \end{aligned} \quad (7.9)$$

where u indicates a vector of Lagrange multipliers. Substituting $d = u/\mu$ into the (7.9), then the problem is converted to the following form:

$$L_\mu(\boldsymbol{\Theta}, v, d) = f_1(\boldsymbol{\Theta}) + f_2(v) + \frac{\mu}{2} \|\mathbf{G}\boldsymbol{\Theta} - v - d\|_2^2 \quad (7.10)$$

Here, (7.10) can be solved by transforming it into three sub-optimization problems which are to solve the variables $\boldsymbol{\Theta}$, u and d individually. These three subproblems are

$$\hat{\Theta}_k = \arg \min_{\Theta} f_1(\Theta) + \frac{\mu}{2} \left\| \mathbf{G}_{k-1} \Theta - v_{k-1} - d_{k-1} \right\|_2^2 \quad (7.11)$$

$$v_k = \arg \min_v f_2(v) + \frac{\mu}{2} \left\| \mathbf{G}_{k-1} \hat{\Theta}_k - v - d_{k-1} \right\|_2^2 \quad (7.12)$$

$$d_k = d_{k-1} - (\mathbf{G}_{k-1} \hat{\Theta}_k - v_k) \quad (7.13)$$

The solution of (7.11) and (7.12) can be calculated as

$$\begin{aligned} \hat{\Theta}_k = & (\mathbf{P}^T \mathbf{P} + \mu \mathbf{G}_{k-1}^T \mathbf{G}_{k-1})^{-1} \\ & (\mathbf{P}^T \mathbf{y} + \mu \mathbf{G}_{k-1}^T (v_{k-1} + d_{k-1})) \end{aligned} \quad (7.14)$$

and

$$\begin{aligned} v_k = & \max(0, (\mathbf{G}_{k-1} \hat{\Theta}_k - d_{k-1}) - \mu/\lambda_{k-1}) \\ & - \max(0, -(\mathbf{G}_{k-1} \hat{\Theta}_k - d_{k-1}) - \mu/\lambda_{k-1}) \end{aligned} \quad (7.15)$$

Therefore, (7.13), (7.14) and (7.15) can be iteratively calculated to produce a sparse solution. Moreover, to obtain an ideal sparse model with fewer iterations, the penalty parameter λ is also a key factor that needs to be tuned. For this chapter, parameter tuning is based on the previous modeling error $\varepsilon_k = \left\| \mathbf{P} \hat{\Theta}_k - \mathbf{y} \right\|_2^2$ which adaptively adjusts the penalty parameter λ at each iteration. The process is as follows

$$\lambda_k = \begin{cases} \alpha \lambda_{k-1}, (\alpha > 1) & \text{if } \left| \frac{\varepsilon_k}{\varepsilon_{k-1}} - 1 \right| < 0.05 \\ \beta \lambda_{k-1}, (0 < \beta < 1) & \text{if } \left| \frac{\varepsilon_k}{\varepsilon_{k-1}} - 1 \right| \geq 0.05 \end{cases} \quad (7.16)$$

The final consideration for BAL is its stopping criteria. BAL can build an ideal sparse model if appropriate stopping criteria are applied. Here, the stopping criteria are that if the nonzero elements of $\hat{\Theta}_k$ and $\hat{\Theta}_{k-1}$ have the same sign and location, the iteration will stop at k th [230].

The raw signal $x(t)$ ($x(t) \supseteq y(n)$), $t = 1, \dots, M + B$, can be denoised when the sparse

Algorithm 1 BAL denoising

Ensure: $k = 0$, $\mu = 0.1$, $\lambda_0 = 0.1$, $v_0 = d_0 = 0$, $\mathbf{G}_0 = \mathbf{I}$ and $\mathbf{X} \supseteq \mathbf{y}$

- 1: **while** the nonzero elements of $\hat{\boldsymbol{\Theta}}_k$ and $\hat{\boldsymbol{\Theta}}_{k-1}$ have the same sign and location **do**
- 2: $\hat{\boldsymbol{\Theta}}_k = (\mathbf{P}^T \mathbf{P} + \mu \mathbf{G}_{k-1}^T \mathbf{G}_{k-1})^{-1} (\mathbf{P}^T \mathbf{y} + \mu \mathbf{G}_{k-1}^T (v_{k-1} + d_{k-1}))$
- 3: $v_k = \max(0, (\mathbf{G}_{k-1} \hat{\boldsymbol{\Theta}}_k - d_{k-1}) - \mu/\lambda_{k-1}) - \max(0, -(\mathbf{G}_{k-1} \hat{\boldsymbol{\Theta}}_k - d_{k-1}) - \mu/\lambda_{k-1})$
- 4: $d_k = d_{k-1} - (\mathbf{G}_{k-1} \hat{\boldsymbol{\Theta}}_k - v_k)$
- 5: $\mathbf{G}_k = \text{diag}[\mathbf{P}^T (\lambda_{k-1} \mathbf{I} + \mathbf{P} \boldsymbol{\Gamma}_k \mathbf{P}^T)^{-1} \mathbf{P}]^{\frac{1}{2}}$, $\boldsymbol{\Gamma}_k = \text{diag}[\hat{\gamma}_k]$, $(\hat{\gamma}_k)_j = |(\hat{\boldsymbol{\Theta}}_k)_j| / (\mathbf{G}_{k-1})_j$
- 6: $\varepsilon_k = \|\mathbf{P} \hat{\boldsymbol{\Theta}}_k - \mathbf{y}\|_2^2$
- 7: $\lambda_k = \begin{cases} \alpha \lambda_{k-1}, (\alpha > 1) & \text{if } \left| \frac{\varepsilon_k}{\varepsilon_{k-1}} - 1 \right| < 0.05 \\ \beta \lambda_{k-1}, (0 < \beta < 1) & \text{if } \left| \frac{\varepsilon_k}{\varepsilon_{k-1}} - 1 \right| \geq 0.05 \end{cases}$
- 8: $k \leftarrow k + 1$
- 9: **end while**
- 10: $\mathbf{X}_d = \mathbf{X} - \Delta \hat{\boldsymbol{\Theta}}_k$

Output: The BAL denoised signal \mathbf{X}_d .

model $\hat{\boldsymbol{\Theta}}_k$ is obtained at k th iteration. Similarly with (7.5), the denoised signal $x_d(t)$ is expressed as the following matrix format.

$$\mathbf{X}_d = \mathbf{X} - \boldsymbol{\Lambda} \hat{\boldsymbol{\Theta}}_k \quad (7.17)$$

where $\mathbf{X}_d = [x_d(M+1), x_d(M+2), \dots, x_d(M+B)]^T$, $\mathbf{X} = [x(M+1), x(M+2), \dots, x(M+B)]$ and $\boldsymbol{\Lambda}$ is a constructed raw signal matrix with the dimension of $B \times \Upsilon M$ shown in (7.18):

$$\boldsymbol{\Lambda} = \begin{bmatrix} y(M) & y(M-1) & \cdots & y(1) & \cdots & y(M)^T & y(M-1)^T & \cdots & y(1)^T \\ y(M+1) & y(M) & \cdots & y(2) & \cdots & y(M+1)^T & y(M)^T & \cdots & y(2)^T \\ \vdots & \vdots & \vdots & \vdots & \cdots & \vdots & \vdots & \vdots & \vdots \\ y(M+B-1) & y(M+B-2) & \cdots & y(B) & \cdots & y(M+B-1)^T & y(M+B-2)^T & \cdots & y(N)^T \end{bmatrix} \quad (7.18)$$

Up to now, the raw signal is denoised by BAL which converts the optimization problems into several sub-problems shown in (7.13), (7.14) and (7.15). The main procedure of BAL denoising is described in detail in Algorithm 1.

7.2.3 Angular resampling

Blade bearings may rotate at fluctuating speeds because of blade flipping and dynamic wind loads. This will cause frequency “smearing” meaning that bearing fault features cannot be easily diagnosed. To solve this issue, it is necessary to resample the denoised signal in the order domain which can effectively eliminate the effects of speed fluctuations and frequency smearing. Assuming the rotation speed signal $s(g)$, $g = 1, \dots, G$ is collected from the tachometer with the unit in *rpm*, the rotation signal associated with the shaft can be represented as

$$S(\omega) = \sin \left(\left(\sum_{g=1}^{\omega} \frac{s(g) \cdot 2\pi}{60} \right) / f_{\text{tach}} \right), \quad \omega = 1, \dots, G \quad (7.19)$$

where f_{tach} is the sampling rate of the speed signal. Then, the analytic signal $S_a(\omega)$ associated with $S(\omega)$ is used to extract the phase information.

$$S_a(\omega) = \mathcal{F}^{-1} \{ \mathcal{F} [S(\omega) \cdot \vartheta(\omega)] \} \quad (7.20)$$

where \mathcal{F} and \mathcal{F}^{-1} indicate the Discrete Fourier Transform (DFT) and Inverse DFT respectively, and $\vartheta(\omega)$ is defined as:

$$\vartheta(\omega) = \begin{cases} 1, & \omega = 1, \frac{G}{2} + 1 \\ 2, & \omega = 2, 3, \dots, \frac{G}{2} \\ 0, & \omega = \frac{G}{2} + 2, \dots, G \end{cases} \quad (7.21)$$

The Discrete Hilbert transform (DHT) of $S(\omega)$ is [202]:

$$\mathcal{H} [S(\omega)] = \text{Im}(S_a(\omega)) \quad (7.22)$$

where \mathcal{H} indicates the DHT of $S(\omega)$ and the notation Im indicates the imaginary part of $S_a(\omega)$ [202]. Next, the instantaneous phase $\phi_{\text{inst}}(\omega)$ is

$$\phi_{\text{inst}}(\omega) = \arctan \left\{ \frac{\mathcal{H} [S(\omega)]}{S(\omega)} \right\} \quad (7.23)$$

As the angle increment δ is a constant value, we can assume that the sampling points per shaft revolution (also termed order domain sampling rate) is f_{order} . Therefore, the angle increment can be expressed as $\delta=2\pi/f_{\text{order}}$. Based on this angle increment, the denoised signal can be resampled at constant angular increments in the order domain [231].

7.2.4 Order domain fault diagnosis

If the denoised signal is resampled, we can apply an envelope method to diagnose the bearing fault in the order domain. Similarly with the frequency domain analysis for constant speed cases, the envelope spectrum of the angularly resampled signal is named as order spectrum; and the corresponding order values of different fault types can be expressed as

$$O_{\text{outer}} = \frac{N_b}{2} \left(1 - \frac{d_b}{d_p} \cos \phi \right) / R_{\text{ratio}} \quad (7.24)$$

$$O_{\text{inner}} = \frac{N_b}{2} \left(1 + \frac{d_b}{d_p} \cos \phi \right) / R_{\text{ratio}} \quad (7.25)$$

$$O_{\text{ball}} = \frac{d_p}{2d_b} \left(1 - \left(\frac{d_b}{d_p} \cos \phi \right)^2 \right) / R_{\text{ratio}} \quad (7.26)$$

where O_{outer} indicates fault characteristic order (FCO) of the outer ring, O_{inner} represents FCO of the inner ring and O_{ball} is indicated as the FCO of the balls. R_{ratio} is the speed ratio between the measured shaft speed from a tachometer and the bearing rotation speed. Therefore, these three FCOs are comparative values which depend on where the speed measurement is taken. For example, if the tachometer can directly measure the bearing shaft speed, R_{ratio} will be set to 1; whereas, it is worth mentioning that the blade bearing rotation speed is very difficult to be measured accurately because it rotates very slowly. A possible solution is to measure the shaft speed of the driving machines, such as the gearbox and motor, which have relatively higher rotation speeds. According to the ratio R_{ratio} , we can obtain the FCOs based on this

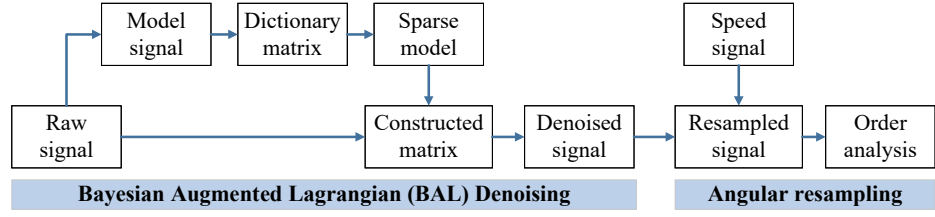


Fig. 7.1. Flowchart of the proposed method for blade bearing fault detection under variable speed conditions.

measured shaft speed.

7.2.5 Summary of the algorithm

With all the equations introduced above, the flowchart of the blade bearing fault diagnosis technique under variable or fluctuating speed conditions can be presented in Fig.7.1. As can be seen in the flowchart, the blade bearing fault diagnosis consists of two stages which are BAL denoising and angular resampling.

With regard to BAL, one of the key factors is the penalty parameter λ . The optimal value of λ can help in obtaining a satisfied sparse solution and reducing the iterations; however, there is a dearth of information about presetting it. In this chapter, for convenience purposes, the initial λ is fixed at 0.1 and the BAL technique can update the penalty parameter λ at each iteration. The other prominent factor of BAL is to construct the dictionary \mathbf{P} . From (7.4), we can see it is an $N \times \Upsilon M$ matrix including the elements from $y(1)$ to $y(M + N)$; therefore, the choice of model signal $y(n)$, $n = 1, \dots, M + N$ is vitally important. To find an ideal $y(n)$, we utilize the kurtosis criterion as the filtering performance indicator. The high kurtosis value can give an indication that the denoised signal contains a great deal of spikes. Then, 3D planes based on different Υ s and calculated parameters M and N are presented in order to lock the position with the largest kurtosis value. After the signal is denoised, the final stage is to resample the denoised signal and diagnose the bearing fault in the order domain.

7.3 Validation experiment

7.3.1 Validation on a seeded defect bearing

In this subsection, we use an open bearing dataset (the dataset numbering is O-A-2) from the SpectraQuest machinery fault simulator to validate the effectiveness of the introduced framework [232]. The test bearing has a seeded outer race fault and its theoretical FCO of the outer race is $O_{\text{outer}} = 3.57$. Fig.7.2(a) displays the raw vibration signal which was collected at the speed from 774 rpm to 1380 rpm.

Two popular methods, discrete/random separation (DRS) [233] and fast kurtogram methods [206], are utilized to compare with the new BAL method in terms of their filtering performance. Here, we firstly use the discrete/random separation (DRS) method to filter the data. From [233], the tunable parameters of the DRS method are the filter length and time delay. Consequently, to evaluate the filtering performance, we use different filter lengths and time delays, and evaluate their impacts on the denoising performance indicator, the kurtosis criterion. The high kurtosis value may indicate that the signal is heavily denoised. As can be seen in Fig.7.3. the highest kurtosis value is 103.52 when the filter length is 18 and the time delay is 1162. Based on these parameters, the DRS denoised signal is displayed in Fig.7.2(b). Furthermore, the same raw vibration signal is also processed using the fast kurtogram method [206]. Fig.7.2(c) displays the denoised signal based on the generated kurtogram and the kurtosis value increases to 166.72.

For the new BAL method, it has three initial parameters, the row of the dictionary (N), the column of the dictionary (M) and the NOI (Υ). Different initial values are used and their effect on kurtosis criterion have been shown in Fig.7.4. As can be seen, the highest kurtosis is 912.45 when $\Upsilon = 3$, $N = 1280$ and $M = 7$. Therefore, according to (7.4), we construct a 1280×21 dictionary matrix for BAL denoising. After 2 iterations with only 0.126008 seconds [our tests are implemented using a laptop with an Intel(R) Core(TM) i7-7700HQ CPU and 16 GB memory], the sparse model $\hat{\Theta}_2$ is built. Fig. 7.5 is the sparse coefficient vector for the validation experiment. As can be seen, only 7 nonzero sparse coefficients (inside red text-box) are presented meaning that

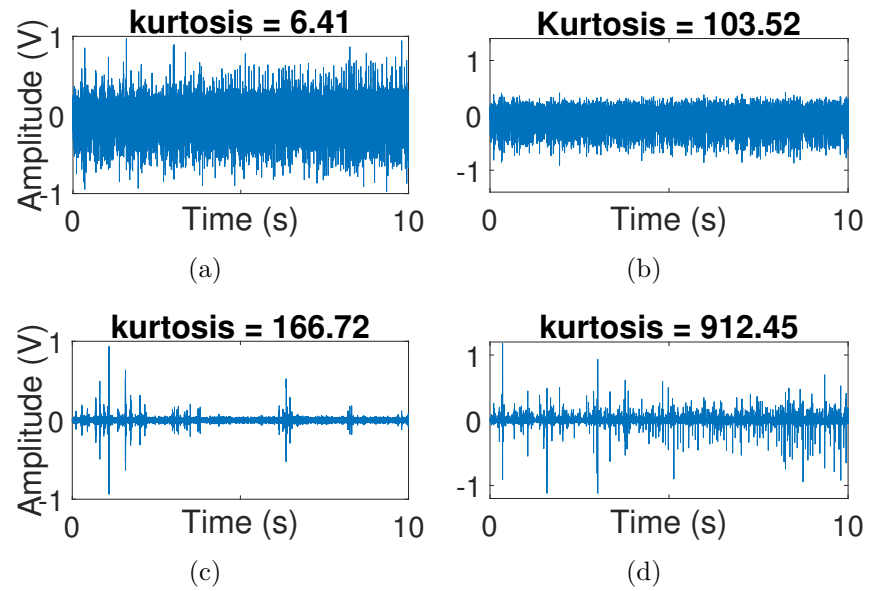


Fig. 7.2. (a) Raw vibration signal and denoised signals obtained by the (b) DRS method, (c) Fast Kurtogram method and (d) BAL method.

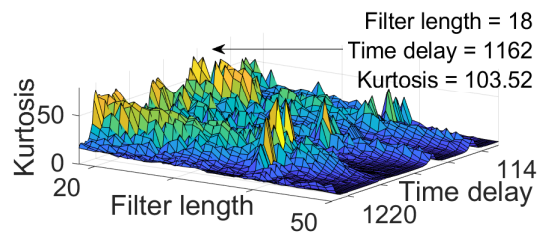


Fig. 7.3. DRS method, Kurtosis VS Filter length and Time delay.

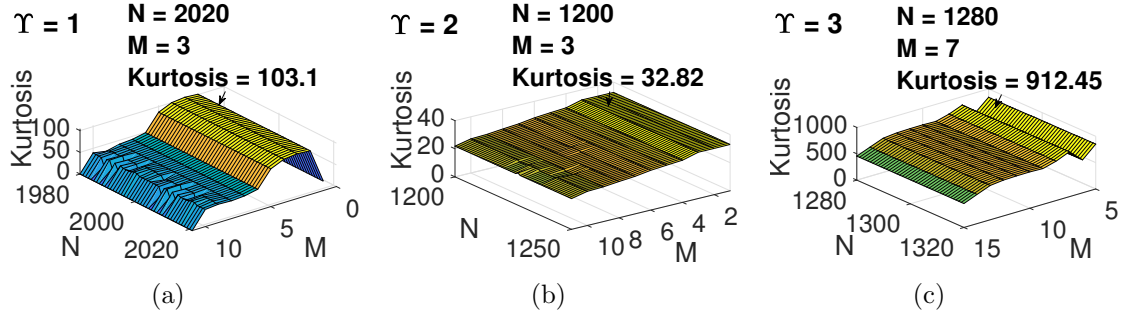


Fig. 7.4. BAL method, Kurtosis VS N and M (a) $\Upsilon = 1$, (b) $\Upsilon = 2$ and (c) $\Upsilon = 3$.

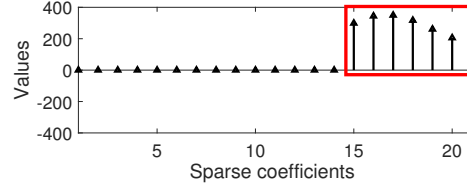


Fig. 7.5. The results of sparse coefficients.

the deterministic components can be represented from the corresponding 7 dictionary terms. Fig.7.2(d) depicts the BAL denoised signal with lower noise interferences where the kurtosis value increases from 6.41 (raw data) to 912.45 (BAL denoised data). Here, for the BAL denoising, the noise reduction capability is more significant than the DRS or fast kurtogram method.

Then, these denoised signals (Fig.7.2(b), Fig.7.2(c) and Fig.7.2(d)) are resampled respectively in the order domain. Fig.7.6 displays the corresponding order spectrums. From Fig.7.6(a) and Fig.7.6(b), the FCOs in these two figures are unclear. In respect of Fig.7.6(c), it illustrates the order spectrum processed using the BAL denoising method where the outer race FCO can be easily identified, which is at 3.306. Therefore, this validation experiment demonstrates that our introduced BAL method has higher filtering performance than the DRS method or the fast kurtogram method to extract fault signals, particularly under the conditions of strong noise disturbances.

7.3.2 Validation on a simulation experiment

To further evaluate the performance of the proposed BAL method, a simulation experiment for the linear and nonlinear noise effect problem is carried out using MATLAB software. To do that, some bearing fault signals are firstly generated with the period

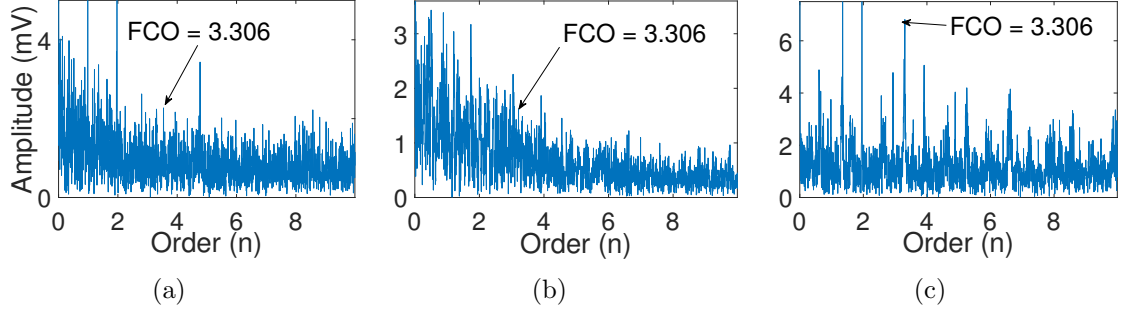


Fig. 7.6. Order spectrum obtained by the (a) DRS method, (b) Fast Kurtogram method and (c) BAL method.

of 1 second [see Fig.7.7(a)]. Then, we use the noise signal [see Fig.7.7(b)] which is collected from the blade bearing test-rig to mask the generated fault signals. The introduction of the blade bearing test-rig will be explained in Section 7.4. It is worth pointing that as the noise signal is collected from the real blade bearing, this simulation experiment has higher credibility for method validation. As can be seen in Fig.7.7(c), the fault signals are disturbed by noise and are very difficult to found. In order to filter the noise masked signal, the BAL method is utilized. Here, we firstly use the linear autoregressive model to filter the data where the NOI (Υ) is set to 1. After carefully tuning the corresponding parameters, as presented in Fig.7.7(d), the quality of the signal has not improved obviously. This is because the linear noise effect is insignificant. Therefore, the nonlinear autoregressive model needs to be deployed. Fig.7.7(e) shows the BAL filtered signal with $\Upsilon = 3$. Compared with Fig.7.7(d), the fault signals in Fig.7.7(e) are extracted and dominated whose kurtosis value improves from 4.55 to 68.29. Hence, the BAL method with the nonlinear autoregressive model is effective for removing the nonlinear noise effects and extracting weak fault signals.

7.3.3 Discussion of the BAL denoising

In conclusion, our introduced BAL denoising method can effectively extract bearing fault signals and its filtering performance is superior to DRS method or fast kurtogram method. Whereas, there are some discussions for the BAL denoising, which are summarized as follows.

- Firstly, compared with the DRS method, the parameter tuning of the BAL is

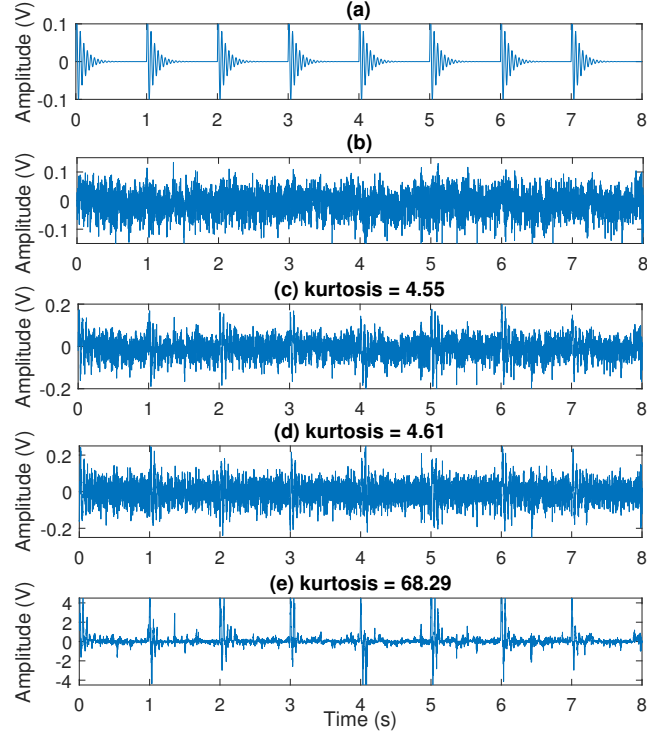


Fig. 7.7. Simulation example (a) generated fault signals, (b) noise signal, (c) noise masked fault signals, (d) filtered signal based on linear autoregressive model ($\Upsilon = 1$) and (d) filtered signal based on nonlinear autoregressive model ($\Upsilon = 3$).

easier. For example, in the light of Fig.7.3, the parameter tuning of DRS method is complicated as the filtering performance is very sensitive to the variations of filter lengths and time delays. In respect of the BAL parameter tuning, according to Fig.7.4, the proposed embedded sparsity makes the filtering results less sensitive to parameter setting. This is because the dictionary matrix in terms of initial parameters Υ , N and M is often redundant. The sparse representation can eliminate redundant information for model construction.

- Secondly, according to (7.2), the new BAL method fully considers the linear and nonlinear characteristics of the signal. On the contrary, the DRS and fast kurtogram methods are linear filtering technique. Therefore, the BAL method offers a promising solution for wind turbine blade bearing fault diagnosis.

7.4 Wind turbine blade bearing fault diagnosis

An industrial-scale and slow-speed wind turbine blade bearing test-rig (see Fig.4.4), imitating the configuration of a blade bearing pitch system, has been designed to evaluate the introduced BAL technique and order analysis. As can be seen, the bearing outer ring is fixed on the test-rig and a 7.75 meter long, 139 kilogram blade is installed on the inner ring. During the experiment, a three-phase induction motor which is coupled with the gearbox can produce power to drive the bearing via the chain drive system; and the bearing rotation speed can be controlled from 0.5 rpm to 5 rpm through the motor inverter. The chain meshes with two sprockets, transmitting rotary motion between the gearbox and bearing. The drive sprocket locked to the shaft of the gearbox has 48 teeth. Meanwhile, the driven sprocket fixed on the blade bearing has 256 teeth. Therefore, the speed ratio R_{ratio} between the gearbox shaft speed and bearing rotation speed is around 5.33 ($\approx 256/48$). To measure the rotation speed, a tachometer is jointed to the gearbox shaft to acquire gearbox shaft speeds.

The test blade bearing is a large-scale slewing bearing which was manufactured by the Rollix company. The weight of this bearing is 261 kg and ball numbers, ball diameter, pitch diameter and contact angle are 60, 54 mm, 1000 mm and 50 °, respectively. According to these geometric parameters, the theoretical FCOs based on the gearbox shaft speeds can be calculated by using (7.24) to (7.26) which are $O_{\text{inner}} = 5.8238$ and $O_{\text{outer}} = 5.4326$ and $O_{\text{ball}} = 1.7348$.

Fig.7.8(a) displays Test 1 gearbox shaft speed with the duration of 200 seconds. As can be seen, the speed variations are from 5.35 rpm to 6.75 rpm. This is because the blade flapping and blade trembling can result in fluctuating bearing rotation speeds. Furthermore, the blade flapping may also introduce additional complicated noise. Fig.7.8(b) displays Test 1 raw vibration signal. The sensor used for vibration signals acquisition is the Hansford HS-100 type accelerometer with the sampling rate at 100 kS/s. As can be seen, the raw signal has compounded fault signals in which the amplitudes of the strong fault signals are over 0.5V and the amplitudes of the weak fault signals are less than 0.05V. In order to denoise the raw signal and extract weak fault signals (see Fig.7.8(b)), we firstly utilize the fast kurtogram method [206] to process the data

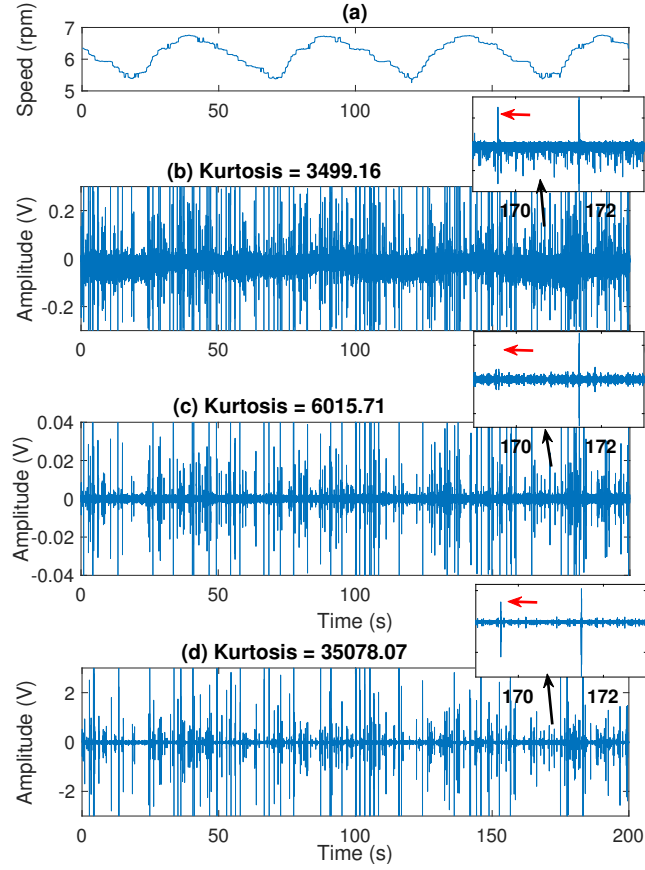


Fig. 7.8. Test 1: (a) Gearbox shaft speed (b) blade bearing raw vibration signal, (c) band-pass filtered signal and (d) BAL denoised signal.

where the selecting frequency band is $[3646\text{Hz}, 4166\text{Hz}]$. As can be seen in Fig.7.8(c), the kurtosis value of the band-pass filtered signal improves to 6015.71. However, if we zoom in the filtered signal from 170 s to 172 s, some weak fault signals are abandoned (see red arrow in Fig.7.8(c)). In order to overcome this problem, the proposed BAL is then used to filter the data. After carefully tuning the Υ , N and M which are displayed in Fig.7.9, we can get the BAL denoised signal depicted in Fig.7.8(d). As can be seen, the kurtosis increases from 3499.16 (raw data) to 35078.07 (BAL denoised data). To demonstrate the effectiveness of the BAL method, we zoom in the signals to show some details from 170 s to 172 s (see Fig.7.8(b), (c) and (d)). Compared with Fig.7.8(b), (c), Fig.7.8(d) denoised by BAL method can clearly show that the noise level decreases, and some small spikes are extracted from the raw data.

To demonstrate the superiority of the proposed BAL method, we compare it with other sparse denoising methods. In contrast to the BAL technique in which the dictionary is developed from the noise components, we use conventional orthogonal matching

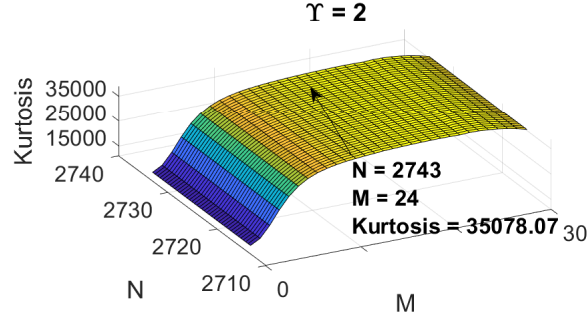


Fig. 7.9. 3D plan for Υ , N and M . The highest kurtosis is 35078.07 under the conditions of $\Upsilon = 2$, $N = 2743$ and $M = 24$.

pursuit (OMP) to process the data where the dictionary is developed from the bearing fault signals. As the OMP method takes significant computational time, only a very small amount of raw signal (0.15 seconds data of Test 1) is used for comparison [see Fig.7.10(a)]. The results of BAL and OMP filtered signals are shown in Fig.7.10(b) and (c), respectively. As can be seen, both methods can reduce noise to an insignificant level. Although OMP is slightly better in term of noise removing, the calculation is very slow and takes 390.02 seconds [the tests are implemented using a laptop with an Intel(R) Core(TM) i7-7700HQ CPU and 16 GB memory]. If we want to process the entire vibration signal of Test 1 (200 seconds) section by section, theoretically, it will take around 6.02 days ($\approx 200/0.15 \times 390.02/3600/24$). On the contrary, for the proposed BAL technique, the calculation only spends 4.12 seconds in processing the entire 200 seconds raw vibration signal. As a result, both methods can process the raw signals, but BAL is efficient which can reduce computational requirements and further save running time.

Then, to compare the diagnostic results with and without angular resampling, the Hilbert envelope method is firstly applied to identify the bearing defect frequency in the frequency domain. It is a frequency relating to balls which pass over the defect point. As the gearbox rotation speed changes from 5.35 rpm to 7.75 rpm, the average bearing rotation speed is at 1.14 rpm ($= (5.35+6.75)/2/5.33$). Based on this speed, the theoretical defect frequencies of the inner race, outer race and balls are $f_{inner} = 0.5897$ Hz, $f_{inner} = 0.5502$ Hz and $f_{ball}=0.1757$ Hz. If the identified defect frequency matches one of the theoretical defect frequencies, the fault type can be inferred. However, after comparing these theoretical defect frequencies and the zoomed frequency spectrum

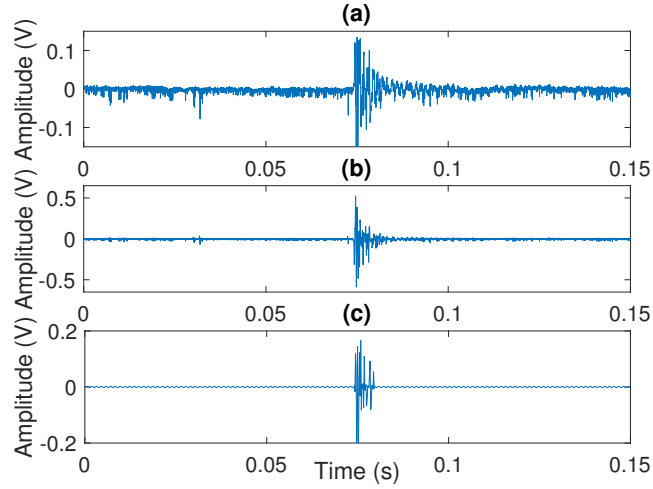


Fig. 7.10. Test 1 with 0.15 seconds: (a) Raw vibration signal, (b) BAL denoised signal and (c) OMP denoised signal.

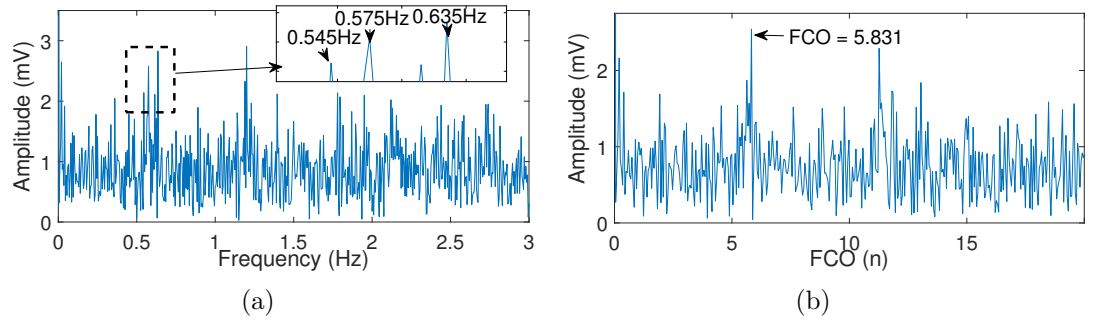


Fig. 7.11. Test 1: (a) frequency spectrum (b) order spectrum based on the gearbox shaft speed.

displayed in Fig.7.11(a), it is very hard to determine its defect frequencies because the bearing rotation speed fluctuates with time meaning that the defect frequencies is smeared. To solve this issue and improve the diagnostic accuracy, the denoised signal is resampled in the order domain based on the collected gearbox shaft speed. The envelope analysis result of the resampled signal is plotted in Fig.7.11(b). In this figure, the bearing FCO is clearly identified, which is at 5.831.

With regard to Test 2, the gearbox speed is increased and the speed variations are from 8.0 rpm to 9.8 rpm, so the imbalanced blade load flapping and blade load trembling can result in more fluctuating bearing rotation speeds. Fig.7.12(a) and (b) show the corresponding gearbox shaft speed signals and bearing raw vibration data with the kurtosis value of 3739.12. After carefully tuning the BAL, the kurtosis value of the denoised signal increase to 110819.71 (see Fig.7.12(c)). If we directly extract its envelope and diagnose the bearing fault type in the frequency domain, the defect

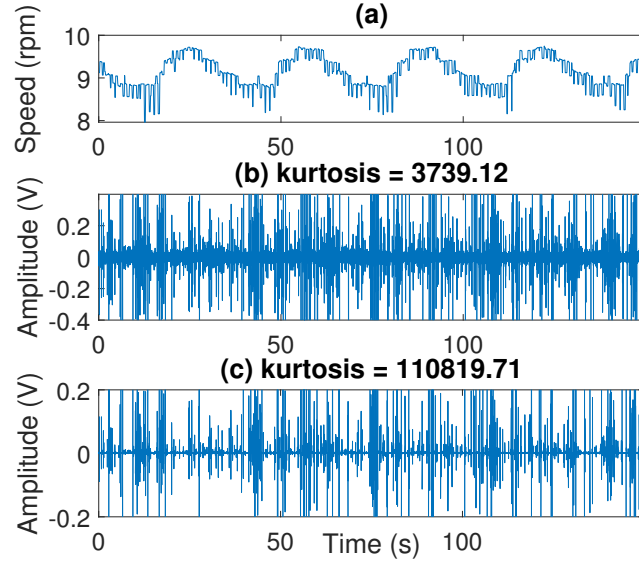


Fig. 7.12. Test 2: (a) Gearbox shaft speed (b) blade bearing raw vibration signal and (c) BAL denoised signal.

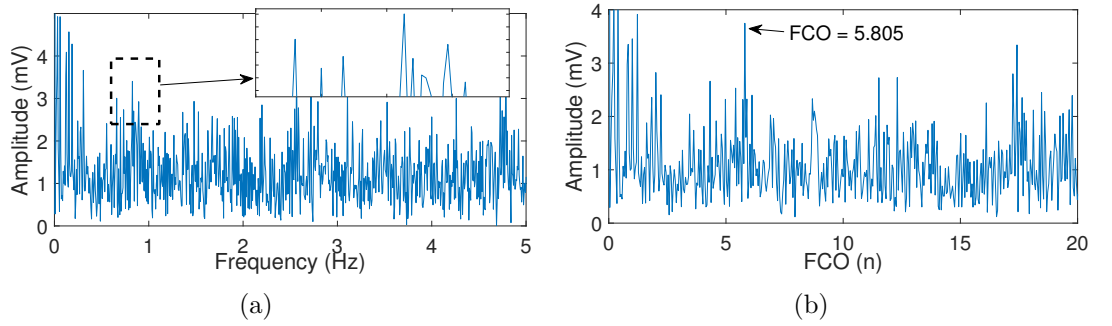


Fig. 7.13. Test 2: (a) frequency spectrum (b) order spectrum based on the gearbox shaft speed.

frequency will be very difficult to distinguish because the defect frequency is smeared as shown in Fig.7.13(a). Finally, the denoised signal is resampled with the aim of finding the FCO in the order domain. Fig.7.13(b) shows the final FCO spectrum based on the collected gearbox shaft speeds. As can be seen, the identified FCO is at 5.805.

Equation (7.27) is used to evaluate the diagnostic accuracy, which is the ratio between the identified FCO and the theoretical FCO.

$$\text{Accuracy} = 1 - (|O_{\text{iden}} - O_{\text{theo}}| / O_{\text{theo}}) \times 100\% \quad (7.27)$$

where O_{iden} is the identified FCOs, and O_{theo} indicates the theoretical FCOs which are $O_{\text{inner}} = 5.8238$, $O_{\text{outer}} = 5.4326$ and $O_{\text{ball}} = 1.7348$. Table 7.1 exhibits the diagnostic accuracy of Test 1 and Test 2 which presents the highest inner race fault average

Table 7.1

Diagnostic accuracy of Test 1 and Test 2.

Test	Inner race fault	Outer race fault	Ball fault
Test 1	99.87%	92.67%	-136.12%
Test 2	99.67%	93.14%	-134.62%
Average	99.77%	92.91%	-135.37%

accuracy. As a result, the bearing inner race fault can be inferred.

7.5 Conclusions

In this chapter, a naturally damaged wind turbine blade bearing is detected under the conditions of fluctuating speeds and blade loads. To extract weak fault signals, Bayesian Augmented Lagrangian algorithm is introduced for signal denoising. The advantages of this method are that the dictionary design is simplified by using a non-linear autoregressive model but without sacrificing the filtering performance. Additionally, Bayesian Augmented Lagrangian can convert the optimization problem into several sub-optimization problems under the Bayesian framework; therefore its fast computation ability means that a sparse solution can be obtained quickly. Finally, to eliminate spectrum smearing and improve diagnostic accuracy, the Bayesian Augmented Lagrangian denoised signal is resampled based on the collected shaft speeds. The diagnostic results show that our proposed framework is efficient and accurate, which demonstrates the wide industrial application potential for blade bearing fault diagnosis.

Chapter 8

Acoustic Emission Fault Diagnosis Using Cepstrum Editing Liftering

8.1 Introduction

Acoustic Emission (AE) analysis which is a promising technique for slow-speed bearing CMFD is utilized for wind turbine blade bearing fault diagnosis. It was firstly used in [234] for slow-speed bearing fault diagnosis at the lowest rotation speed of 10 r/min, and it was shown that the AE signal clearly presents bearing fault signals under slow rotation speed conditions. Later on, AE analysis was used to diagnose slower rolling bearings at rotation speeds from 0.5 r/min to 5 r/min [235]. This study denoted that the AE measurement is a very sensitive method for slow-speed bearing fault detection. Jamaludin et al. [236] analysed AE signal time signatures and their corresponding frequency spectrum to diagnose the slow-speed bearing fault type. Widodo et al. [237] used both AE and vibration signals to diagnose the slow-speed bearings. Two fault diagnosis techniques, relevance vector machine and support vector machine, were used and the results indicated that AE signals demonstrate better performance than vibration signals. Elforjani et al. [238] conducted a fatigue life analysis to detect and locate the life-test defects via AE analysis. A 35 kN radial load is applied to the test bearing. The envelopes of the collected AE signals are analysed in order to detect the presence of the bearing defect frequencies. The results show that AE

analysis can be employed as a quality control tool for slow-speed bearing manufacturers. Žvokelj et al. [239] conducted a slewing bearing fatigue life experiment in order to detect incipient failures in the bearing. The test AE signals were collected under different working conditions including different axial loads (0, 240, 480) kN and rotation directions (left, right). Ensemble Empirical Mode Decomposition (EEMD) based multiscale Independent Component Analysis (ICA) is applied to extract weak fault signals and the envelope analysis is then utilized to diagnose the bearing fault type in the frequency domain. Aye et al. [240] combined the principal component analysis (PCA) and the exponentially weighted moving average (EWMA) method to process the AE signals of a slow-speed bearing. The proposed diagnostic tool can detect the bearing fault under the conditions of variable speeds and heavy loads.

Although the aforementioned investigations present many interesting results, they mainly focus on small-scale bearings in a sublimite laboratory environment. The laboratory tests often introduce seeded faults which may not perform well on large-scale and real-world wind turbines due to the complex failure modes. For our case, an industrial wind turbine blade bearing which has already served on a wind farm for over 15 years, is utilized. The defects in this test blade bearing are produced under real wind turbine working conditions instead of artificial defects or accelerated life-test defects, which is more accordant with the field situations. However, the main difficulties are as follows: 1) the fault signals are weak under slow rotation speed conditions; 2) the AE signal denoising is difficult when compared with vibration analysis. This is because the source of generation of AE signals has a wide frequency range including more noisy disturbances. Therefore, AE signal denoising has become a critical factor for blade bearing fault diagnosis.

For signal denoising, the raw AE signal of the wind turbine blade bearing has stochastic components including AE fault signals and periodic components including noise, so CMFD of large-scale wind turbine blade bearings benefits greatly in terms of efficiency if the periodic component can be eliminated. The characteristic of the periodic component is that it can produce a frequency spectrum with multiple equally spaced harmonics and modulation sidebands resulting in periodicities of the spectrum [241].

In the cepstrum domain (it is the spectrum of the frequency spectrum), these periodicities of the spectrum can be concentrated into families of impulses called “rahmonics” [242]. As a result, removal of the rahmonics or liftering can reduce the periodic component and denoise the raw AE signal. A case in point is where the rahmonics are removed. To solve this issue, cepstrum editing procedures (CEPs) are developed to separate impulsive type rahmonics from the cepstrum. The most widely used CEPs are the notch liftering (the notch filter in the cepstrum) and cepstrum pre-whitening. With regard to notch liftering, the operation consists of designing a series of notch lifters to set all corresponding rahmonics to zero in order to eliminate the periodic components [243]. However, for the AE analysis, the sources of generation of AE signals have a wide frequency range including different kinds of disturbances making the lifter design more complicated. The other cepstrum pre-whitening is far more radical when compared with notch liftering, which uses a low-pass liftering to set the cepstrum to zero value (except possibly at zero quefrency) [241]. This technique can remove all rahmonics, but some useful information is also eliminated. Consequently, the aforementioned CEPs may not be the ideal solutions for AE signal denoising. In order to extract weak fault signals as far as possible, this chapter proposes a discrete/random separation based cepstrum editing liftering (DRS-CEL) for AE signal denoising where DRS is used as the lifter in the cepstrum domain. The DRS method is firstly proposed by Antoni and Randall in [208] for noise cancellation in the time domain. It can achieve a filter to cancel periodic components from the raw signal. As a result, from the remaining denoised part, the fault signals become dominant. Since the rahmonics in the cepstrum domain also possess periodic properties, similar to the DRS filtering in the time domain, the rahmonics can also be removed via DRS in the cepstrum domain. Compared with the conventional CEPs, such as notch liftering or cepstrum pre-whitening, the DRS lifter is easier to implement and can achieve better denoising performance.

After the signal is denoised, the following step is to implement envelope analysis to demodulate the denoised signal and detect the presence of the bearing defect frequency generated by bearing faults. To achieve this goal, the morphological envelope

method is employed. It was first developed by Nikolaou et al. [214] for bearing vibration signal analysis. Later on, some scholars utilized it for different machinery fault diagnoses [244–246]. Different from the Hilbert envelope method, the morphological envelope method can construct an envelope by modifying the geometrical features of the signals in order to further filter the residual noise leaked from signal denoising step and accentuate the bearing defect frequency. Subsequently, the bearing defect frequency has become more dominant and is easier to distinguish. In this chapter, we integrate the DRS-CEL and morphological envelope analysis into a combined diagnostic framework which is validated by comparisons with other filtering methods and Hilbert envelope method. The diagnostic results indicate that the proposed framework offers a promising solution for wind farm applications [153].

8.2 Theoretical Background

8.2.1 Discrete/Random Separation based cepstrum editing liftering (DRS-CEL)

As mentioned in the introduction part, the raw AE signal of the wind turbine blade bearing has stochastic components including AE fault signals and periodic components including noise. Therefore, signal denoising can be carried out if the periodic components can be eliminated. In order to achieve this goal, a new development, published by Randall in [247], introduced a real cepstrum editing method, which can remove the periodic components in the cepstrum domain. The word “cepstrum” is derived by reversing the first four letters of “spectrum”, which justifies it is a spectrum of a frequency spectrum [248]. Furthermore, the words “quefrency”, “rahmonics” and “lifter” are also regularly used words which are from “frequency”, “harmonics” and “filter” to clarify that the operations refer to the cepstrum domain [248]. In particular, given a signal $x(n)$, $n = 1, \dots, 2N - 1$, the real cepstrum can be defined as follows:

$$C(n) = \text{Re}(\mathcal{F}^{-1}\{\ln[|\mathcal{F}(x(n))|]\}), n = 1, \dots, 2N - 1 \quad (8.1)$$

where the notation Re indicates the real part. $\mathcal{F}[\cdot]$ and $\mathcal{F}^{-1}[\cdot]$ correspond to the Discrete Fourier Transform (DFT) and Inverse Discrete Fourier Transform (IDFT) respectively. To denoise the AE signal, the DRS lifter is developed to separate rahmonics from the cepstrum. As can be seen in (8.1), the real cepstrum is the spectrum of the logarithm of the frequency spectrum, so it is even symmetry at the centre point N . Therefore, for the DRS liftering, we only use the left-hand side (LHS) real cepstrum

$$C_r(n) = C(n), n = 1, \dots, N \quad (8.2)$$

The real cepstrum can be expressed as a combination of the rahmonics and stochastic components including AE fault signals. The rahmonics, which are transformed from the equally spaced harmonics, have some periodic properties, so the LHS real cepstrum $C_r(n)$ can be expressed as below [207]:

$$C_r(n) = s(n) + p(n), n = 1, \dots, N \quad (8.3)$$

where $s(n)$ indicates a stochastic process including AE fault signals and $p(n)$ indicates a periodic process containing rahmonics components. $s(n)$ and $p(n)$ are uncorrelated with each other. From [249], the periodic process satisfies to be predicted from its previous values. More precisely, defining $\widehat{C}_r(n)$ as the predictor of $C_r(n)$ from a certain number of previous values $C_r(n - \Delta - i)$ with $i = 0, \dots, M - 1$ and Δ satisfies the condition $E[s(n)s(n - m)] = 0$ for all $|m| > \Delta$. The notation $E[\cdot]$ indicates the expectation operator. From [207], $\widehat{C}_r(n)$ is expressed as a linear regressor shown below:

$$\widehat{C}_r(n) = \sum_{i=0}^{M-1} h_i C_r(n - \Delta - i) \quad (8.4)$$

To estimate the quality of $\widehat{C}_r(n)$, the mean squared error σ_e^2 is utilized,

$$\begin{aligned} \sigma_e^2 &= E\{[\widehat{C}_r(n) - C_r(n)]^2\} \\ &= \frac{1}{N} \sum_{n=1}^N [\widehat{C}_r(n) - C_r(n)]^2 \end{aligned} \quad (8.5)$$

The following procedure is to determine the values of the coefficients h_i when the mean squared error σ_e^2 is minimized. Substituting (8.4) into (8.5), the equation is shown as

$$\sigma_e^2 = \frac{1}{N} \sum_{n=1}^N \left[\sum_{i=0}^{M-1} h_i C(n - \Delta - i) - C_r(n) \right]^2 \quad (8.6)$$

In order to find out the minimum σ_e^2 , the gradient of (8.6) is

$$\begin{aligned} \sum_{i=1}^{M-1} \frac{\partial(\sigma_e^2)}{\partial h_i} &= \frac{2}{N} \sum_{n=1}^N \left\{ \left[\sum_{i=0}^{M-1} h_i C_r(n - \Delta - i) - C_r(n) \right] \sum_{j=0}^{M-1} C_r(n - \Delta - j) \right\} \\ &= \frac{2}{N} \sum_{n=1}^N \left[\sum_{i=0}^{M-1} h_i r(n, i) - r(n) \right] \end{aligned} \quad (8.7)$$

where $r(n, i) = \sum_{j=0}^{M-1} C_r(n - \Delta - j) C_r(n - \Delta - i)$ and $r(n) = \sum_{j=0}^{M-1} C_r(n - \Delta - j) C_r(n)$. Then, the condition of minimum σ_e^2 is

$$\sum_{i=0}^{M-1} h_i r(n, i) - r(n) = 0 \quad (8.8)$$

where $n = 1, \dots, N$ and $i = 0, \dots, M-1$. The (8.8) is termed the Wiener-Hopf equation.

Antoni et al. [208] proposed a convenient method DRS which can solve (8.8) in the frequency domain. Specifically, after applying the discrete Fourier transform (DFT) to (8.8), the equation becomes to

$$\begin{aligned} \mathcal{F}[s(n)] &= R_1(f) = \mathcal{F} \left[\sum_{i=0}^{M-1} h_i r(n, i) \right] \\ &= \sum_{n=1}^N r(n, i) e^{-j\omega(n-i)} \sum_{i=0}^{M-1} h_i e^{-j\omega i} \\ &= R_2(f) H(f) \end{aligned} \quad (8.9)$$

where $\mathcal{F}[\cdot]$ represents the DFT. From (8.9), the Wiener-Hopf equation is transformed in the frequency domain and can be expressed by the product. Therefore, the filter

$H(f)$ can be solved directly based on the ratio between a current signal block $R_1(f)$ and a past signal block $R_2(f)$. Assuming $R_1(f)$ and $R_2(f)$ are expressed as

$$R_1(f) = \mathcal{F}[C_r(n - T)], T = 0, \dots, N - 1 \quad (8.10)$$

and

$$R_2(f) = \mathcal{F}[C_r(n - T - \Delta)], T = 0, \dots, N - 1 \quad (8.11)$$

where $\Delta > 0$.

Labelling $\hat{R}_M(f)$ and $\hat{R}_M^\Delta(f)$ are the estimators of $R_1(f)$ and $R_2(f)$ with the block length M ($M = 2N$ due to possible zero-padding), the estimator of $H(f)$ is [208]

$$\hat{H}(f) = \frac{\hat{R}_M^\Delta(f) \cdot \hat{R}_M(f)^*}{|\hat{R}_M^\Delta(f)|^2} \quad (8.12)$$

The M -long DRS lifter $\hat{H}(f)$ can be utilized to remove rahmonics from the real cepstrum $C_r(n)$. So, the DRS edited LHS real cepstrum can be derived as

$$C_{\text{LHS}}(n) = \mathcal{F}^{-1}[\hat{H}(f)] * C_r(n), n = 1, \dots, N \quad (8.13)$$

where the notation $*$ indicates the convolution operation. As the real cepstrum is even symmetry at the centre point N , the final edited real cepstrum is expressed as

$$C_{\text{edited}}(n) = \begin{cases} C_{\text{LHS}}(n) & n = 1, \dots, N \\ C_{\text{LHS}}(2N - n) & n = N + 1, \dots, 2N - 1 \end{cases} \quad (8.14)$$

Consequently, the final edited real spectrum can be combined with the original phase spectrum

$$\phi(\omega) = \arctan\left(\frac{\text{Im}(\mathcal{F}(x(n)))}{\text{Re}(\mathcal{F}(x(n)))}\right) \quad (8.15)$$

to generate a DRS-CEL denoised signal $x_D(n)$:

$$x_D(n) = \mathcal{F}^{-1}(e^{\text{Re}(\mathcal{F}(C_{\text{edited}}(n)))} \cdot e^{i\phi(\omega)}) \quad (8.16)$$

where $n = 1, \dots, 2N - 1$. The notation Re and Im represent real and imaginary parts, respectively.

8.2.2 Morphological closing envelope

The DRS-CEL method introduced in the previous subsection can denoise the raw AE signal and extract impulsive-type weak fault signals. The next step for blade bearing fault diagnosis is to calculate the repetition rate (this is also known as the bearing defect frequency) of these extracted fault signals. However, the fault signals are modulated by high-frequency harmonic components making the repetition rate unnoticeable in the frequency domain. To demodulate the denoised signal, morphological analysis is utilized in this chapter as it can accentuate the repetition rate as well as further filter the residual noise leaked from the DRS-CEL denoising [244]. The idea of morphological analysis is to extract the shape of a signal, by modifying it with another function called the structure element (SE). There are two basic morphological operations, dilation and erosion, which are defined as [245]

$$(x_D \oplus g)(n) = \max[x_D(n - \gamma) + g(\gamma)] \quad (8.17)$$

$$(x_D \ominus g)(n) = \min[x_D(n + \gamma) - g(\gamma)] \quad (8.18)$$

where the notations \oplus and \ominus indicates dilation and erosion respectively. x_D represents the DRS-CEL denoised signal with $n = 1, \dots, 2N - 1$; and $g(n)$ is the SE with $\gamma = 1, \dots, \Gamma$ and $\Gamma < 2N - 1$. Based on the dilation and erosion, we can derive the morphological closing envelope:

$$(x_D \bullet g)(n) = (x_D \oplus g \ominus g)(n) \quad (8.19)$$

where \bullet indicates the closing operator. To fully discuss the morphological closing envelope, we use an example to demonstrate its effectiveness. As can be seen, Fig.8.1(a) shows the DRS-CEL denoised signal and Fig.8.1(b) displays the conventional Hilbert envelope where the weak fault signals are still submerged by some noise, meaning that the repetition rate of the fault signals (or bearing defect frequency) may be insignificant in the frequency domain. To solve this issue, morphological closing envelope (see Fig.8.1(c)) is utilized where the residual noise can further be reduced and the shape of the envelope is very close to the DRS-CEL denoised signal. Finally, to diagnose the specific bearing fault type, $\mathcal{F}[(x_D \bullet g)(n)]$ is calculated to find the bearing defect frequency in the frequency domain.

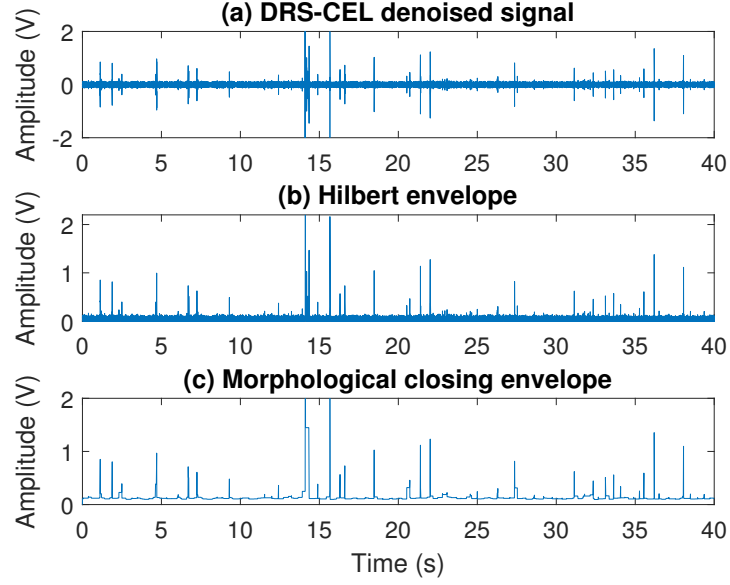


Fig. 8.1. (a) DRS-CEL denoised signal, and its different kinds of envelopes: (b) Hilbert envelope and (c) morphological closing envelope.

8.2.3 Summary of the diagnostic framework and parameter tuning

From the above, the diagnostic framework of the proposed method is shown in Fig.8.2. It can be seen, the procedure consists of two steps: the DRS-CEL denoising and morphological analysis. DRS-CEL produces a DRS lifter to separate rahmonics from the cepstrum so that the raw AE signals can be denoised. Thereafter, the morphological closing envelope is utilized to further filter the residual noise leaked from the DRS-CEL procedure and identify the bearing defect frequency.

With regard to DRS-CEL analysis, the time delay Δ and the lifter length M are two tunable parameters which are able to affect the filtering performance of the denoised signal. In order to determine these parameters, we choose the kurtosis criterion as the indicator to evaluate the DRS-CEL denoising performance. The high kurtosis indicates that the signal has a great deal of spikes. Finally, we draw a 3D plane based on the calculated parameters to determine the location of the largest kurtosis point. For example, as can be seen in Fig.8.3, the x-axis and y-axis indicate the time delay Δ and lifter length M respectively and z-axis presents the kurtosis value where the highest kurtosis is 202.8 at the time delay up to 1484 and the lifter length up to 28.

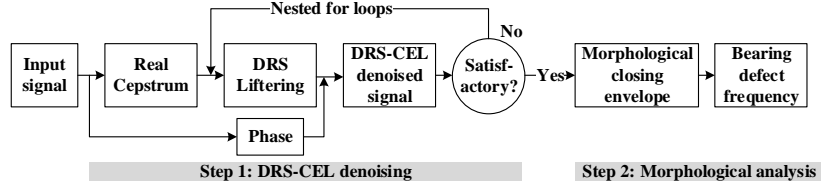


Fig. 8.2. The flowchart of the diagnostic framework.

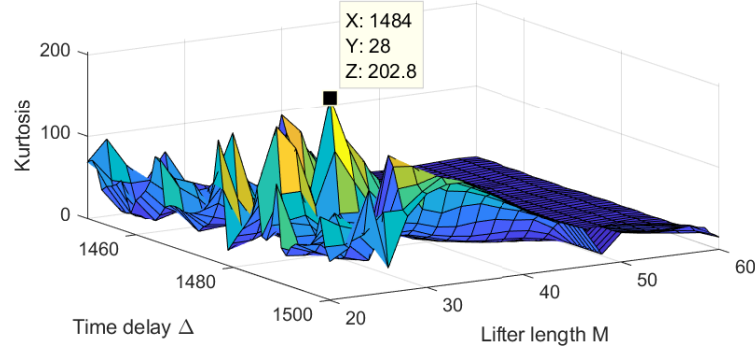


Fig. 8.3. 3D plot for kurtosis VS time delay Δ and lifter length M .

Therefore, we choose the time delay $\Delta = 1484$ and lifter length $M = 28$ for DRS-CEL denoising.

In respect of the morphological analysis, SE is the key factor which has a decisive effect on the diagnostic result. As presented in the recent studies [244–246], there are various kinds of SE designs; but for simplicity, we utilize flat SEs where the amplitudes are set to zero and only the length Γ needs to be tuned. As suggested from [245], a longer length of SE can extract a smaller number of impulsive-type fault signals so that the lower frequency components are accentuated. Instead, a shorter length of SE can detect more fault signals and the higher frequency components are enhanced. When tuning the SE, the extracted frequencies are compared with the theoretical defect frequency and the one producing the distinct frequency which coincides with the theoretical defect frequency will be utilized.

8.3 AE signal denoising

The experimental AE signals used as examples in this section come from an PK15I type AE sensor installed on the blade bearing outer ring surface. The blade bearing

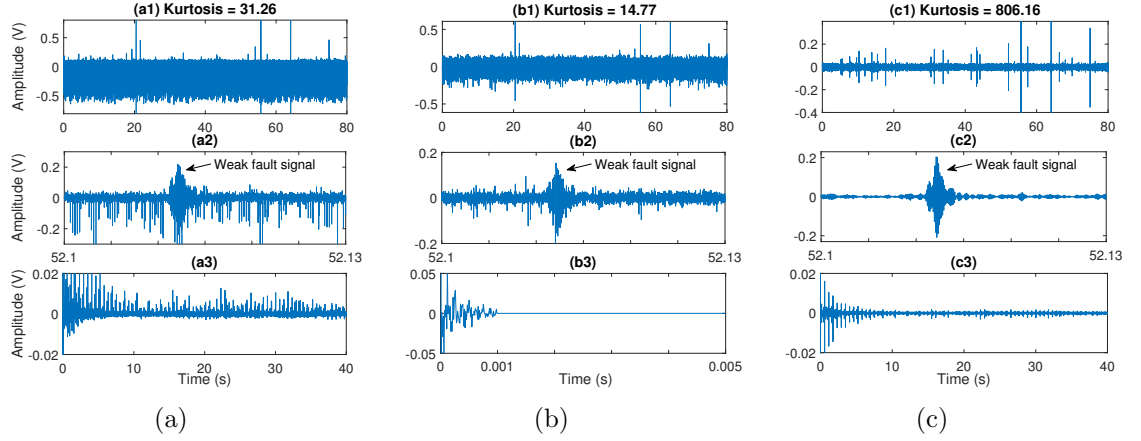


Fig. 8.4. Test 1, the comparisons of raw AE signal, low-pass edited signal and DRS-CEL denoised signal: (a1) raw AE signal at 1.11 r/min (a2) enlarged raw AE signal (a3) real cepstrum of the raw AE signal (b1) low-pass edited signal (b2) enlarged low-pass edited signal (c3) real cepstrum of the low-pass edited signal (c1) DRS-CEL denoised signal (c2) enlarged DRS-CEL denoised signal and (c3) real cepstrum of the DRS-CEL denoised signal

test rig is shown in Fig.4.3. Fig.8.4(a1) presents the first test where the raw AE signal is obtained by rotating the bearing at 1.11 r/min. The raw signal kurtosis is 31.26. If we zoom in the raw AE signal from 52.1 s to 52.13 s as shown in Fig.8.4(a2), the small fault signal can be seen which are masked by some unknown noisy disturbances. After analyzing its real cepstrum presented in Fig.8.4(a3), we can see that the cepstrum is dominated by multiple families of rahmonics generated from motor rotation, shaft rotation, gearbox tooth meshing, etc. Removing these rahmonics (or CEP) can denoise the raw signals and extract weak fault signals. One of the CEPs introduced in [242] is notch liftering which designs a series of notch lifters to set the corresponding rahmonics to zero. However, as for AE signal editing, the notch lifter design is complicated and very difficult to carry out. This is because the rahmonics are massive and distributed in the whole cepstrum with different amplitudes and quefrequencies. Another CEP is cepstrum pre-whitening which is to design a low-pass lifter to set the cepstrum to zero [241]. For example, in Fig.8.4(b3), we design a low-pass lifter with the cutoff quefreny 0.001 s, which can pass quefrequencies within 0.001 s and reject quefrequencies outside 0.001 s. After applying this lifter, the signal waveform in the time domain (see Fig.8.4(b2)) is smoothed. However, for the whole signal depicted in Fig.8.4(b1), the weak fault signals are still masked by heavy noise. Moreover, the kurtosis value decreases from 31.26 to 14.77 indicating that some useful information is eliminated by using the low-pass lifter. To address this problem, the proposed DRS-CEL is then

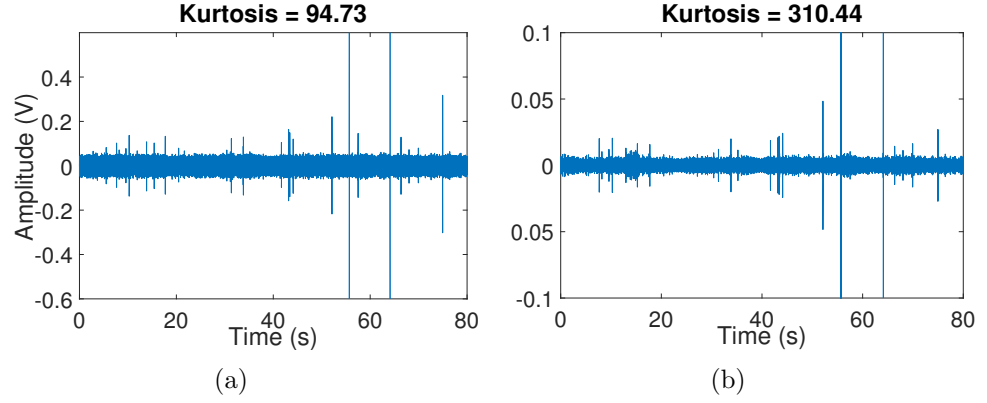


Fig. 8.5. Different denoised signals by using the (a) DRS method and (b) SK analysis.

utilized. Fig.8.4(c1) and (c2) show the filtered signals and its enlarged part. As can be seen, the weak fault signals are extracted and the whole signal waveform is smoothed. The kurtosis of the DRS-CEL filtered improves from 31.26 to 806.16. Fig.8.4(c3) shows the DRS edited cepstrum. Compared with Fig.8.4(a3), the amplitudes of the rahmonics depicted in Fig.8.4(c3) are reduced meaning that the corresponding periodic components are minimized.

To further demonstrate the priority of our proposed DRS-CEL denoising, two widely-used signal denoising methods, DRS [208] and the spectral kurtosis (SK) [206], are utilized for comparisons. The DRS method can produce a filter to cancel periodic components from the raw AE data, so some fault signals become dominant from the remaining denoised part. Fig.8.5(a) shows the DRS filtered signal. After carefully tuning the corresponding parameters of the DRS method, the signal kurtosis can reach to 94.72; but the denoising performance is inferior to the DRS-CEL denoising as shown in Fig.8.4(c1). In respect of the SK, Antoni introduced the fast kurtogram method which is able to detect fault signals in a narrow frequency band with the aim of maximizing the kurtosis of the denoised signal [206]. Fig.8.5(b) presents the band-pass filtered signal with the filter bandwidth [6250.0 Hz, 7812.5 Hz]. As can be seen, the kurtosis of the filtered signal improves to 310.44. However, only the large spikes are extracted and some small spikes are degraded.

In respect of Test 2, Fig.8.6(a) displays the raw AE signal where the bearing rotation speed is increased to 2.69 r/min. Firstly, we utilize DRS and SK to filter the raw signal, and the kurtosis improves to 88.45 and 519.94 respectively (see Fig.8.6(b) and

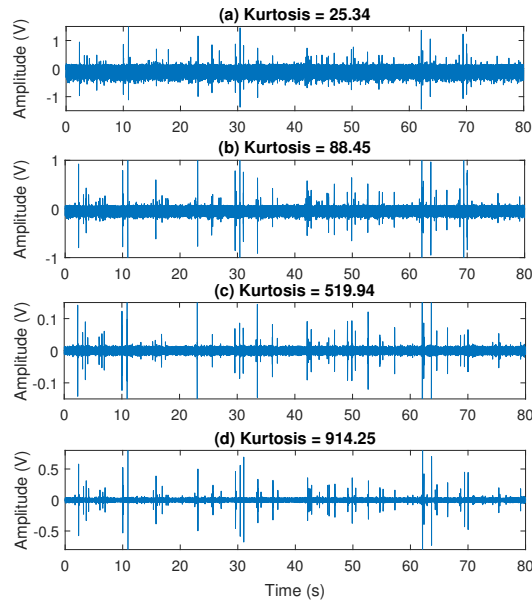


Fig. 8.6. Test 2: (a) raw AE signal at 2.69 r/min, (b) DRS denoised signal, (c) band-pass filtered signal by using the SK and (d) DRS-CEL denoised signal.

Table 8.1

AE HIT PARAMETERS OF TEST 1

	Raw signal	Low-pass lifter	DRS	SK analysis	DRS-CEL
RMS	0.041	0.028	0.015	0.021	0.009
ASL(dB)	-33.09	-33.60	-41.99	-44.12	-46.79
Energy	96.80	0.65	130.57	89.57	213.61
Counts	177	52	329	729	993

(c)). In order to further extract the weak fault signals and minimize the noise level, the new DRS-CEL is utilized. As can be seen in Fig.8.6(d), the fault signals are clearly demonstrated with small noise interferences and the kurtosis value increases to 914.25.

Up until this point, two experiments (Test 1 and Test 2) were conducted by using low-pass lifter, DRS, SK and DRS-CEL. In order to further compare the used methods, four AE hit parameters which are Root Mean Square (RMS), Average Signal Level (ASL), energy and counts, are presented in Table.8.1 and Table.8.2. RMS and ASL are the indicators to measure the continuously varying of AE signals or AE noise levels, and energy and counts can measure the extracted AE fault signals [250]. As can be seen in Table.8.1 and Table.8.2, the DRS-CEL method can produce the lowest RMS and ASL value indicating that DRS-CEL has better denoising performance. Another finding from these tables is that DRS-CEL outperforms other filtering methods that used for fault signal extraction. This is because DRS-CEL can produce the highest energy and counts.

Table 8.2

AE HIT PARAMETERS OF TEST 2

	Raw signal	Low-pass lifter	DRS	SK analysis	DRS-CEL
RMS	0.028	0.027	0.017	0.010	0.008
ASL(dB)	-31.44	-33.78	-36.64	-42.83	-43.44
Energy	732.76	3.12	823.93	596.62	873.98
Counts	1057	445	1363	2000	2671

8.4 Fault diagnosis

After filtering the raw AE signal, the next step is to apply morphological analysis to the denoised signals (Fig.8.4(c1) and Fig.8.6(d)) with the aim of diagnosing the blade bearing fault type. The characteristics of morphological analysis are that it can accentuate the defect frequencies and further filter the DRS-CEL denoised signal. Fig.8.7(a) and Fig.8.8(a) present the frequency spectrums of the morphological closing envelopes where the dominant frequencies are 0.575 Hz for 1.11 r/min and 1.378 Hz for 2.69 r/min.

The proposed diagnostic framework contains a signal denoising step (DRS-CEL denoising) and a fault diagnosis step (morphological analysis), so some comparisons with other frameworks are carried out in order to further evaluate the performance of our proposed methods. Fig.8.7(b) and Fig.8.8(b) present the combination of DRS-CEL and Hilbert envelope method. The bearing defect frequencies are extracted, but the spectrums present some unknown frequency components making the defect frequencies unnoticeable in the frequency domain. Fig.8.7(c) and Fig.8.8(c) show the frequency spectrum generated from the fast kurtogram method [206]. The defect frequencies are submerged by other frequency components and are very difficult to distinguish. Lastly, Fig.8.7(d) and Fig.8.8(d) plot the envelope spectrum of the raw AE signals (Fig.8.4(a1) and Fig.8.6(a)). As shown in these figures, the defect frequencies are non-obvious because of the complicated unknown frequency components.

The following equation is utilized to determine the defect frequency matching error (DFMR) which is an indicator to identify the bearing fault type.

$$\text{Error} = (|f_{\text{dominant}} - f_{\text{defect}}| / f_{\text{defect}}) \times 100\% \quad (8.20)$$

where f_{dominant} indicates the dominant frequencies and f_{defect} represents the theoretical

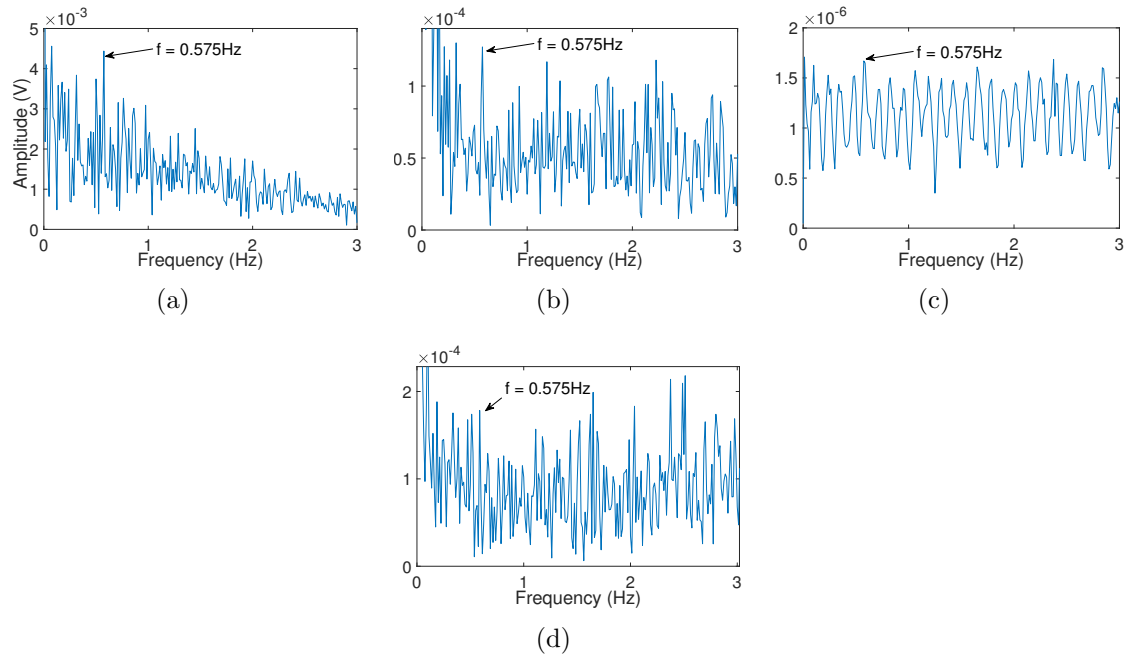


Fig. 8.7. Test 1 at 1.11 r/min, frequency spectrum process by (a) DRC-CEL/morphological closing envelope, (b) DRC-CEL/Hilbert envelope analysis (c) fast kurtogram analysis and (d) raw signal envelope spectrum.

Table 8.3

DEFECT FREQUENCIES MATCHING ERROR

Test	r/min	Inner matching error	Outer matching error	Ball matching error
Test 1	1.11	0.14%	7.34%	236.06%
Test 2	2.69	0.97%	6.15%	232.45%
Average		0.56%	6.75%	234.26%

defect frequencies calculated using (4.1)-(4.3). As can be seen, DFMR is the ratio between the theoretical defect frequency and the identified dominant frequency. The small DFMR indicates the high probability of the corresponding bearing fault type. Table 8.3 lists the diagnostic results reflecting that the fault is highly possible in the inner raceway with the lowest average DFMR of 0.56%.

8.5 Conclusion

The main goal of this chapter was to demonstrate the applicability of acoustic emission (AE) analysis in diagnosing the naturally damaged industrial and slow-speed blade bearing. To extract weak fault signals, a novel discrete/random separation based cepstrum editing liftering (DRS-CEL) method was proposed where the rahmonics in the

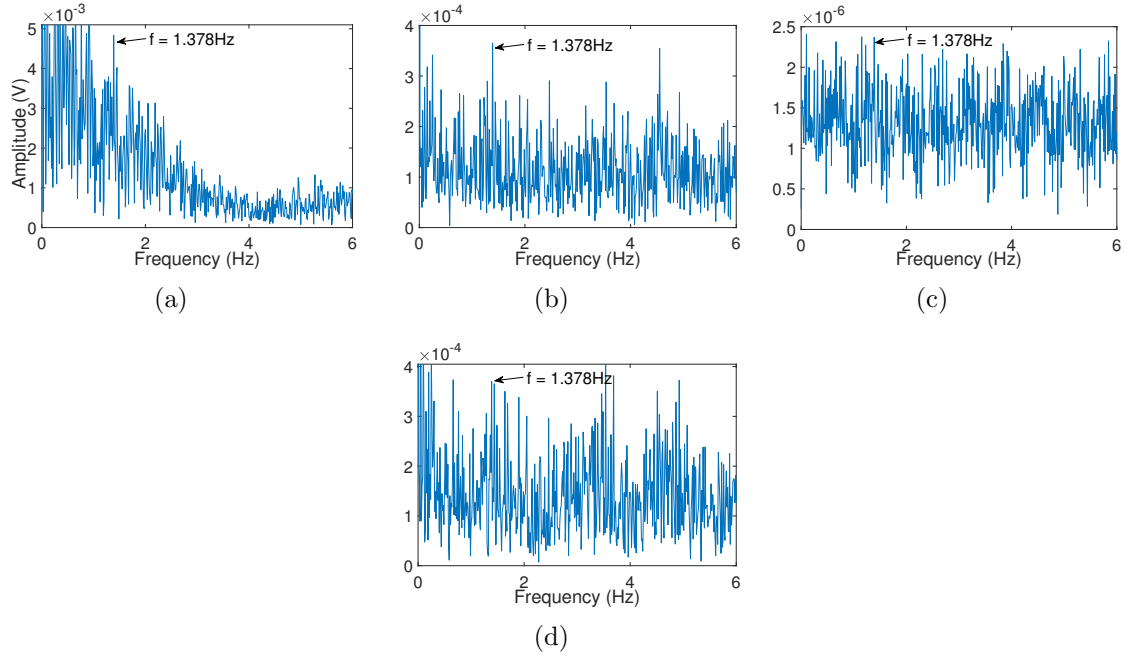


Fig. 8.8. Test 2 at 2.69 r/min, frequency spectrum process by (a) DRC-CEL/morphological closing envelope, (b) DRC-CEL/Hilbert envelope analysis and (c) fast kurtogram analysis and (d) raw AE signal envelope spectrum.

cepstrum domain were removed via DRS approach. Compared with the conventional cepstrum editing procedure (CEP), such as notching liftering and low-pass liftering, our method offers high denoising performance and is relatively easy to implement. Thereafter, the morphological analysis was utilized to further denoise the residual noise and diagnose the bearing fault type in the frequency domain. The effectiveness and accuracy of the proposed diagnostic framework were validated by comparisons with other methods and related studies.

Chapter 9

Conclusions and Future Works

9.1 Introduction

This chapter summaries the general findings on blade bearing fault diagnosis. Furthermore, some interesting topics as well as the research directions for blade bearing fault detections are suggested for future works.

9.2 Conclusions and Comparisons

Blade bearings are vital components for wind turbines which can achieve blade pitch processes, perform aerodynamic braking and transmit blade loads into the hub. They work in a hash environment under slow speed (less than 5 r/min) with limited angles (within 100°). Blade bearing failure can result in lost control of blades, and further reduce energy production. However, the research on blade bearing CMFD is still in an initial stage. This is because the special working mechanism of blade bearings gives rise to several challenges, which are summarized as follows. 1) The rotation speeds of blade bearings are very slow meaning that fault signals are very weak due to low kinetic energy and are also masked by noisy disturbances. 2) The effective collected signals is very limited because blade bearings swing in small angles. 3) The disturbances from the blade flapping and dynamic wind loads can cause fluctuating rotation speeds.

In order to solve the problems mentioned above, some novel methods were proposed. The main contributions of this thesis are listed as follows:

- This thesis have systematically and comprehensively reviewed current CMFD methods of wind turbine bearings in Chapters 2 and 3, which provides a references for scholars to better develop more reliable and cost-effective diagnostic methods.
- An industry-scale and slow-speed wind turbine blade bearing test-rig and in-situ fault detection tools including vibration and AE measurements are developed in Chapter 4.
- A novel method called empirical wavelet thresholding is proposed in Chapter 5. It is easy to use and can maximally minimize the heavy noise. Nonetheless, it can only be used under constant speed conditions and some weak fault signals will be eliminated which may affect the accuracy of the diagnostic results.
- A new method iterative nonlinear filter (INF) is proposed in Chapter 6 which can iteratively and gradually filter the raw vibration signals by extracting the fault signals and canceling out the periodic noise. The advantages of this method are that it has low computation cost and can keep the weak fault signals. However, the parameter tuning of INF is complicated and it can only be utilized under constant speed conditions. If the bearing rotates at constant and slow speeds, INF can be used for fault detection.
- To diagnose the blade bearing under time-varying speed conditions, a new AI method Bayesian Augmented Lagrangian (BAL) is used in Chapter 6. The advantages of this method are that the dictionary design is simplified by using a nonlinear autoregressive model but without sacrificing the filtering performance. The BAL method can learn the built model for noise reduction. However, the parameter tuning for this method is complicated. If the bearing rotates at fluctuation speeds, BAL can be used for CMFD.

- To use AE analysis for blade bearing fault diagnosis, a novel cepstrum editing method, discrete/random separation based cepstrum editing liftering (DRS-CEL), is proposed in Chapter 8 with the aim of filtering the raw AE signals. Compared with the conventional cepstrum editing method, DRS-CEL offers high denoising performance. However, the computation cost of DRS-CEL is high and the parameter tuning is complicated. DRS-CEL can be used to process the data under strong noise conditions.

In summary, this thesis for the first time proposed four novel methods (empirical wavelet thresholding, INF, BAL and DRS-CEL) for blade bearing fault diagnosis. A comparison of the proposed methods is summarized in Table.9.1. According to different situations and applications, different methods can be selected.

9.3 Future Works and Interesting topics

To date, my research has diagnosed one wind turbine blade bearing under different mechanical working conditions. In future research activities, the following problems and research activities could be considered

1. The research has only diagnosed one blade bearing. In the future, more blade bearings with different failure modes can be tested to validate our proposed methods.
2. As can be seen in Fig. 4.2, the normal operations of blade bearings include the starts, constant rotation, stops and direction changes. To diagnose blade bearings, my solution is to eliminate starts and stops, and only use the constant speed parts. As a result, some useful information inside the starts and stops will be eliminated. The new methods may be proposed to utilize the whole useful information.
3. For the fault characteristics analysis, the envelope methods are often implemented which can diagnose the bearing fault type in the frequency domain or

Table 9.1
Comparisons of different proposed methods.

Method	Advantages	Disadvantages	Experiments
EWT* (Chapter 5)	Low computational cost	Hard to determine the boundaries	Vibration analysis under constant slow speed conditions
	Easy to use	Some fault signals will be eliminated	
INF (Chapter 6)	High filtering performance	Parameter tuning is complicated	Vibration analysis under slow speed and limited angle conditions
	Fault signals can be retained		
BAL (Chapter 7)	Low computational cost	Parameter tuning is complicated	Vibration analysis under time-vary low speed and heavy load conditions
	High filtering performance		
	Dictionary design is easy		
DRS-CEL (Chapter 8)	High filtering performance	High computational cost	AE analysis under constant slow speed conditions
		Parameter tuning is complicated	

*empirical wavelet thresholding

order domain. These processes often need the speed information as a reference, and we must assemble tachometers to the test-rig with the aim of collecting speed informations. However, for wind farms, the assembled tachometers will increase costs. To solve this issue, the tacholess methods can be developed for blade bearing fault detections.

4. The developed diagnostic frameworks in this thesis can diagnose the bearing fault type (inner race fault, outer race fault and ball fault), but they cannot diagnose the fault severity and locate the fault place. In the future, new methods may be developed to solve these problems.
5. There is a great potential for the proposed methods to be applied to other rotation machines with similar noise disturbances and dynamic heavy load conditions.

Bibliography

- [1] R. S. Amano, “Review of wind turbine research in 21st century,” *Journal of Energy Resources Technology*, vol. 139, no. 5, p. 050801, 2017.
- [2] *Global wind report 2019*. Global Wind Energy Council, 2017.
- [3] L. Chen, Y. Zhang, and X. Xia, “Contact stress and deformation of blade bearing in wind turbine,” in *2010 International Conference on Measuring Technology and Mechatronics Automation*, vol. 1, March 2010, pp. 833–836.
- [4] M. H. Larsen, A. V. Nielsen, and S. F. Poulsen, “Pitch bearing for wind turbine rotor blades,” Dec. 4 2012, US Patent 8,322,928.
- [5] “Components and systems for wind turbines large diameter bearings, gearboxes, electric motors, and hydraulic cylinders - all from one source,” Liebherr, Tech. Rep.
- [6] J. Wang, Y. Peng, and W. Qiao, “Current-aided order tracking of vibration signals for bearing fault diagnosis of direct-drive wind turbines,” *IEEE Transactions on Industrial Electronics*, vol. 63, no. 10, pp. 6336–6346, Oct 2016.
- [7] L. Zhang, Z. Q. Lang, and M. Papaelias, “Generalized transmissibility damage indicator with application to wind turbine component condition monitoring,” *IEEE Transactions on Industrial Electronics*, vol. 63, no. 10, pp. 6347–6359, Oct 2016.
- [8] J. W. Han, J. S. Nam, Y. J. Park, G. H. Lee, and Y. Y. Nam, “An experimental study on the performance and fatigue life of pitch bearing for wind turbine,”

- Journal of Mechanical Science and Technology*, vol. 29, no. 5, pp. 1963–1971, 2015.
- [9] Y. Wang and Q. Yuan, “Static load-carrying capacity and fatigue life of a double row pitch bearing with radial interference,” *Proceedings of the Institution of Mechanical Engineers, Part C: Journal of Mechanical Engineering Science*, vol. 228, no. 2, pp. 307–316, 2014.
- [10] M. N. Kotzalas and G. L. Doll, “Tribological advancements for reliable wind turbine performance,” *Philosophical Transactions of the Royal Society of London A: Mathematical, Physical and Engineering Sciences*, vol. 368, no. 1929, pp. 4829–4850, 2010.
- [11] H. Polinder, F. F. A. van der Pijl, G. . de Vilder, and P. J. Tavner, “Comparison of direct-drive and geared generator concepts for wind turbines,” *IEEE Transactions on Energy Conversion*, vol. 21, no. 3, pp. 725–733, Sep. 2006.
- [12] Z. Liu and L. Zhang, “A review of failure modes, condition monitoring and fault diagnosis methods for large-scale wind turbine bearings,” *Measurement*, vol. 149, p. 107002, 2020.
- [13] “Extending bearing life in wind turbine mainshafts,” <http://www.power-eng.com/articles/print/volume-120/issue-8/features/extending-bearing-life-in-wind-turbine-mainshafts.html>, Aug. 2017 [accessed 31 December 2017].
- [14] F. Oyague, “Gearbox modeling and load simulation of a baseline 750-kW wind turbine using state-of-the-art simulation codes,” National Renewable Energy Laboratory (NREL), Golden, CO., Tech. Rep., 2009.
- [15] S. Sheng, “Report on wind turbine subsystem reliability-a survey of various databases,” National Renewable Energy Laboratory (NREL), Golden, CO., Tech. Rep., 2013.
- [16] L. Sethuraman, Y. Guo, and S. Sheng, “Main bearing dynamics in three-point suspension drivetrains for wind turbines,” National Renewable Energy Laboratory (NREL), Golden, CO., Tech. Rep., 2015.

- [17] *Bearing solutions and services for wind turbine gearboxes.* Schaeffler, 2010.
- [18] M. Paolone, F. Napolitano, A. Borghetti, C. Nucci, M. Marzinotto, F. Fiamingo, C. Mazzetti, and H. Dellago, “Models of wind-turbine main shaft bearings for the development of specific lightning protection systems,” in *2007 IEEE Lausanne Power Tech.* IEEE, 2007, pp. 783–789.
- [19] M. Whittle, “Wind turbine generator reliability: an exploration of the root causes of generator bearing failures,” Ph.D. dissertation, Durham University, 2013.
- [20] L. Ionescu and T. Pontius, “Main shaft support for wind turbine with a fixed and floating bearing configuration,” The Timkin Company, Tech. Rep., 2009.
- [21] S. Yagi and N. Ninoyu, “Technical trends in wind turbine bearings,” *Technical Review*, vol. 76, pp. 113–120, 2008.
- [22] “Bearing solutions and service for wind turbines,” Schaeffler, Schaeffler Technologies GmbH & Co. KG, Tech. Rep., 2014.
- [23] Y. Wang and Q. Yuan, “Contact force distribution and static load-carrying capacity of large size double row four-point contact ball bearing,” *Defence Technology*, vol. 9, no. 4, pp. 229–236, 2013.
- [24] “Bearing solutions and service for wind turbines,” Schaeffler, Tech. Rep., 2014.
- [25] M. H. Larsen, A. V. Nielsen, and S. F. Poulsen, “Pitch bearing for wind turbine rotor blades,” Dec. 4 2012, US Patent 8,322,928.
- [26] T. Harris, J. Rumbarger, and C. P. Butterfield, “Wind turbine design guideline DG03: yaw and pitch rolling bearing life,” National Renewable Energy Laboratory (NREL), Golden, CO., Tech. Rep., 2009.
- [27] M. Kim and P. Dalhoff, “Yaw systems for wind turbines—overview of concepts, current challenges and design methods,” in *Journal of Physics: Conference Series*, vol. 524, no. 1. IOP Publishing, 2014, p. 012086.
- [28] R. Arsenault, *Treatise on materials science and technology. Volume VI. Plastic deformation of materials.* Academic Press, Inc., New York, 1975.

- [29] T. Zhang, W. Xu, and M. Zhao, “The role of plastic deformation of rough surfaces in the size-dependent hardness,” *Acta materialia*, vol. 52, no. 1, pp. 57–68, 2004.
- [30] *Rolling bearings - Damage and failures - Terms, characteristics and causes*. ISO 15243:2004(E), 2004.
- [31] C. Radu, “The most common causes of bearing failure and the importance of bearing lubrication,” *RKB Technical Review-February*, pp. 1–7, 2010.
- [32] J. I. Taylor, “Identification of bearing defects by spectral analysis,” *Journal of Mechanical design*, vol. 102, no. 2, pp. 199–204, 1980.
- [33] Z. He, J. Zhang, W. Xie, Z. Li, and G. Zhang, “Misalignment analysis of journal bearing influenced by asymmetric deflection, based on a simple stepped shaft model,” *Journal of Zhejiang University-Science A*, vol. 13, no. 9, pp. 647–664, 2012.
- [34] M. Lahmar, D. Frihi, and D. Nicolas, “The effect of misalignment on performance characteristics of engine main crankshaft bearings,” *European Journal of Mechanics-A/Solids*, vol. 21, no. 4, pp. 703–714, 2002.
- [35] M. Whittle, W. Shin, J. Trevelyan, and J. Wu, “A parametric study of the effect of generator misalignment on bearing fatigue life in wind turbines,” in *2011 European Wind Energy Conference and Exhibition (EWEC)*, 01 2011, pp. 24–27.
- [36] R. Widner and W. Littmann, “Bearing damage analysis,” in *Proceeding of the 20th Meeting of the Mechanical Failures Prevention Group*. US Department of Commerce Gaithersburg, MD, 1976, pp. 67–83.
- [37] “Bearing failure: Causes and cures,” Barden Precision Bearings, Tech. Rep., 1992.
- [38] P. J. Blau, L. R. Walker, H. Xu, R. J. Parten, J. Qu, and T. Geer, “Wear analysis of wind turbine gearbox bearings,” Oak Ridge National Laboratory (ORNL), Tech. Rep., 2010.

- [39] “Care and maintenance of bearings,” NTN corporation, Tech. Rep., 2017.
- [40] “Bearing failure prevention guide,” The Torrington Company, Torrington Ingersoll Rand, Tech. Rep., 2017.
- [41] “Rolling bearing damage symptoms causes remedies,” FAG Schaeffler Group Aerospace, Tech. Rep., 2011.
- [42] X. Ai, “Effect of debris contamination on the fatigue life of roller bearings,” *Proceedings of the Institution of Mechanical Engineers, Part J: Journal of Engineering Tribology*, vol. 215, no. 6, pp. 563–575, 2001.
- [43] P. A. Carneiro, G. A. Umbuzeiro, D. P. Oliveira, and M. V. B. Zanoni, “Assessment of water contamination caused by a mutagenic textile effluent/dyehouse effluent bearing disperse dyes,” *Journal of Hazardous Materials*, vol. 174, no. 1, pp. 694–699, 2010.
- [44] Y. P. Raizer and J. E. Allen, *Gas discharge physics*. Springer Berlin, 1997, vol. 2.
- [45] F. Simpson and W. Crump, “Effects of electric currents on the life of rolling contact bearings,” in *Proc. Lubrication and Wear Convention Bournemouth*, 1963, pp. 296–304.
- [46] S. Raadnui and S. Kleesuwan, “Electrical pitting of grease-lubricated rolling and sliding bearings: a comparative study,” in *Journal of Physics: Conference Series*, vol. 364, no. 1. IOP Publishing, 2012, p. 012041.
- [47] M. A. Maleque and M. S. Salit, *Materials selection and design*. Springer, 2013.
- [48] M. Evans, “An updated review: white etching cracks (WECs) and axial cracks in wind turbine gearbox bearings,” *Materials Science and Technology*, vol. 32, no. 11, pp. 1133–1169, 2016.
- [49] T. Bruce, E. Rounding, H. Long, and R. Dwyer-Joyce, “Characterisation of white etching crack damage in wind turbine gearbox bearings,” *Wear*, vol. 338, pp. 164–177, 2015.

- [50] A. R. Du Crehu, “Tribological analysis of white etching crack (WEC) failures in rolling element bearings,” Ph.D. dissertation, INSA de Lyon, 2014.
- [51] M. Evans, A. Richardson, L. Wang, and R. Wood, “Serial sectioning investigation of butterfly and white etching crack (WEC) formation in wind turbine gearbox bearings,” *Wear*, vol. 302, no. 1, pp. 1573–1582, 2013.
- [52] K. Mori, N. Kasashima, T. Yoshioka, and Y. Ueno, “Prediction of spalling on a ball bearing by applying the discrete wavelet transform to vibration signals,” *Wear*, vol. 195, no. 1-2, pp. 162–168, 1996.
- [53] W. H. Detweiler, “Common causes and cures for roller bearing overheating,” SKF USA Inc, Tech. Rep., 2011.
- [54] “Example type B report wind turbine blade pitch bearing analysis,” JAD analysis, Tech. Rep., 2015.
- [55] I. Kovaříková, B. Szewczykova, P. Blaškoviš, E. Hodúlová, and E. Lechovič, “Study and characteristic of abrasive wear mechanisms,” *Materials Science and Technology*, pp. 1335–9053, 2009.
- [56] F. Massi, J. Rocchi, A. Culla, and Y. Berthier, “Coupling system dynamics and contact behaviour: Modelling bearings subjected to environmental induced vibrations and ‘false brinelling’ degradation,” *Mechanical Systems and Signal Processing*, vol. 24, no. 4, pp. 1068–1080, 2010.
- [57] M. Phaner-Goutorbe, C. Barthou, L. Porte, and B. Vannes, “Scanning tunneling microscopy study of wear induced by false brinelling on rolling bearings,” *Applied surface science*, vol. 108, no. 1, pp. 45–51, 1997.
- [58] R. L. Norton, *Cam design and manufacturing handbook*. Industrial Press Inc., 2009.
- [59] C. M. Pooley and D. Tabor, “Friction and molecular structure: the behaviour of some thermoplastics,” *Proceedings of the Royal Society of London A: Mathematical, Physical and Engineering Sciences*, vol. 329, no. 1578, pp. 251–274, 1972.

- [60] G. Y. Yampolski, I. Kragelskii, and I. Yushakov, “Abrasive wear of rolling bearings,” *Tribology International*, vol. 14, no. 3, pp. 137–138, 1981.
- [61] R. Nilsson, R. S. Dwyer-Joyce, and U. Olofsson, “Abrasive wear of rolling bearings by lubricant borne particles,” *Proceedings of the Institution of Mechanical Engineers, Part J: Journal of Engineering Tribology*, vol. 220, no. 5, pp. 429–439, 2006.
- [62] A. Begelinger and A. De Gee, “Abrasive wear of bearing materials—a comparison of test methods,” *Wear*, vol. 101, no. 2, pp. 141–154, 1985.
- [63] A. Greco, S. Sheng, J. Keller, and A. Erdemir, “Material wear and fatigue in wind turbine systems,” *Wear*, vol. 302, no. 1, pp. 1583–1591, 2013.
- [64] A. Vencl, V. Gašić, and B. Stojanović, “Fault tree analysis of most common rolling bearing tribological failures,” in *IOP Conference Series: Materials Science and Engineering*, vol. 174, no. 1. IOP Publishing, 2017, p. 012048.
- [65] S. Sheng, M. McDade, and R. Errichello, *Wind Turbine Gearbox Failure Modes: A Brief*. National Renewable Energy Laboratory (NREL), 2011.
- [66] J. K. Toyoda, “Koyo training manual,” Tech. Rep., 2013.
- [67] U. S. Abdulhussain, E. A. Elfaki, and I. A. M. Ali, “Causes and remedies of bearing failure in sudanese industry,” *Journal of Science and Technology*, vol. 8, no. 1, pp. 0–0, 2007.
- [68] W. Qiao and D. Lu, “A survey on wind turbine condition monitoring and fault diagnosis—part I: Components and subsystems,” *IEEE Transactions on Industrial Electronics*, vol. 62, no. 10, pp. 6536–6545, 2015.
- [69] J. Smith, “Vibration monitoring of bearings at low speeds,” *Tribology International*, vol. 15, no. 3, pp. 139–144, 1982.
- [70] B. Lent, “Simple steps to selecting the right accelerometer,” <http://www.sensormag.com/components/simple-steps-to-selecting-right-accelerometer>, Aug. 2017 [accessed 31 December 2017].

- [71] “Acoustic emission testing,” https://www.nde-ed.org/EducationResources/CommunityCollege/Other%20Methods/AE/AE_Equipment.php, Aug. 2017 [accessed 31 December 2017].
- [72] J. Sun, R. Wood, L. Wang, I. Care, and H. Powrie, “Wear monitoring of bearing steel using electrostatic and acoustic emission techniques,” *Wear*, vol. 259, no. 7, pp. 1482–1489, 2005.
- [73] O. Tasbaz, R. Wood, M. Browne, H. Powrie, and G. Denuault, “Electrostatic monitoring of oil lubricated sliding point contacts for early detection of scuffing,” *Wear*, vol. 230, no. 1, pp. 86–97, 1999.
- [74] R. Dwyer Joyce, “Predicting the abrasive wear of ball bearings by lubricant debris,” *Wear*, vol. 233, pp. 692–701, 1999.
- [75] M. Whittle, “Wind turbine generator reliability: an exploration of the root causes of generator bearing failures,” Ph.D. dissertation, Durham University, 2013.
- [76] H. D. M. de Azevedo, A. M. Araújo, and N. Bouchonneau, “A review of wind turbine bearing condition monitoring: State-of-the-art and challenges,” *Renewable and Sustainable Energy Reviews*, vol. 56, pp. 368–379, 2016.
- [77] S. Costinas, I. Diaconescu, and I. Fagarasanu, “Wind power plant condition monitoring,” in *Proceedings of the 3rd WSEAS International Conference on Energy Planning, Energy Saving, Environmental Education (EPESE’09), Canary Islands, Spain*, 2009, pp. 1–3.
- [78] M. Regula, A. Otcenasova, M. Roch, R. Bodnar, and M. Repak, “SCADA system with power quality monitoring in smart grid model,” in *2016 IEEE 16th International Conference on Environment and Electrical Engineering (EEEIC)*. IEEE, 2016, pp. 1–5.
- [79] Z. Liu and L. Zhang, “Naturally damaged wind turbine blade bearing fault detection using novel iterative nonlinear filter and morphological analysis,” *IEEE Transactions on Industrial Electronics*, pp. 1–1, 2019.

- [80] B. Corley, J. Carroll, and A. McDonald, “Thermal modelling of a small wind turbine gearbox for condition monitoring,” *The Journal of Engineering*, vol. 2019, no. 18, pp. 5335–5339, 2019.
- [81] X. An, D. Jiang, J. Chen, and C. Liu, “Application of the intrinsic time-scale decomposition method to fault diagnosis of wind turbine bearing,” *Journal of Vibration and Control*, vol. 18, no. 2, pp. 240–245, 2012.
- [82] W. Xin, Y. Liu, Y. He, and B. Su, “Amplitude envelope analysis for feature extraction of direct-driven wind turbine bearing failure,” in *2012 10th World Congress on Intelligent Control and Automation (WCICA)*. IEEE, 2012, pp. 3173–3176.
- [83] Z. Pan, S. Liang, Y. Liu, and P. Liang, “Spectral correlation feature analysis for rolling bearing fault of wind turbine generator,” *International Conference on Renewable Power Generation (RPG 2015)*, pp. 1–5, 2015.
- [84] L. Zhang, Z. Q. Lang, and M. Papaelias, “Generalized transmissibility damage indicator with application to wind turbine component condition monitoring,” *IEEE Transactions on Industrial Electronics*, vol. 63, no. 10, pp. 6347–6359, 2016.
- [85] M. K. Bodla, S. M. Malik, M. T. Rasheed, M. Numan, M. Z. Ali, and J. B. Brima, “Logistic regression and feature extraction based fault diagnosis of main bearing of wind turbines,” in *2016 IEEE 11th Conference on Industrial Electronics and Applications (ICIEA)*. IEEE, 2016, pp. 1628–1633.
- [86] C. Chen, X. Sun, Q. Gu, B. Zhou, and Y. Gu, “Wavelet-based multifractal analysis of large scale wind turbine main bearing,” *Journal of Renewable and Sustainable Energy*, vol. 5, no. 1, p. 013102, 2013.
- [87] A. Purarjomandlangrudi, G. Nourbakhsh, H. Ghaemmaghmi, and A. Tan, “Application of anomaly technique in wind turbine bearing fault detection,” in *IECON 2014 - 40th Annual Conference of the IEEE Industrial Electronics Society*, Oct 2014, pp. 1984–1988.

- [88] L. Zhang and Z. Lang, “Wavelet energy transmissibility function and its application to wind turbine bearing condition monitoring,” *IEEE Transactions on Sustainable Energy*, vol. 9, no. 4, pp. 1833–1843, Oct 2018.
- [89] T. Han, Q. Liu, L. Zhang, and A. Tan, “Fault feature extraction of low speed roller bearing based on teager energy operator and ceemd,” *Measurement*, vol. 138, pp. 400–408, 2019.
- [90] X. Gong, W. Qiao, and W. Zhou, “Incipient bearing fault detection via wind generator stator current and wavelet filter,” in *IECON 2010-36th Annual Conference on IEEE Industrial Electronics Society*. IEEE, 2010, pp. 2615–2620.
- [91] X. Gong and W. Qiao, “Bearing fault detection for direct-drive wind turbines via stator current spectrum analysis,” in *2011 IEEE Energy Conversion Congress and Exposition (ECCE)*. IEEE, 2011, pp. 313–318.
- [92] W. Qiao and X. Gong, “Current-based online bearing fault diagnosis for direct-drive wind turbines via spectrum analysis and impulse detection,” in *2012 IEEE Power Electronics and Machines in Wind Applications (PEMWA)*. IEEE, 2012, pp. 1–6.
- [93] X. Gong, “Bearing fault diagnosis for direct-drive wind turbines via current-demodulated signals,” *IEEE Transactions on Industrial Electronics*, vol. 60, no. 8, pp. 3419–3428, 2013.
- [94] J. Wang, Y. Peng, W. Qiao, and J. L. Hudgins, “Bearing fault diagnosis of direct-drive wind turbines using multiscale filtering spectrum,” *IEEE Transactions on Industry Applications*, vol. 53, no. 3, pp. 3029–3038, 2017.
- [95] J. Wang, Y. Peng, and W. Qiao, “Current-aided order tracking of vibration signals for bearing fault diagnosis of direct-drive wind turbines,” *IEEE Transactions on Industrial Electronics*, vol. 63, no. 10, pp. 6336–6346, 2016.
- [96] W. Wang, “Autoregressive model-based diagnostics for gears and bearings,” *Insight-Non-Destructive Testing and Condition Monitoring*, vol. 50, no. 8, pp. 414–418, 2008.

- [97] C. Peeters, P. Guillaume, and J. Helsen, “Vibration-based bearing fault detection for operations and maintenance cost reduction in wind energy,” *Renewable Energy*, vol. 116, pp. 74–87, 2018.
- [98] I. Antoniadou, T. P. Howard, R. Dwyer Joyce, M. B. Marshall, J. Naumann, N. Dervilis, and K. Worden, “Envelope analysis using the teager-kaiser energy operator for condition monitoring of a wind turbine bearing,” *Applied Mechanics & Materials*, vol. 564, pp. 170–175, 2014.
- [99] N. Sawalhi, R. B. Randall, and D. Forrester, “Separation and enhancement of gear and bearing signals for the diagnosis of wind turbine transmission systems,” *Wind Energy*, vol. 17, no. 5, pp. 729–743, 2014.
- [100] J. Xu, J. Zhang, T. Chen, and R. H. Liu, “A planet bearing fault case of wind turbine gearbox,” *Advanced Materials Research*, vol. 953, pp. 472–477, 2014.
- [101] S. Jain, P. Whiteley, and H. Hunt, “Detection of planet bearing faults in wind turbine gearboxes,” in *Proceedings of International Conference on Noise and Vibration Engineering (ISMA’12)/International Conference on Uncertainty in Structural Dynamics (USD’12)*, 2012, pp. 4351–4362.
- [102] S. Shanbr, F. Elasha, M. Elforjani, and J. Teixeira, “Detection of natural crack in wind turbine gearbox,” *Renewable Energy*, vol. 118, pp. 172–179, 2018.
- [103] F. Zhou, “Research on online monitoring and diagnosis of bearing fault of wind turbine gearbox based on undecimated wavelet transformation,” in *2010 IEEE Youth Conference on Information Computing and Telecommunications (YC-ICT)*. IEEE, 2010, pp. 251–254.
- [104] Y. Lv, N. Guan, J. Liu, and T. Cai, “The fault diagnosis of rolling bearing in gearbox of wind turbines based on second generation wavelet,” in *2014 International Conference on Wavelet Analysis and Pattern Recognition (ICWAPR)*. IEEE, 2014, pp. 43–49.
- [105] C. Hu, M. Huang, Q. Yang, and W. Yan, “On the use of EEMD and SVM based approach for bearing fault diagnosis of wind turbine gearbox,” in *2016 Chinese Control and Decision Conference (CCDC)*. IEEE, 2016, pp. 3472–3477.

- [106] Z. Li, Y. Jiang, Q. Guo, C. Hu, and Z. Peng, “Multi-dimensional variational mode decomposition for bearing-crack detection in wind turbines with large driving-speed variations,” *Renewable Energy*, vol. 116, pp. 55–73, 2018.
- [107] Y. Guo, X. Chen, S. Wang, R. Sun, and Z. Zhao, “Wind turbine diagnosis under variable speed conditions using a single sensor based on the synchrosqueezing transform method,” *Sensors*, vol. 17, no. 5, p. 1149, 2017.
- [108] J. S. Smith, “The local mean decomposition and its application to EEG perception data,” *Journal of the Royal Society Interface*, vol. 2, no. 5, pp. 443–454, 2005.
- [109] J. Zhang, J. Zhang, M. Zhong, J. Zhong, J. Zheng, and L. Yao, “Detection for incipient damages of wind turbine rolling bearing based on vmd-amckd method,” *IEEE Access*, 2019.
- [110] W. Teng, X. Zhang, Y. Liu, A. Kusiak, and Z. Ma, “Prognosis of the remaining useful life of bearings in a wind turbine gearbox,” *Energies*, vol. 10, no. 1, pp. 1–16, 2017.
- [111] J. Saari, D. Strömbergsson, J. Lundberg, and A. Thomson, “Detection and identification of windmill bearing faults using a one-class support vector machine (svm),” *Measurement*, vol. 137, pp. 287–301, 2019.
- [112] J. B. Ali, L. Saidi, S. Harrath, E. Bechhoefer, and M. Benbouzid, “Online automatic diagnosis of wind turbine bearings progressive degradations under real experimental conditions based on unsupervised machine learning,” *Applied Acoustics*, vol. 132, pp. 167–181, 2018.
- [113] J. Li, X. Zhang, X. Zhou, and L. Lu, “Reliability assessment of wind turbine bearing based on the degradation-hidden-markov model,” *Renewable Energy*, vol. 132, pp. 1076–1087, 2019.
- [114] P. Zhang and P. Neti, “Detection of gearbox bearing defects using electrical signature analysis for doubly fed wind generators,” *IEEE Transactions on Industry Applications*, vol. 51, no. 3, pp. 2195–2200, 2015.

- [115] T. Bruce, E. Rounding, H. Long, and R. Dwyer-Joyce, “Characterisation of white etching crack damage in wind turbine gearbox bearings,” *Wear*, vol. 338, pp. 164–177, 2015.
- [116] B. Gould, A. Greco, K. Stadler, and X. Xiao, “An analysis of premature cracking associated with microstructural alterations in an AISI 52100 failed wind turbine bearing using X-ray tomography,” *Materials & Design*, vol. 117, pp. 417–429, 2017.
- [117] J. Gegner and W. Nierlich, “Service loading analysis of wind turbine gearbox rolling bearings based on X-ray diffraction residual stress measurements,” *Materials Science Forum*, vol. 768, pp. 723–732, 2014.
- [118] R. Dupuis, “Application of oil debris monitoring for wind turbine gearbox prognostics and health management,” in *Annual Conference of the prognostics and health management society*, 2010, pp. 1–15.
- [119] X. Gu and C. Chen, “Adaptive parameter-matching method of sr algorithm for fault diagnosis of wind turbine bearing,” *Journal of Mechanical Science and Technology*, vol. 33, no. 3, pp. 1007–1018, 2019.
- [120] J. Li, J. Zhang, M. Li, and Y. Zhang, “A novel adaptive stochastic resonance method based on coupled bistable systems and its application in rolling bearing fault diagnosis,” *Mechanical Systems and Signal Processing*, vol. 114, pp. 128–145, 2019.
- [121] J. Li, M. Li, J. Zhang, and G. Jiang, “Frequency-shift multiscale noise tuning stochastic resonance method for fault diagnosis of generator bearing in wind turbine,” *Measurement*, vol. 133, pp. 421–432, 2019.
- [122] H. Sun, Y. Zi, and Z. He, “Wind turbine fault detection using multiwavelet denoising with the data-driven block threshold,” *Applied Acoustics*, vol. 77, pp. 122–129, 2014.
- [123] W. He, Y. Zi, B. Chen, F. Wu, and Z. He, “Automatic fault feature extraction of mechanical anomaly on induction motor bearing using ensemble super-wavelet

- transform,” *Mechanical Systems and Signal Processing*, vol. 54, pp. 457–480, 2015.
- [124] W. Teng, X. Ding, Y. Zhang, Y. Liu, Z. Ma, and A. Kusiak, “Application of cyclic coherence function to bearing fault detection in a wind turbine generator under electromagnetic vibration,” *Mechanical Systems and Signal Processing*, vol. 87, pp. 279–293, 2017.
- [125] J. Chen, J. Pan, Z. Li, Y. Zi, and X. Chen, “Generator bearing fault diagnosis for wind turbine via empirical wavelet transform using measured vibration signals,” *Renewable Energy*, vol. 89, pp. 80–92, 2016.
- [126] X. Zheng, G. Zhou, J. Wang, H. Ren, and D. Li, “Variational mode decomposition applied to offshore wind turbine rolling bearing fault diagnosis,” in *2016 35th Chinese Control Conference (CCC)*. IEEE, 2016, pp. 6673–6677.
- [127] L. Song, X. R. Zhang, L. W. Su, and Y. J. Gu, “Fault diagnosis approach for incipient bearing fault in wind turbine under variable conditions,” *Applied Mechanics and Materials*, vol. 599, pp. 312–320, 2014.
- [128] X. Liu, L. Bo, and C. Peng, “Application of order cyclostationary demodulation to damage detection in a direct-driven wind turbine bearing,” *Measurement Science and Technology*, vol. 25, no. 2, p. 025004, 2013.
- [129] C. M. Pezzani, J. M. Bossio, A. M. Castellino, G. R. Bossio, and C. H. De Angelo, “A PLL-based resampling technique for vibration analysis in variable-speed wind turbines with PMSG: A bearing fault case,” *Mechanical Systems and Signal Processing*, vol. 85, pp. 354–366, 2017.
- [130] R. Zimroz, W. Bartelmus, T. Barszcz, and J. Urbanek, “Diagnostics of bearings in presence of strong operating conditions non-stationarity-A procedure of load-dependent features processing with application to wind turbine bearings,” *Mechanical systems and signal processing*, vol. 46, no. 1, pp. 16–27, 2014.
- [131] W. Teng, W. Wang, H. Ma, Y. Liu, Z. Ma, and H. Mu, “Adaptive fault detection of the bearing in wind turbine generators using parameterless empirical wavelet

- transform and margin factor,” *Journal of Vibration and Control*, vol. 25, no. 6, pp. 1263–1278, 2019.
- [132] E. Mollasalehi, D. Wood, and Q. Sun, “Indicative fault diagnosis of wind turbine generator bearings using tower sound and vibration,” *Energies*, vol. 10, no. 11, p. 1853, 2017.
- [133] X. Chen, Y. Yang, Z. Cui, and J. Shen, “Vibration fault diagnosis of wind turbines based on variational mode decomposition and energy entropy,” *Energy*, 2019.
- [134] J. Guo, S. Lu, C. Zhai, and Q. He, “Automatic bearing fault diagnosis of permanent magnet synchronous generators in wind turbines subjected to noise interference,” *Measurement Science and Technology*, vol. 29, no. 2, p. 025002, 2018.
- [135] W. Liu, Q. Gao, G. Ye, R. Ma, X. Lu, and J. Han, “A novel wind turbine bearing fault diagnosis method based on integral extension LMD,” *Measurement*, vol. 74, pp. 70–77, 2015.
- [136] J. Chen, J. Pan, C. Zhang, X. Luo, Z. Zhou, and B. Wang, “Specialization improved nonlocal means to detect periodic impulse feature for generator bearing fault identification,” *Renewable energy*, vol. 103, pp. 448–467, 2017.
- [137] B. Yang, R. Liu, and X. Chen, “Fault diagnosis for wind turbine generator bearing via sparse representation and shift-invariant K-SVD,” *IEEE Transactions on Industrial Informatics*, vol. 13, no. 3, pp. 1321–1331, 2017.
- [138] R. Sun, Z. Yang, Z. Zhai, and X. Chen, “Sparse representation based on parametric impulsive dictionary design for bearing fault diagnosis,” *Mechanical Systems and Signal Processing*, vol. 122, pp. 737–753, 2019.
- [139] Y. Guo, Z. Zhao, R. Sun, and X. Chen, “Data-driven multiscale sparse representation for bearing fault diagnosis in wind turbine,” *Wind Energy*, 2019.
- [140] J. Wang, W. Qiao, and L. Qu, “Wind turbine bearing fault diagnosis based on sparse representation of condition monitoring signals,” *IEEE Transactions on Industry Applications*, 2018.

- [141] M. R. Shahriar, P. Borghesani, and A. C. Tan, “Electrical signature analysis-based detection of external bearing faults in electromechanical drivetrains,” *IEEE Transactions on Industrial Electronics*, vol. 65, no. 7, pp. 5941–5950, 2018.
- [142] Y. Amirat, V. Choqueuse, M. Benbouzid, and J. F. Charpentier, “Bearing fault detection in DFIG-based wind turbines using the first intrinsic mode function,” in *2010 XIX International Conference on Electrical Machines (ICEM)*. IEEE, 2010, pp. 1–6.
- [143] Y. Amirat, M. Benbouzid, T. Wang, and S. Turri, “Performance analysis of an EEMD-based hilbert huang transform as a bearing failure detector in wind turbines,” in *2014 International Conference on Green Energy*. IEEE, 2014, pp. 193–198.
- [144] Y. Amirat, V. Choqueuse, and M. Benbouzid, “Wind turbine bearing failure detection using generator stator current homopolar component ensemble empirical mode decomposition,” in *IECON 2012-38th Annual Conference on IEEE Industrial Electronics Society*. IEEE, 2012, pp. 3937–3942.
- [145] Y. Amirat, V. Choqueuse, M. Benbouzid, and S. Turri, “Hilbert transform-based bearing failure detection in DFIG-based wind turbines,” *International Review of Electrical Engineering*, vol. 6, no. 3, pp. 1249–1256, 2011.
- [146] Y. Amirat, V. Choqueuse, and M. Benbouzid, “EEMD-based wind turbine bearing failure detection using the generator stator current homopolar component,” *Mechanical Systems and Signal Processing*, vol. 41, no. 1, pp. 667–678, 2013.
- [147] Y. Amirat, M. Benbouzid, T. Wang, K. Bacha, and G. Feld, “Bearing fault detection in wind turbines using dominant intrinsic mode function subtraction,” in *IECON 2016 - 42nd Annual Conference of the IEEE Industrial Electronics Society*. IEEE, 2016, pp. 6961–6965.
- [148] X. Chen, W. Xu, Y. Liu, and R. Islam, “Bearing corrosion failure diagnosis of doubly-fed induction generator in wind turbines based on stator current analysis,” *IEEE Transactions on Industrial Electronics*, pp. 1–1, 2019.

- [149] A. Kusiak and A. Verma, “Analyzing bearing faults in wind turbines: A data-mining approach,” *Renewable Energy*, vol. 48, pp. 110–116, 2012.
- [150] J. Wang, W. Qiao, and L. Qu, “Wind turbine bearing fault diagnosis based on sparse representation of condition monitoring signals,” in *2017 IEEE Energy Conversion Congress and Exposition (ECCE)*. IEEE, 2017, pp. 3696–3702.
- [151] Z. Liu, L. Zhang, and J. Carrasco, “Vibration analysis for large-scale wind turbine blade bearing fault detection with an empirical wavelet thresholding method,” *Renewable Energy*, vol. 146, pp. 99 – 110, 2020.
- [152] Z. Liu, X. Tang, X. Wang, J. E. Mugica, and L. Zhang, “Wind turbine blade bearing fault diagnosis under fluctuating speed operations via bayesian augmented lagrangian analysis,” *IEEE Transactions on Industrial Informatics*, pp. 1–1, 2020.
- [153] Z. Liu, X. Wang, and L. Zhang, “Fault diagnosis of industrial wind turbine blade bearing using acoustic emission analysis,” *IEEE Transactions on Instrumentation and Measurement*, pp. 1–1, 2020.
- [154] J. W. Han, J. S. Nam, Y. J. Park, G. H. Lee, and Y. Y. Nam, “An experimental study on the performance and fatigue life of pitch bearing for wind turbine,” *Journal of Mechanical Science and Technology*, vol. 29, no. 5, pp. 1963–1971, 2015.
- [155] Y. Pan, R. Hong, J. Chen, Z. Qin, and Y. Feng, “Incipient fault detection of wind turbine large-size slewing bearing based on circular domain,” *Measurement*, vol. 137, pp. 130–142, 2019.
- [156] H. Zong, H. Wang, S. Tian, and X. Gao, “A life test method and result analysis for slewing bearings in wind turbines,” *Proceedings of the Institution of Mechanical Engineers, Part C: Journal of Mechanical Engineering Science*, vol. 229, no. 18, pp. 3499–3514, 2015.
- [157] Y. Feng, J. Chen, X. D. Huang, and W. Wang, “Structure fatigue life analysis of a 1.5 MW smart yaw slewing bearing,” *Advanced Materials Research*, vol. 779, pp. 664–670, 2013.

- [158] Y. Wang and Q. Yuan, “Static load-carrying capacity and fatigue life of a double row pitch bearing with radial interference,” *Proceedings of the Institution of Mechanical Engineers, Part C: Journal of Mechanical Engineering Science*, vol. 228, no. 2, pp. 307–316, 2014.
- [159] R. U. Maheswari and R. Umamaheswari, “Trends in non-stationary signal processing techniques applied to vibration analysis of wind turbine drive train—a contemporary survey,” *Mechanical Systems and Signal Processing*, vol. 85, pp. 296–311, 2017.
- [160] W. Caesarendra, B. Kosasih, A. K. Tieu, H. Zhu, C. A. Moodie, and Q. Zhu, “Acoustic emission-based condition monitoring methods: Review and application for low speed slew bearing,” *Mechanical Systems and Signal Processing*, vol. 72, pp. 134–159, 2016.
- [161] P. Nikolakopoulos and A. Zavos, “Slew bearings damage detection using hilbert huang transformation and acoustic methods,” *Tribology in Industry*, vol. 37, no. 2, 2015.
- [162] M. Kang, J. Kim, and J.-M. Kim, “Reliable fault diagnosis for incipient low-speed bearings using fault feature analysis based on a binary bat algorithm,” *Information Sciences*, vol. 294, pp. 423–438, 2015.
- [163] S. A. Aye, P. S. Heyns, and C. J. Thiart, “Fault detection of slow speed bearings using an integrated approach,” *IFAC-PapersOnLine*, vol. 48, no. 3, pp. 1779–1784, 2015.
- [164] M. Žvokelj, S. Zupan, and I. Prebil, “Eemd-based multiscale ica method for slewing bearing fault detection and diagnosis,” *Journal of Sound and Vibration*, vol. 370, pp. 394–423, 2016.
- [165] X. Q. Bai, H. L. Xiao, and L. Zhang, “The condition monitoring of large slewing bearing based on oil analysis method,” in *Key Engineering Materials*, vol. 474. Trans Tech Publ, 2011, pp. 716–719.
- [166] V. K. Patel and M. A. Soni, “Analyses of water contaminants lubricated deep

groove ball bearing through vibration, shock pulse and temperature measurement,” 2017.

- [167] A. Timofiejczuk, F. Chaari, R. Zimroz, W. Bartelmus, and M. Haddar, “Advances in condition monitoring of machinery in non-stationary operations,” in *International Congress on Technical Diagnostics-International Conference on Condition Monitoring of Machinery in Non-Stationary Operations 2016 CONGRESS*, vol. 9. Springer, 2018.
- [168] B. Li and X. Zhang, “A new strategy of instantaneous angular speed extraction and its application to multistage gearbox fault diagnosis,” *Journal of Sound and Vibration*, vol. 396, pp. 340–355, 2017.
- [169] B. Li, X. Zhang, and J. Wu, “New procedure for gear fault detection and diagnosis using instantaneous angular speed,” *Mechanical Systems and Signal Processing*, vol. 85, pp. 415–428, 2017.
- [170] Y. Zhou, T. Tao, X. Mei, G. Jiang, and N. Sun, “Feed-axis gearbox condition monitoring using built-in position sensors and eemd method,” *Robotics and Computer-Integrated Manufacturing*, vol. 27, no. 4, pp. 785–793, 2011.
- [171] B. Li and X. Zhang, “A new strategy of instantaneous angular speed extraction and its application to multistage gearbox fault diagnosis,” *Journal of Sound and Vibration*, vol. 396, pp. 340–355, 2017.
- [172] S. Lu, Q. He, and J. Zhao, “Bearing fault diagnosis of a permanent magnet synchronous motor via a fast and online order analysis method in an embedded system,” *Mechanical Systems and Signal Processing*, 2017.
- [173] X. Wang, J. Guo, S. Lu, C. Shen, and Q. He, “A computer-vision-based rotating speed estimation method for motor bearing fault diagnosis,” *Measurement Science and Technology*, vol. 28, no. 6, p. 065012, 2017.
- [174] Y. Wang, Y. Xie, G. Xu, S. Zhang, and C. Hou, “Tacholeless order-tracking approach for wind turbine gearbox fault detection,” *Frontiers of Mechanical Engineering*, vol. 12, no. 3, pp. 427–439, 2017.

- [175] M. A. Ismail, N. Sawalhi, and A. Bierig, “Fault diagnosis of wind turbine gear-boxes using enhanced tachless order tracking,” 2018.
- [176] M. Zhao, J. Lin, X. Xu, and Y. Lei, “Tachless envelope order analysis and its application to fault detection of rolling element bearings with varying speeds,” *Sensors*, vol. 13, no. 8, pp. 10 856–10 875, 2013.
- [177] Y. Hu, X. Tu, F. Li, H. Li, and G. Meng, “An adaptive and tachless order analysis method based on enhanced empirical wavelet transform for fault detection of bearings with varying speeds,” *Journal of Sound and Vibration*, vol. 409, pp. 241–255, 2017.
- [178] H. Huang, N. Baddour, and M. Liang, “Bearing fault diagnosis under unknown time-varying rotational speed conditions via multiple time-frequency curve extraction,” *Journal of Sound and Vibration*, vol. 414, pp. 43–60, 2018.
- [179] F. Moss, L. M. Ward, and W. G. Sannita, “Stochastic resonance and sensory information processing: a tutorial and review of application,” *Clinical neurophysiology*, vol. 115, no. 2, pp. 267–281, 2004.
- [180] J. Guo, S. Lu, C. Zhai, and Q. He, “Automatic bearing fault diagnosis of permanent magnet synchronous generators in wind turbines subjected to noise interference,” *Measurement Science and Technology*, vol. 29, no. 2, p. 025002, 2018.
- [181] Y. Lei, D. Han, J. Lin, and Z. He, “Planetary gearbox fault diagnosis using an adaptive stochastic resonance method,” *Mechanical Systems and Signal Processing*, vol. 38, no. 1, pp. 113–124, 2013.
- [182] Z. Qiao, Y. Lei, J. Lin, and F. Jia, “An adaptive unsaturated bistable stochastic resonance method and its application in mechanical fault diagnosis,” *Mechanical Systems and Signal Processing*, vol. 84, pp. 731–746, 2017.
- [183] P. Sopcik and D. O’Sullivan, “How sensor performance enables condition-based monitoring solutions,” *5 Making Sense of Sounds, or How AI Can Boost Your Machines’ Uptime*, p. 45.

- [184] H. Saruhan, S. Sandemir, A. Çiçek, and I. Uygur, “Vibration analysis of rolling element bearings defects,” *Journal of applied research and technology*, vol. 12, no. 3, pp. 384–395, 2014.
- [185] W. Xin, Y. Liu, Y. He, and B. Su, “Amplitude envelope analysis for feature extraction of direct-driven wind turbine bearing failure,” in *2012 10th World Congress on Intelligent Control and Automation (WCICA)*. IEEE, 2012, pp. 3173–3176.
- [186] A. Muthukumarasamy and S. Ganeriwala, “The effect of frequency resolution in bearing fault studies,” *Technote, SpectraQuest Inc*, 2010.
- [187] W. Caesarendra, B. Kosasih, A. K. Tieu, and C. A. Moodie, “Application of the largest lyapunov exponent algorithm for feature extraction in low speed slew bearing condition monitoring,” *Mechanical Systems and Signal Processing*, vol. 50, pp. 116–138, 2015.
- [188] R. Poore, “Development of an operations and maintenance cost model to identify cost of energy savings for low wind speed turbines: July 2, 2004–june 30, 2008,” National Renewable Energy Laboratory (NREL), Golden, CO., Tech. Rep., 2008.
- [189] Z. Gao, C. Cecati, and S. X. Ding, “A survey of fault diagnosis and fault-tolerant techniques-part I: Fault diagnosis with model-based and signal-based approaches,” *IEEE Transactions on Industrial Electronics*, vol. 62, no. 6, pp. 3757–3767, 2015.
- [190] J. Antoni, “Fast computation of the kurtogram for the detection of transient faults,” *Mechanical Systems and Signal Processing*, vol. 21, no. 1, pp. 108–124, 2007.
- [191] T. Wang, M. Liang, J. Li, and W. Cheng, “Rolling element bearing fault diagnosis via fault characteristic order (fco) analysis,” *Mechanical Systems and Signal Processing*, vol. 45, no. 1, pp. 139–153, 2014.
- [192] T. Wang, M. Liang, J. Li, W. Cheng, and C. Li, “Bearing fault diagnosis under unknown variable speed via gear noise cancellation and rotational order sideband

- identification,” *Mechanical Systems and Signal Processing*, vol. 62, pp. 30–53, 2015.
- [193] F. Combet and R. Zimroz, “A new method for the estimation of the instantaneous speed relative fluctuation in a vibration signal based on the short time scale transform,” *Mechanical Systems and Signal Processing*, vol. 23, no. 4, pp. 1382–1397, 2009.
- [194] S. Schmidt, P. S. Heyns, and J. P. De Villiers, “A tacholeless order tracking methodology based on a probabilistic approach to incorporate angular acceleration information into the maxima tracking process,” *Mechanical Systems and Signal Processing*, vol. 100, pp. 630–646, 2018.
- [195] D. Siegel, H. Al-Atat, V. Shauche, L. Liao, J. Snyder, and J. Lee, “Novel method for rolling element bearing health assessment—a tachometer-less synchronously averaged envelope feature extraction technique,” *Mechanical Systems and Signal Processing*, vol. 29, pp. 362–376, 2012.
- [196] J. Gilles, “Empirical wavelet transform,” *IEEE transactions on signal processing*, vol. 61, no. 16, pp. 3999–4010, 2013.
- [197] J. Gilles, G. Tran, and S. Osher, “2d empirical transforms. Wavelets, ridgelets, and curvelets revisited,” *SIAM Journal on Imaging Sciences*, vol. 7, no. 1, pp. 157–186, 2014.
- [198] J. Delon, A. Desolneux, J.-L. Lisani, and A. B. Petro, “A nonparametric approach for histogram segmentation,” *IEEE Transactions on Image Processing*, vol. 16, no. 1, pp. 253–261, 2007.
- [199] J. Gilles and K. Heal, “A parameterless scale-space approach to find meaningful modes in histograms-Application to image and spectrum segmentation,” *International Journal of Wavelets, Multiresolution and Information Processing*, vol. 12, no. 06, p. 1450044, 2014.
- [200] D. L. Donoho and I. M. Johnstone, “Threshold selection for wavelet shrinkage of noisy data,” in *Proceedings of 16th Annual International Conference of the IEEE Engineering in Medicine and Biology Society*, Nov 1994, pp. A24–A25 vol.1.

- [201] D. L. Donoho, I. M. Johnstone *et al.*, “Ideal denoising in an orthonormal basis chosen from a library of bases,” *Comptes rendus de l’Académie des sciences. Série I, Mathématique*, vol. 319, no. 12, pp. 1317–1322, 1994.
- [202] L. Marple, “Computing the discrete-time ‘analytic’ signal via fft,” *IEEE Transactions on signal processing*, vol. 47, no. 9, pp. 2600–2603, 1999.
- [203] M. Kedadouché, M. Thomas, and A. Tahan, “A comparative study between Empirical Wavelet Transforms and Empirical Mode Decomposition Methods: Application to bearing defect diagnosis,” *Mechanical Systems and Signal Processing*, vol. 81, pp. 88–107, 2016.
- [204] K. P. Balanda and H. MacGillivray, “Kurtosis: a critical review,” *The American Statistician*, vol. 42, no. 2, pp. 111–119, 1988.
- [205] W. Zhou, T. G. Habetler, and R. G. Harley, “Bearing fault detection via stator current noise cancellation and statistical control,” *IEEE Transactions on Industrial Electronics*, vol. 55, no. 12, pp. 4260–4269, 2008.
- [206] J. Antoni, “Fast computation of the kurtogram for the detection of transient faults,” *Mechanical Systems and Signal Processing*, vol. 21, no. 1, pp. 108–124, 2007.
- [207] J. Antoni and R. Randall, “Unsupervised noise cancellation for vibration signals: part I - evaluation of adaptive algorithms,” *Mechanical Systems and Signal Processing*, vol. 18, no. 1, pp. 89–101, 2004.
- [208] R. Randall and J. Antoni, “Unsupervised noise cancellation for vibration signals: part II-a novel frequency-domain algorithm,” *Mechanical Systems and Signal Processing*, vol. 18, no. 1, pp. 103–117, 2004.
- [209] H. Ocaik and K. A. Loparo, “Estimation of the running speed and bearing defect frequencies of an induction motor from vibration data,” *Mechanical Systems and Signal Processing*, vol. 18, no. 3, pp. 515 – 533, 2004.
- [210] J. Wang, L. Qiao, Y. Ye, and Y. Chen, “Fractional envelope analysis for rolling element bearing weak fault feature extraction,” *IEEE/CAA Journal of Automatica Sinica*, vol. 4, no. 2, pp. 353–360, April 2017.

- [211] P. Perona and J. Malik, “Scale-space and edge detection using anisotropic diffusion,” *IEEE Transactions on Pattern Analysis and Machine Intelligence*, vol. 12, no. 7, pp. 629–639, Jul 1990.
- [212] Y. Li, Y. Ding, and T. Li, “Nonlinear diffusion filtering for peak-preserving smoothing of a spectrum signal,” *Chemometrics and Intelligent Laboratory Systems*, vol. 156, pp. 157–165, 2016.
- [213] A. S. Raj and N. Murali, “Early classification of bearing faults using morphological operators and fuzzy inference,” *IEEE Transactions on Industrial Electronics*, vol. 60, no. 2, pp. 567–574, 2013.
- [214] N. Nikolaou and I. Antoniadis, “Application of morphological operators as envelope extractors for impulsive-type periodic signals,” *Mechanical Systems and Signal Processing*, vol. 17, no. 6, pp. 1147–1162, 2003.
- [215] G. Gerig, O. Kubler, R. Kikinis, and F. A. Jolesz, “Nonlinear anisotropic filtering of MRI data,” *IEEE Transactions on Medical Imaging*, vol. 11, no. 2, pp. 221–232, Jun 1992.
- [216] E. Michel-González, M. H. Cho, and S. Y. Lee, “Geometric nonlinear diffusion filter and its application to X-ray imaging,” *BioMedical Engineering OnLine*, vol. 10, no. 1, p. 47, Jun 2011.
- [217] “Acoustics and vibration database,” <http://data-acoustics.com/measurements/bearing-faults/bearing-1/>, accessed: 26/08/2019.
- [218] Y. Lei, B. Yang, X. Jiang, F. Jia, N. Li, and A. K. Nandi, “Applications of machine learning to machine fault diagnosis: A review and roadmap,” *Mechanical Systems and Signal Processing*, vol. 138, p. 106587, 2020.
- [219] Z. Feng, M. Liang, and F. Chu, “Recent advances in time–frequency analysis methods for machinery fault diagnosis: A review with application examples,” *Mechanical Systems and Signal Processing*, vol. 38, no. 1, pp. 165 – 205, 2013.
- [220] Z. Zhang, Y. Xu, J. Yang, X. Li, and D. Zhang, “A survey of sparse representation: Algorithms and applications,” *IEEE Access*, vol. 3, pp. 490–530, 2015.

- [221] B. Yang, R. Liu, and X. Chen, “Sparse time-frequency representation for incipient fault diagnosis of wind turbine drive train,” *IEEE Transactions on Instrumentation and Measurement*, vol. 67, no. 11, pp. 2616–2627, Nov 2018.
- [222] X. Chen, Z. Du, J. Li, X. Li, and H. Zhang, “Compressed sensing based on dictionary learning for extracting impulse components,” *Signal Processing*, vol. 96, pp. 94 – 109, 2014, time-frequency methods for condition based maintenance and modal analysis.
- [223] H. Yang, J. Mathew, and L. Ma, “Fault diagnosis of rolling element bearings using basis pursuit,” *Mechanical Systems and Signal Processing*, vol. 19, no. 2, pp. 341 – 356, 2005.
- [224] J. Wang, W. Qiao, and L. Qu, “Wind turbine bearing fault diagnosis based on sparse representation of condition monitoring signals,” *IEEE Transactions on Industry Applications*, pp. 1–1, 2018.
- [225] Z. Du, X. Chen, H. Zhang, and R. Yan, “Sparse feature identification based on union of redundant dictionary for wind turbine gearbox fault diagnosis,” *IEEE Transactions on Industrial Electronics*, vol. 62, no. 10, pp. 6594–6605, Oct 2015.
- [226] H. Liu, C. Liu, and Y. Huang, “Adaptive feature extraction using sparse coding for machinery fault diagnosis,” *Mechanical Systems and Signal Processing*, vol. 25, no. 2, pp. 558 – 574, 2011.
- [227] F. Hou, J. Chen, and G. Dong, “Weak fault feature extraction of rolling bearings based on globally optimized sparse coding and approximate SVD,” *Mechanical Systems and Signal Processing*, vol. 111, pp. 234 – 250, 2018.
- [228] C. Zhao, Z. Feng, X. Wei, and Y. Qin, “Sparse classification based on dictionary learning for planet bearing fault identification,” *Expert Systems with Applications*, vol. 108, pp. 233 – 245, 2018.
- [229] B. Yang, R. Liu, and X. Chen, “Fault diagnosis for a wind turbine generator bearing via sparse representation and shift-invariant K-SVD,” *IEEE Transactions on Industrial Informatics*, vol. 13, no. 3, pp. 1321–1331, 2017.

- [230] X. Tang, L. Zhang, and X. Li, “Bayesian augmented lagrangian algorithm for system identification,” *Systems & Control Letters*, vol. 120, pp. 9–16, 2018.
- [231] F. Bonnardot, M. El Badaoui, R. Randall, J. Daniere, and F. Guillet, “Use of the acceleration signal of a gearbox in order to perform angular resampling (with limited speed fluctuation),” *Mechanical Systems and Signal Processing*, vol. 19, no. 4, pp. 766–785, 2005.
- [232] H. Huang and N. Baddour, “Bearing vibration data collected under time-varying rotational speed conditions,” *Data in Brief*, vol. 21, pp. 1745 – 1749, 2018.
- [233] J. Antoni, “Unsupervised noise cancellation for vibration signals: part II—a novel frequency-domain algorithm,” *Mechanical Systems and Signal Processing*, vol. 18, no. 1, pp. 103 – 117, 2004.
- [234] J. Smith, “Vibration monitoring of bearings at low speeds,” *Tribology International*, vol. 15, no. 3, pp. 139–144, 1982.
- [235] J. Miettinen and P. Pataniitty, “Acoustic emission in monitoring extremely slowly rotating rolling bearing,” in *Proceedings of COMADEM*, vol. 99, 1999, pp. 289–297.
- [236] N. Jamaludin, D. Mba, and R. Bannister, “Condition monitoring of slow-speed rolling element bearings using stress waves,” *Proceedings of the Institution of Mechanical Engineers, Part E: Journal of Process Mechanical Engineering*, vol. 215, no. 4, pp. 245–271, 2001.
- [237] A. Widodo, E. Y. Kim, J.-D. Son, B.-S. Yang, A. C. Tan, D.-S. Gu, B.-K. Choi, and J. Mathew, “Fault diagnosis of low speed bearing based on relevance vector machine and support vector machine,” *Expert systems with applications*, vol. 36, no. 3, pp. 7252–7261, 2009.
- [238] M. Elforjani and D. Mba, “Accelerated natural fault diagnosis in slow speed bearings with acoustic emission,” *Engineering Fracture Mechanics*, vol. 77, no. 1, pp. 112–127, 2010.

- [239] M. Žvokelj, S. Zupan, and I. Prebil, “EEMD-based multiscale ica method for slewing bearing fault detection and diagnosis,” *Journal of Sound and Vibration*, vol. 370, pp. 394 – 423, 2016.
- [240] S. A. Aye, P. S. Heyns, and C. J. Thiert, “Fault detection of slow speed bearings using an integrated approach,” *IFAC-PapersOnLine*, vol. 48, no. 3, pp. 1779 – 1784, 2015, 15th IFAC Symposium on Information Control Problems in Manufacturing.
- [241] P. Borghesani, P. Pennacchi, R. Randall, N. Sawalhi, and R. Ricci, “Application of cepstrum pre-whitening for the diagnosis of bearing faults under variable speed conditions,” *Mechanical Systems and Signal Processing*, vol. 36, no. 2, pp. 370 – 384, 2013.
- [242] R. B. Randall and N. Sawalhi, “Cepstral removal of periodic spectral components from time signals,” in *Advances in Condition Monitoring of Machinery in Non-Stationary Operations*. Springer, 2014, pp. 313–324.
- [243] C. Peeters, P. Guillaume, and J. Helsen, “Signal pre-processing using cepstral editing for vibration-based bearing fault detection,” 09 2016.
- [244] J. Wang, G. Xu, Q. Zhang, and L. Liang, “Application of improved morphological filter to the extraction of impulsive attenuation signals,” *Mechanical Systems and Signal Processing*, vol. 23, no. 1, pp. 236–245, 2009.
- [245] N. Nikolaou and I. Antoniadis, “Application of morphological operators as envelope extractors for impulsive-type periodic signals,” *Mechanical Systems and Signal Processing*, vol. 17, no. 6, pp. 1147 – 1162, 2003.
- [246] A. S. Raj and N. Murali, “Early classification of bearing faults using morphological operators and fuzzy inference,” *IEEE Transactions on Industrial Electronics*, vol. 60, no. 2, pp. 567–574, Feb 2013.
- [247] R. Randall and N. Sawalhi, “Editing time signals using the real cepstrum,” *Technical Program for MFPT: The Applied Systems Health Management Conference 2011: Enabling Sustainable Systems*, 01 2011.

- [248] R. B. Randall, “A history of cepstrum analysis and its application to mechanical problems,” *Mechanical Systems and Signal Processing*, vol. 97, pp. 3–19, 2017.
- [249] M. B. Priestley, “Spectral analysis and time series,” 1981.
- [250] W. Caesarendra, B. Kosasih, A. K. Tieu, H. Zhu, C. A. Moodie, and Q. Zhu, “Acoustic emission-based condition monitoring methods: Review and application for low speed slew bearing,” *Mechanical Systems and Signal Processing*, vol. 72-73, pp. 134 – 159, 2016.